ABSTRACT

Title of Dissertation: LEVERAGING SELF-ASSEMBLY AND BIOPHYSICAL DESIGN TO BUILD NEXT-GENERATION IMMUNOTHERAPIES

Yevgeniy Froimchuk, Doctor of Philosophy, 2022

Dissertation directed by: Dr. Christopher M. Jewell, Professor, Fischell Department of Bioengineering, University of Maryland, College Park

The immune system has evolved mechanisms to respond not only to specific molecular signals, but also to biophysical cues. Interestingly, research at the interface of biomaterials and immunology has also revealed that the biophysical properties and form of vaccines and immunotherapies impact immunological outcomes. For example, the intermolecular distance between antigen molecules on the surface of nanoparticles can impact formation of T cell receptor clusters that are critical during T cell activation. Despite the importance of biophysical cues in tuning the immune response, the connections between these parameters and immunological outcomes are poorly understood in the context of immunotherapy. Immunotherapies harness an individual's immune system to battle diseases such as autoimmunity. During autoimmune disease, the immune system malfunctions and mistakenly attacks self-tissue. Immunotherapies can help tailor and guide more effective responses in these settings, as evidenced by recent advances with monoclonal antibodies and adoptive cell therapies. However, despite the transformative gains of immunotherapies for patients, many therapies are not curative, work only for a small subset of patients, and lack specificity in distinguishing between healthy and diseased cells, which can cause severe side effects. To overcome these challenges, experimental strategies are attempting to co-

deliver self-antigens and modulatory cues to reprogram dysfunctional responses against self-antigens without hindering normal immune function. These strategies have shown exciting potential in pre-clinical models of autoimmune disease but are unproven in clinical research. Understanding how biophysical features are linked to immunological mechanisms in these settings would add a critical dimension to designing translatable, antigen-specific immunotherapies.

Self-assembling materials are a class of biomaterials that spontaneously assemble in aqueous solution. Self-assembling modalities are useful technologies to study the links between biophysical parameters and immune outcomes because they offer precise control and uniformity of the biophysical properties of assembled moieties. Our lab leveraged the benefits of self-assembly to pioneer development of "carrier-free" immunotherapies composed entirely of immune signals. The therapies are composed of self-antigens modified with cationic amino acid residues and anionic, nucleic acid based modulatory cues. These signals are self-assembled into nanostructured complexes via electrostatic interactions. The research in this dissertation utilizes this platform as a tool to understand how tuning the biophysical properties of self-antigens impacts molecular interactions during self-assembly and in turn, how changes in biophysical features are linked to immunological outcomes. Surface plasmon resonance studies revealed that the binding affinity between signals can be tuned by altering overall cationic charge and charge density of self-antigen, and by anchoring the self-antigen with arginine or lysine residues. For example, the binding affinity between signals can be increased by increasing the total cationic charge on the self-antigen, and by anchoring the self-antigen with arginine residues rather than lysine residues. Computational modeling approaches generated insights into how molecular interactions between signals, such as hydrogen bonding, salt-bridges, and hydrophobic interactions, change with different design parameters. In vitro assays revealed that a lower binding affinity between self-

assembled signals was associated with greater reduction of inflammatory gene expression in dendritic cells and more differentiation of self-reactive T cells towards regulatory phenotypes that are protective during autoimmunity. Taken all together, these insights help intuit how to use biophysical design to improve modularity of the self-assembly platform to incorporate a range of antigens for distinct disease targets. This granular understanding of nanomaterial-immune interactions contributes to more rational immunotherapy design.

LEVERAGING SELF-ASSEMBLY AND BIOPHYSICAL DESIGN TO BUILD NEXT-GENERATION IMMUNOTHERAPIES

by

Yevgeniy Froimchuk

Dissertation submitted to the Faculty of the Graduate School of the
University of Maryland, College Park, in partial fulfillment
of the requirements for the degree of
Doctor of Philosophy
2022

Advisory Committee:
Professor Christopher M. Jewell, Chair
Professor Katharina Maisel
Professor Silvina Matysiak
Professor David M. Mosser, Dean's Representative
Professor Srinivasa R. Raghavan

Table of Contents

List of Tables

List of Figures

CHAPTER 1: INTRODUCTION

In recent years, research at the interface of biomaterials and immunology has revealed that the biophysical properties of scaffolds, particles, and other carriers of vaccines and immunotherapies impact immunological outcomes. For example, uptake and processing pathways of immune cues are impacted by the size and surface charge of polymer or lipid particles carrying these signals.[1,2] Likewise, the display density of signals on nanoparticles can impact efficacy and important immunological processes required for immunity or tolerance.[3,4] Thus, outcomes are impacted not only through specific signal combinations, doses, and tissue locations, but by the biophysical parameters and forms through which the signals are delivered. These parameters are important considerations when designing immunotherapies to battle diseases like autoimmunity and cancer. Unfortunately, these links are poorly understood, discovered primarily through observational studies.

The body of work in this dissertation utilized self-assembly of immune signals as a platform and tool to study the links between biophysical parameters and immune outcomes. The goal of the work was to study how changes in molecular structure impact molecular interactions between self-assembled immune signals, how those molecular interactions impact the overall

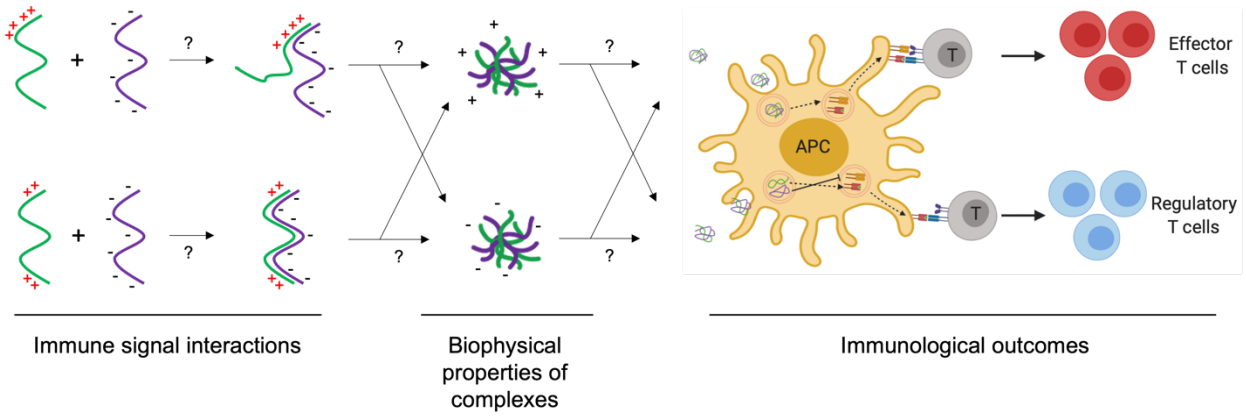

Figure 1. The goal of the dissertation work was to study the links between biophysical design and immune outcomes to help improve the engineering of self-assembled immunotherapies.

biophysical properties of self-assembled immunotherapies, and in turn, how the changes in molecular structure and biophysical properties impact immunological outcomes (**Fig. 1**). This knowledge will inform how biophysical parameters of self-assembled immune cues, such as binding affinity, can be utilized as a tool and design lever to engineer next-generation immunotherapies. Chapter 1 provides an introduction of key areas important for understanding the work presented in subsequent chapters.

1.1) Antigen presenting cells are key therapeutic targets to modulate adaptive immune responses

Antigen presenting cells (APCs) of the innate immune system, such as dendritic cells and macrophages, survey our tissues, constantly clearing the body of cellular debris and engulfing foreign substances. During this activity, antigen presenting cells process and present molecular fragments of engulfed material – termed antigens – on their surface to activate the highly-specific "adaptive" arm of the immune system. APCs make use of many environmental cues to direct processing and presentation of antigens by distinct mechanisms.[5] Some of these cues include signaling proteins called cytokines and activation of pattern recognition receptors, such as toll-like receptors, that recognize foreign molecular patterns that are uncommon in mammalian hosts. Concurrently, cells in our body present self-antigens from their own internal machinery to ensure the immune system can distinguish between host cells and foreign pathogens, such as bacteria or viruses. External antigens are presented in major histocompatibility complex (MHC)-II proteins while internal (i.e., self) antigens are presented in MHC-I proteins. Loading of a peptide antigen into a major histocompatibility complex is dependent on specific interactions that take place in the binding groove of the MHC. The interactions depend on the geometry, charge distribution, and hydrophobicity of both the binding groove and the peptide, as well as the length of the peptide.[6,7]

After dendritic cells and other APCs encounter foreign antigen, they migrate to lymph nodes to present antigens to lymphocytes of the adaptive immune system, such as T cells and B cells. Activation of T cells typically requires three signals. The first is recognition of an MHC protein containing antigen that matches the specificity of the T cell; this is the "cognate" antigen. The second signal is recognition of costimulatory molecules APCs present to lymphocytes along with the cognate antigen. The third is cytokines that direct polarization of lymphocytes towards specific functional phenotypes. If a T cell binds its cognate antigen in the presence of appropriate machinery and costimulatory signals, the T cell activates, proliferates, and migrates to the periphery in search of cells or pathogens expressing the cognate antigen. CD4 T cells adopt helper phenotypes, including T_H1 and T_H17, that shape adaptive immune responses by secreting cytokines that influence immune clearance mechanisms. CD8 T cells become cytotoxic T cells that directly kill cells expressing the cognate antigen. B cells produce antibodies that neutralize cells, extracellular pathogens such as bacteria, and toxins expressing the cognate antigen. If dendritic cells present antigen without the appropriate costimulatory signals, as in the case of self-antigens originating from host cells, lymphocytes can be rendered inactive against cognate antigen or adopt regulatory phenotypes (e.g., T_{REG}) that prevent attack of host cells expressing those antigens, otherwise known as immunological tolerance. Due to the intricate interactions described, controlling the initial events that dictate signals between dendritic cells and T cells is crucial in developing engineered approaches to direct immune function.[8] To achieve this level of control, precise understanding of how immune cells respond to specific signals and also how biophysical properties are linked to immunological outcomes needs to be understood.

1.2) Biophysical properties impact immunological mechanisms and therapeutic outcomes

In addition to the specific signals immune cells encounter, the biophysical properties of the signals and interactions, such as hydrophobicity and binding affinity, are also important in driving immunological processes. For example, innate immune cells have evolved to detect hydrophobic motifs as a universal signal to recognize damage and initiate immunity and repair responses.[9] During T cell development, T cells that bind self-antigen with high affinity are eliminated from the repertoire via negative selection, and T cells that bind self-antigen with low affinity are positively selected.[10] This selection process generates T cells that have low affinity for self-antigens and high affinity for foreign antigens. Further, the affinity with which a T cell binds its cognate antigen impacts the T cell's level of activity and specificity.[11] A T cell's immunological response is also a biophysical event that requires a minimum number of T cell antigen receptors to be connected or "clustered" before an immunogenic signal is delivered to the T cell.[12,13]

Given that the immune system is sensitive to biophysical parameters, it is unsurprising that physical properties of immunotherapies impact how immunotherapies are encountered and processed by immune cells. The size and shape of particles can skew how different APCs take up and process immune cues[14-18] and in turn, the phenotype of T cells after activation.[19] For example, one study showed that compared to 500 nm particles, 50 nm particles are taken up more efficiently and induce greater levels of costimulatory marker expression by pulmonary dendritic cells.[18] Additionally, the dose of antigen and density or intermolecular distance of antigen on the surface of particles can impact important immunological phenomena such as T cell polarization,[20] formation of T cell receptor clusters,[3] and therapeutic efficacy in pre-clinical mouse models.[4] Our lab showed that at a fixed antigen dose, treating with more particles displaying fewer peptide antigens per particle had greater therapeutic efficacy than treating with fewer particles with more peptide antigens per particle in a mouse model of autoimmune disease. This was a striking example

of a biophysical design parameter (antigen density on the surface of nanoparticles) impacting therapeutic outcomes. Surface properties of therapies, such as hydrophobicity of particles[21] and surface charge[1,2,22] can also impact uptake and trafficking pathways of particles by APCs. One recent study observed that compared to near-neutral particles, more negatively charged particles were taken up more efficiently by distinct subsets of dendritic cells involved in activation of helper T cells.[22] All of these observations indicate that, in addition to the specific immune cues, biophysical properties are important design parameters to consider when formulating immunotherapies. Yet, the links between biophysical properties and immune outcomes are poorly defined. Elucidating these links could inform precisely what combination of immune cues and biophysical properties are necessary to tune interactions between dendritic cells and T cells to direct specific immune outcomes.

1.3) Immunotherapies promote immune responses to fight cancer and autoimmune disease

One key area where precise links between biophysical properties and immune outcomes would be transformative is immunotherapies. Therapeutic immunotherapies harness an individual's immune system to stimulate immune responses that better fight diseases like cancer and autoimmunity.[8,23-25] When fighting a disease like cancer that is characterized by uncontrollable cell division, the immune system often fails to generate effective anti-tumor responses because many of the antigens on tumors are indistinguishable from those on healthy host cells. Additionally, cancer cells actively suppress the immune system by overexpressing molecules such as PD-1 and CTLA-4, which are natural suppressors the immune system normally uses to restrain immune function. When treating cancer, immunotherapies attempt to boost immune response to destroy cancer cells that otherwise evade and suppress the immune system. Important clinical strategies include monoclonal antibodies,[26] such as rituximab which targets B cells in certain types

of cancers, and more recently, the exciting development of checkpoint inhibitor antibodies.[27] For example, anti-PD-1 and anti-CTLA-4 antibodies unleash the stimulatory immune pathways that tumors normally block. However, an important limitation to consider is that cancer immunotherapies that stimulate immunity create risk of uncontrolled immunotoxicity that can drive severe – sometimes fatal – side effects.[28,29]

Conversely, in treating autoimmune disease, the goal of immunotherapies is to suppress inflammatory responses.[30] During autoimmune diseases such as multiple sclerosis, type 1 diabetes, and rheumatoid arthritis, the immune system mistakenly targets self-antigens, resulting in attack of an individual's own tissues. For example, in multiple sclerosis, the myelin matrix coating axons of the central nervous system is attacked. In these contexts, immunotherapies seek to suppress inflammatory responses to restore balance and prevent dysfunctional attacks against the body.[30] Despite their effectiveness in mitigating symptoms, treatments for autoimmune disease remain non-curative, require lifelong treatment, and are broadly immunosuppressive, which can leave patients susceptible to opportunistic infections and malignancies. New immunotherapies are leveraging molecularly specific targeting to provide new benefits relative to existing suppressive options. One new monoclonal antibody, ocrelizumab, is the first FDA approved drug for the progressive form of multiple sclerosis.[31] Another exciting monoclonal antibody, Tzield, is the first FDA approved therapeutic that delays clinical onset of type 1 diabetes.[32] Despite the transformative gains these breakthroughs have provided for patients, a limitation of immunotherapies continues to be lack of specificity in targeting or in the specificity of the resulting immune response. For example, even monoclonal antibodies do not distinguish between the target markers expressed on healthy cells and diseased cells, such as those that attack self-tissue during

autoimmunity. A critical challenge for new strategies is then to induce sustained, antigen-specific immune responses without impeding normal immune function.

1.4) New pre-clinical strategies incorporate biomaterials to improve specificity and potency of immune response

Given that adaptive immune responses are inherently antigen-specific and are initiated by APCs of the innate immune system, targeting innate pathways to induce antigen-specific tolerance is a promising approach currently being explored in pre-clinical models.[8,24] The general approach involves delivering self-antigens attacked during autoimmune disease to APCs either alone or along with a modulatory signal. These strategies seek to control the processing of immune cues and the interactions between APCs and lymphocytes to program selective, antigen-specific tolerance.

Biomaterials have emerged as promising technologies to help achieve delivery of signals to APCs while also overcoming some of the limitations of immunotherapy highlighted above.[8,24,25,33] The term biomaterials encompasses a broad range of organic and inorganic compounds, including polymers, metals, peptides, nucleic acids, and even cells, that are used in biological applications. These materials offer attractive properties including encapsulation of multiple signals for co-delivery, protection of cargo from enzymatic degradation and pH changes, tunable release kinetics, and increased circulation times. Biomaterials also allow for delivery of immune signals in particulate form, which can improve uptake and potency of the signals.[34-36] Additionally, biomaterials allow for control of ligand density, a biophysical parameter that impacts immune cell activation and therapeutic efficacy.[3,4] Given that adaptive immune responses are inherently antigen-specific and are mediated by APCs of the innate immune system, targeting

innate pathways to induce antigen-specific tolerance is a promising approach currently being explored.

One promising strategy to induce antigen specific tolerance is targeting disease relevant antigen to apoptotic cell clearance pathways.[37] Phagocytic cells routinely clear apoptotic debris, such as red blood cells, without eliciting an adaptive immune response. This implies that the antigens from apoptotic debris are processed and presented through innate mechanisms that allow the immune system to recognize these antigens as "self". To harness this tolerogenic pathway, several groups have conjugated disease-relevant antigens to apoptotic splenocytes or red blood cells as a treatment strategy in mouse models of autoimmunity.[38-45] The hypothesis is that because these cells are normally recycled in the spleen at high rates, the antigens will be processed through the same tolerogenic mechanisms and presented by APCs to effector cells in a way that promotes selective tolerance and reverses disease. This strategy demonstrated favorable safety profiles in a clinical setting, but has not progressed since the initial trial in 2013.[42] Thus, further understanding of how tolerance is generated is needed so this strategy can be optimized for clinical translation.

Several labs have shown that targeting clearance mechanisms by encapsulating or displaying self-antigens on nanoparticles or microparticles, instead of apoptotic cells, can be a successful strategy in mouse models of autoimmune disease.[4,46-52] Biomaterials have also been exploited to co-deliver disease relevant antigen with regulatory immune signals to APCs.[53-72] The goal of these strategies is to deliver self-antigens attacked during disease to APCs and have the APCs present self-antigen without co-stimulatory signals. The hypothesis is that inhibiting inflammatory signaling or promoting regulatory signaling while antigen is being processed and presented by APCs will promote presentation of antigen without costimulatory molecules or in other manners that promote tolerance. Then, for example, when T cells bind cognate self-antigen

without co-stimulatory signals, T cells will be inactivated against self-antigen or will be polarized towards regulatory phenotypes that maintain tolerance to self-tissue. To date, antigen-specific specific therapies have shown great promise in pre-clinical models but have not been successfully translated into clinical settings.[42,73-75]

Delivering immune cues to target specific signaling pathways often necessitates the ability to reach spatially restricted tissues or receptors. Given the impact of biophysical properties such as size and surface charge, it is important to design therapies with biophysical features that allow the signals to reach their targets and be biologically available to initiate specific signaling pathways. It also requires a better understanding of the mechanisms that lead to success of these strategies in preclinical models. The current standard of assessing immunological responses to antigen-specific therapies involves general analyses of antibody production, common costimulatory markers expressed by APCs, presence or absence of cytokines associated with inflammation or regulation, and proliferation and polarization of T cells towards inflammatory or regulatory phenotypes. However, as mentioned throughout Chapter 1, the immune system is sensitive not only to the presence of specific signals, but also to biophysical parameters such as binding affinity of T cell receptors for cognate antigen.

Developing a better understanding of how immunotherapies impact molecular interactions between immune cells and how these interactions change as a function of biophysical design parameters could significantly improve our understanding of how to engineer effective antigen-specific therapies. Toward this goal, Chapter 2 reviews how a particular set of biomaterials – self-assembled biomaterials – have been utilized to engineer immunotherapies for cancer and autoimmune disease. The research in Chapter 3 tests the hypothesis that biophysical properties of self-assembled immune signals can be tuned to influence immune cell signaling. We reveal that

immune cues assembled with a relatively lower binding affinity were better able to inhibit inflammatory signaling than immune cues assembled with a relatively higher binding affinity. The research in Chapter 4 utilized molecular dynamics simulations to test the hypothesis that during electrostatic self-assembly, arginine residues facilitate higher binding affinity than lysine residues because arginine can form more electrostatic interactions than lysine. We reveal that peptide antigens with higher total charge or anchored with arginine residues formed more hydrogen bonds and salt bridges than peptide antigens with lower total charge or anchored with lysine residues, respectively. Chapter 5 details ongoing and future research directions to continue developing self-assembly of immune signals as a platform and tool to build next-generation immunotherapies. The dissertation concludes with an Appendix that outlines the contributions to science that resulted from this work, including research publications, conference presentations, and funding sources that supported the dissertation research, followed by a list of references.

CHAPTER 2: SELF-ASSEMBLY AS A MOLECULAR STRATEGY TO IMPROVE IMMUNOTHERAPY[†]

Self-assembling biomaterials are a class of biomaterials that spontaneously assemble in aqueous solution to create entropically favorable structures.[24] The underlying forces driving spontaneous assembly result either from hydrophobic interactions or charge polarity. Hydrophobic interactions have been utilized to create a range of intricate structures, including peptide nanofibers, nanogels, micelle-like particles, and in vivo assemblies with protein carriers to target signals to lymph nodes. There has also been extensive work to develop platforms that utilize electrostatic interactions to drive assembly of oppositely charged immune signals. This platform benefits from the ability to readily tune biophysical interactions between two components by altering the ratio of cationic to anionic charge during formulation, or the density of charge per component.

Chapter 2 explains how hydrophobicity and charge polarity have been exploited to self-assemble engineered materials and immune signals for improving immunotherapies. Self-assembled biotechnologies could help address some of the limitations facing immunotherapies by offering unique capabilities, such as high levels of uniformity and precise control of composition. The creativity of engineered self-assembly has led to some key insights that could benefit future immunotherapies and revealed aspects that need to be more completely understood. The challenge now remains to utilize these insights to push development of new and effective immunotherapeutics into clinical settings.

[†] Adapted from **Froimchuk, E.**, et al. Self-Assembly as a Molecular Strategy to Improve Immunotherapy. *Acc. Chem. Res.* 2020. 53 (11): 2534-45.

2.1) Self-assembled technologies offer unique benefits to improve immunotherapies

Despite the many benefits of biomaterials described in Chapter 1, biomaterials also introduce additional challenges into the clinical translation process. Material formulations are often hindered by inefficient cargo loading or heterogenous distributions in size or other biophysical properties. Inclusion of polymer carriers or heterogenous mixtures can also complicate characterization and assessment of safety required for clinical trials and FDA approval.[76]

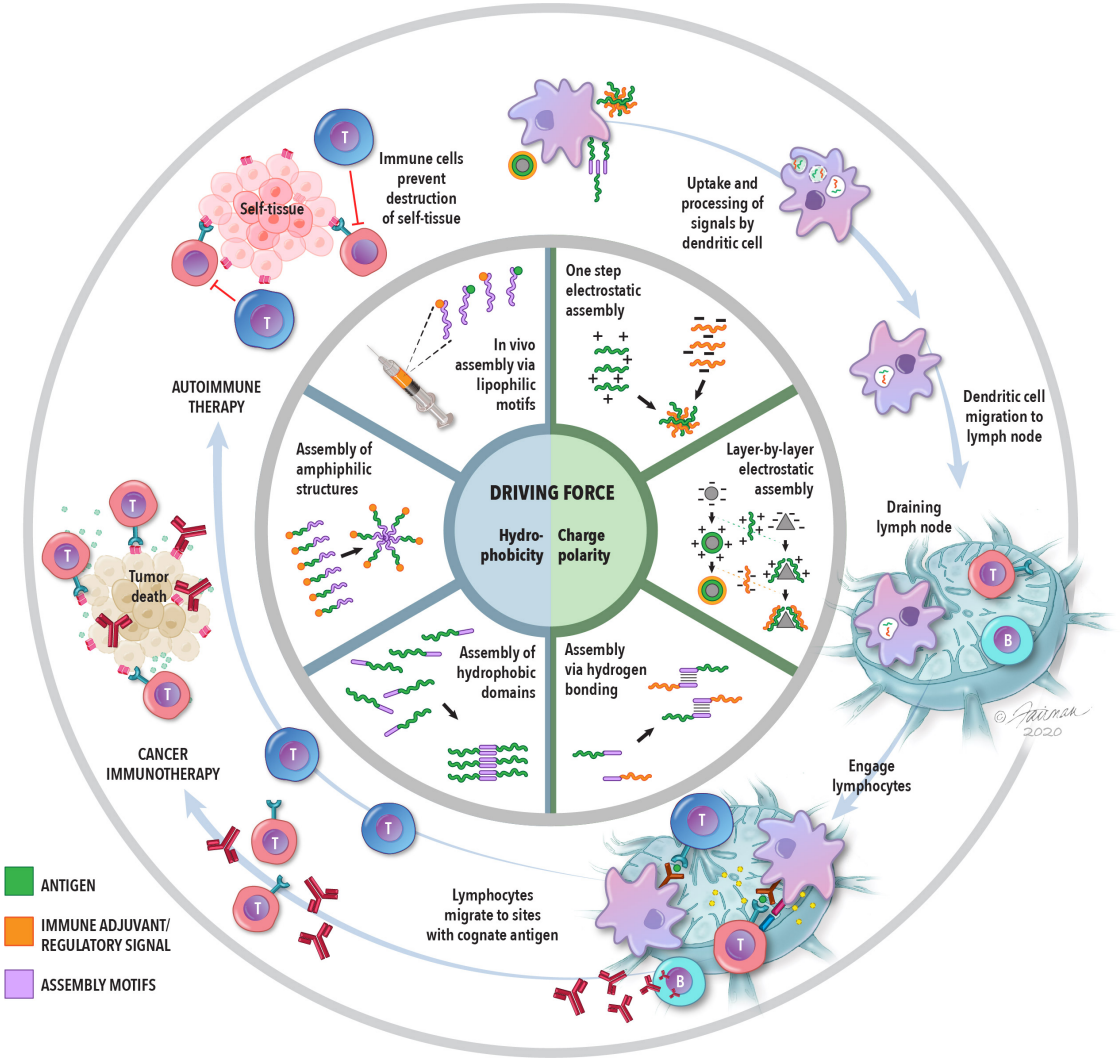

Figure 2. The inner two circles highlight the two main driving forces of self-assembled immunotherapies and the general strategies that have utilized these forces to create self-assembled structures. The outer-most circle illustrates the general strategy of immunotherapies for cancer and autoimmune disease, as described in Chapter 1 and throughout Chapter 2. Self-assembled materials are being explored in all of the stages depicted in the outer-most ring.

Additionally, commonly used biomaterial polymers used to encapsulate therapeutic agents exhibit intrinsic immunogenic features that can elicit inflammation even in the absence of other immune signals.[77,78] These effects can be a confounding variable in developing therapeutic strategies that require precise understanding and control of therapeutic outcomes to establish safety and clinical translation. For example, polymer carriers may impact immune signaling and alter the expected response of the immune signals in the immunotherapy. Considering the challenges just mentioned, Chapter 2 highlights how self-assembling materials offer both the unique benefits of biomaterials, as well as the potential to overcome some of the complexity and formulation limitations described.

Self-assembled materials require little to no additional energy input due to the spontaneous nature of assembly, allowing for facile, low-energy manufacturing methods that are scalable. Further, the precise structures and interactions that govern self-assembly can help reduce heterogeneity and the resulting complications in characterization and loading consistency. Self-assembled materials generally assemble owing to two underlying driving forces: hydrophobic interactions and/or charge polarity (**Fig. 2**). Hydrophobic interactions cause assembly of molecules into entropically favorable states, with hydrophobic regions "hidden" from the surrounding aqueous environment. Charge polarity drives electrostatic adsorption of oppositely charged components, creates a countervailing force that prevents assembly between like-charged components, and allows for hydrogen bonding to occur between polar molecules. The remainder of Chapter 2 highlights how these types of driving forces have been leveraged by the Jewell lab and others to develop self-assembly approaches for candidate immunotherapies and to gain insights that could improve the effectiveness and translatability of future immunotherapies.

2.2) Biomaterials can be designed for self-assembly with hydrophobic domains

One method of driving self-assembly is conjugating biomaterials with hydrophobic motifs, such as the self-assembling peptide Q11 developed by the Collier lab to spontaneously assemble into β-sheet nanofibers.[79] The assembly is driven by the peptide's alternating hydrophobic/hydrophilic primary structure, with all hydrophobic residues positioned on one face of the β-sheet and all hydrophilic residues positioned on the other face (**Fig. 3A)**. Several research efforts have tested Q11's ability to assemble and deliver antigens to APCs to enhance immune responses.[2,20,80-84] These self-assembled structures induced robust antibody responses to the antigen without any additional adjuvants. Adjuvants are stimulatory signals often included in vaccines and immunotherapies to stimulate responses against an antigen of interest. The ability to induce an immune response without addition of adjuvant is an intriguing property that could potentially simplify formulations and limit undesired inflammation caused by off-target effects. This benefit was highlighted in studies where vaccination of mice with peptide nanofibers did not cause swelling (**Fig. 3B**) or accumulation of immune cells and inflammatory cytokines at injection sites, a common side effect with many adjuvants.[83] Additionally, the nanofibers selectively activated dendritic cells, but not macrophages, even though both cell types were able to engulf the nanofibers.[83] The selective activation could be a useful property for directing specific immune responses, which may be more difficult with conventional adjuvants that are broadly stimulatory. Despite the lack of inflammation, the nanofibers were able to activate antigen-specific CD8 T cells, which are important in anti-tumor immune responses.[84] This platform could also be tuned to

generate a particular type of immune response depending on the dose of antigen that was incorporated into the nanofibers. For example, the dose of antigen that maximized helper T cell responses (T_{fh}) important in activating B cells was nearly a magnitude higher than the dose that maximized helper T cells (T_h1) that secrete inflammatory cytokines (**Fig. 3C**).[20] Fibers that formed either α-helical structures or β-sheets both produced antibody responses.[85,86] However, APCs only internalized and presented antigen when nanofibers were positively, but not negatively, charged indicating that surface properties impact the biological responses to the self-assembled structures.[2]

Hydrophobic motifs have also been used to create a variety of other self-assembled structures. Purwada et al created self-assembling protein nanogels containing a polymer backbone with a functionalized hydrophobic pyridine side chain.[87] In the presence of aqueous protein, entropic forces drove the self-assembly of the pyridine groups into an inner layer, while proteins in solution formed the outer layer. Another example from the Akiyoshi lab used cholesterol-

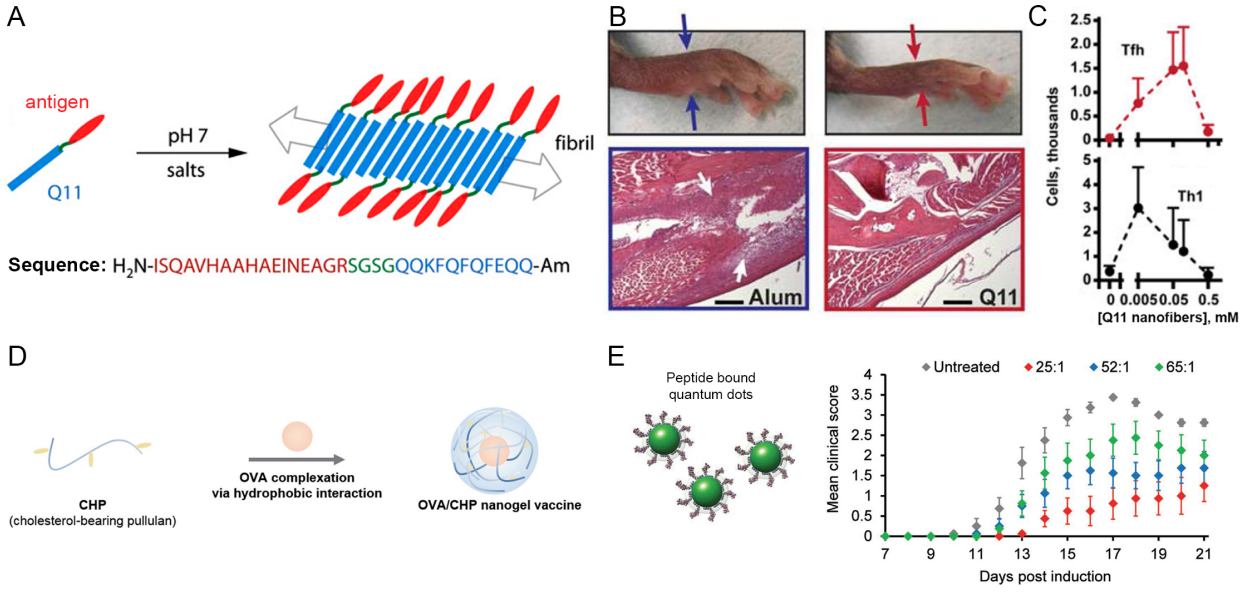

Figure 3. A) Q11 nanofibers conjugated with antigen. B) Reduced swelling in mouse footpads after treatment with Q11 nanofibers (right) compared to treatment containing adjuvant (left). Reprinted from ref. 79 with permission from Elsevier. C) Dose of antigen impacted overall immune response. Adapted from ref. 20 with permission from Wiley. D) Nanogels containing ovalbumin (OVA). Adapted from ref. 88, published by The Royal Society of Chemistry. E) Therapeutic efficacy was altered as a function of antigen density per quantum dot. Adapted from ref. 4 with permission from Wiley.

bearing pullulan to create a self-assembling nanogel incorporating the common protein antigen ovalbumin (**Fig. 3D**).[88] Treatment with nanogels alone or in combination with anti-PD1 antibodies significantly reduced tumor growth in a lymphoma mouse model that expresses ovalbumin, relative to treatment only with anti-PD1 or a combination of soluble ovalbumin and anti-PD1. Interestingly, when the nanogels were modified to increase anionic surface charge, these nanogels were distributed in different areas of lymph nodes compared to the distribution observed with unmodified nanogels, which were near-neutral.[22] The anionic nanogels were internalized more effectively by several distinct subsets of dendritic cells involved in activation of helper T cells and B cells.

The size, shape, and surface chemistry of immunotherapies can all impact biological responses.[1,25] In the case of the Q11 nanofibers, the cationic charge may have facilitated adsorption with the anionic cell membrane and thus improved uptake via non-specific electrostatic interactions. Conversely, the anionic charge of the nanogels could have prevented the non-specific interactions with the cell membrane, resulting in selective uptake by subsets of phagocytic cells. The ability to activate immune responses without additional adjuvants may also be impacted by biophysical properties. For example, immune responses can be activated through recognition of hydrophobic groups,[9] which may contribute to the ability of Q11 nanofibers to generate immune response without explicit adjuvant molecules. However, another study using self-assembled peptide nanovesicles induced strong CD8 T cell responses and delayed tumor growth only when administered with an adjuvant.[89] These nanovesicles exhibited different morphology than the Q11 nanofibers, which might hide hydrophobic motifs in a core, thus preventing or reducing recognition by and activation of immune cells.

In addition to accessibility of molecular motifs in self-assembled materials, the density of immune signals displayed on constructs can also impact response during immunotherapy. The Jewell lab has investigated this idea in the context of immunotherapies for multiple sclerosis.[4] In one set of studies, peptide self-antigens were self-assembled and displayed on quantum dots at defined densities. Mice induced with a mouse model of autoimmunity responded to treatment with quantum dots more efficiently when the dose of peptide was higher. Intriguingly, however, efficacy was inversely correlated with the density at which the peptide was delivered on the quantum dots. At a fixed antigen dose, particles displaying a low density of antigen on a greater number of particles (e.g., 25:1) were more efficacious than particles displaying antigen at a high density on fewer particles (e.g., 65:1), indicated by lower mean clinical scores (**Fig. 3E**). These data suggest that availability of more therapeutic "events" (i.e., particles) may be more effective in modulating the integrated signaling in immune response. This discovery is one example of how self-assembled biomaterials offer unique features to understand the "design rules" that promote tolerogenic processing of antigen by APCs. Elucidating the requisite design parameters will be a crucial aspect of rationally engineering antigen-specific immunotherapies.

2.3) Chemically synthesized amphiphilic molecules form micelle-like particles

Hydrophobic interactions can also be used to self-assemble amphiphilic structures into ordered phases, such as micelle-like structures.[36,90,91] One important area where this idea has been used for immunotherapies is the design of peptide amphiphiles composed of a hydrophobic, lipid-like tail that is linked to a hydrophilic peptide headgroup.[36] In aqueous conditions, the peptide amphiphiles self-assemble into micelles, burying the hydrophobic tails within the core while the hydrophilic headgroups are displayed on the surface.

Toward a standardized platform for manufacturing personalized cancer vaccines, the Seder lab recently developed antigen-adjuvant conjugates that self-assemble into micelle-like particles of uniform size, irrespective of the antigen sequence.[36] The self-assembly was driven by charge-modified peptide sequences and hydrophobic oligopeptides that were anchored to the C and N termini via enzyme degradable linkers. The hydrophobic blocks were further linked to a defined number of small molecule adjuvants specifically selected based on their hydrophobic properties and ability to drive T cell response. Upon resuspension in aqueous solution, the hydrophobic components promoted assembly of micelle-like structures, while the charge modifying groups established uniform surface charge that provided a countervailing force to prevent formation of aggregates (**Fig. 4A**). The micelles could incorporate a range of different tumor-specific antigens and adjuvants without disturbing the integrity of the particles. Furthermore, the micelle platform improved loading of antigens compared to other commonly used biomaterials, such as poly(lactic co-glycolic acid) or liposomes, where loading varied between different antigens and can sometimes vary batch to batch. Micelles conferred markedly improved efficacy in mouse models of skin and lung cancer relative to administration of soluble antigen and adjuvant (**Fig. 4B**). Importantly, vaccination of non-human primates with micelles activated both CD4 and CD8 T cell responses, a promising indicator that this platform has potential for application in clinical settings.

The development of this micelle platform is exciting, representing a standardized formulation approach that successfully incorporates a range of antigen and adjuvants. The consistent assembly of particles irrespective of composition is important for overcoming downstream hurdles specific to manufacturing and regulatory characterization. From a clinical perspective, the ability to incorporate a range of tumor-specific antigens is also relevant for personalized cancer therapies, which seek anti-cancer immune responses without side effects or alteration to healthy immune function. Combining such approaches with technologies to identify tumor-specific antigens could represent a new paradigm for cancer immunotherapy.

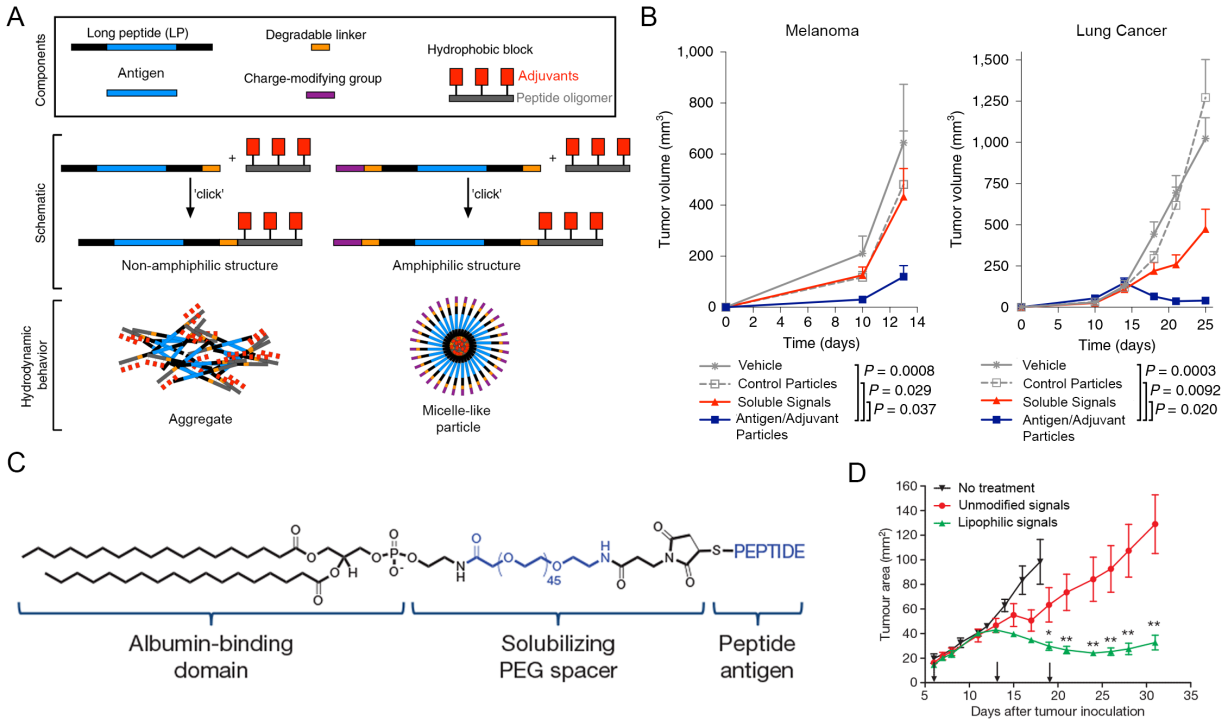

Figure 4. A) Micelle-like particles containing antigen and adjuvant. B) Reduction in tumor volume in two models of cancer after treatment with micelle-like particles (blue). A+B are adapted from ref. 36. C) Structure of lipophilic molecules. D) Reduction in tumor volume after treatment with lipophilic antigen and adjuvant. C+D adapted from ref. 92 with permission from Springer Nature.

2.4) Lipophilic motifs promote in vivo self-assembly with protein carriers

Hydrophobic interactions can be leveraged within the body to target immunotherapies more efficiently to lymph nodes, increasing their potency. One strategy draws on the ability of lipophilic moieties to self-assemble with protein carriers, such as albumin. Albumin is a natural transporter molecule that shuttles cargo in the body to lymph nodes. Liu et al first discovered the promise of an "albumin hitchhiking" idea by modifying a stimulatory adjuvant and other antigens with lipophilic motifs (**Fig. 4C**).[92] These signals drained more efficiently to lymph nodes and decreased systemic toxicity compared to unmodified components, which were not concentrated in lymph nodes. By investigating the fate of these lipophilic structures, the authors discovered that lymph node resident dendritic cells must cleave the bond between peptide and amphiphile before presenting the antigen to T cells. Because of improved lymph node targeting and subsequent presentation, T cells specific for the antigen were proliferated and inflammatory cues increased. When mice bearing skin or metastatic lung cancers were vaccinated with these immunotherapies, survival was significantly improved (**Fig. 4D**). Zhu et al built on this idea using Evan's blue, a clinical lymphatic tracer dye, as an albumin-binding domain due to its established safety profile.[93] A lipophilic construct was created by conjugating the dye with an adjuvant. Co-delivery of this construct with a model antigen to mice resulted in a four-fold increase of antigen-specific CD8 T cells relative to an oil-in-water emulsion of antigen, which is a current benchmark for vaccination in these pre-clinical studies.

This albumin hitchhiking approach significantly improved the efficacy of a cancer immunotherapy in a mouse cancer model. Building off their prior work, Appelbe et al combined albumin-complexed adjuvant with radiation to improve cancer immunotherapy.[94] In healthy vasculature, albumin is too large to drain out of blood vessels and instead is selectively processed

through lymphatics.[93] However, when a tumor is irradiated, the vasculature becomes more permeable. With this increased permeability, lipophilic adjuvant delivered intravenously binds to albumin and accumulates in tumors. The authors showed that this targeted accumulation increased inflammatory responses in the tumor environment and reduced systemic toxicity. This body of work suggests potential for in-vivo assembly of hydrophobic domains to increase potency of existing immunotherapies. Lipophilic modifications for lymph node targeting offer promise as a flexible platform by modifying different combinations of adjuvants and antigens. The flexibility of this system could be useful for modifying and improving other immunotherapies for cancer, as additional immune signals help amplify the immune response at the tumor site. Conversely, efforts could also explore targeting of signals to lymph nodes to direct immune responses away from inflammation that causes autoimmune disease. Additionally, the facile formulation and ability to modify different antigens could enable better precision in production, purity, and screening of future immunotherapeutics.

2.5) Hydrogen bonding is a driving force with abundant engineering potential

Recent studies have utilized hydrogen bonds to create intricately self-assembled structures for immunotherapies.[95-100] For example, one group utilized lipid-modified DNA sequences and either adjuvant and/or antigen sequences that were elongated with a complementary sequence to the DNA.[96,97] Hybridization of DNA and its complementary sequence on the elongated immune signals facilitated assembly of components into nanoparticles. Another approach developed an antigen aptamer-adjuvant fused sequence that integrated into DNA hydrogels via hybridization with a DNA linker.[98] When administered to mice in combination with doxorubicin, the hydrogel induced an inflammatory immune response and decreased tumor growth in a breast cancer model. Most recently, Li et al utilized hydrogen bonding to create a treatment employing immunotherapy,

chemotherapy, and radiation therapy all in one.[100] Particles were composed of diselemide, which is an inhibitor of antigen presentation, and pemetrexel, an approved chemotherapy. The two drugs self-assembled due to triple hydrogen bonds between the cytosine on diselemide and guanine on pemetrexel. Until recently, hydrogen bonding has scarcely been used as the main driving force for self-assembly of immunotherapies. However, as evidenced by natural phenomena such as formation of the DNA helix, hydrogen bonds have the capacity to facilitate assembly of highly intricate and stable natural structures. Further exploration of hydrogen bonding in bioengineering contexts could reveal novel assembly strategies for development of controlled and precisely tuned immunotherapies.

2.6) Alternating cationic and anionic moieties allows for layer-by-layer electrostatic assembly

Electrostatic interactions are a powerful driving force that can facilitate assembly of anionic and cationic components into layered structures. By alternating cationic and anionic layers, facile assembly of these structures can be achieved. This strategy has been employed in the development of immunotherapeutics to create polyelectrolyte multilayer (PEM) capsules. Earlier work established that PEMs could encapsulate antigen by coating antigen-loaded calcium carbonate particles with alternating layers of anionic dextran sulfate and cationic polylysine polymers. The calcium carbonate was subsequently dissolved out to create PEM capsules with antigen in their core.[101] Compared to vaccination with soluble antigen, PEMs improved delivery of antigen to antigen presenting cells and generated immunity in mice against melanoma.[102] Subsequently, PEMs were developed by incorporating an adjuvant as the anionic layer. The PEM capsules could induce antigen presenting cell and T cell activation in response to antigen and adjuvant within the capsules.[103] Whereas past systems incorporated polymers or other materials as structural components, our lab has recently developed PEMs composed entirely of immune

signals.[104] To support assembly, these immune polyelectrolyte multilayers (iPEMs) were composed of peptide antigens anchored with cationic amino acids on the C-terminal end and anionic nucleic-acid based adjuvants coated on gold nanoparticles using a layer-by-layer assembly process. These iPEM-coated nanoparticles induced antigen-specific T cell activation in mice after vaccination, indicating both signals remained bioactive after being assembled in iPEM coatings. Further, the responses generated by iPEMs were more potent than those observed when mice received vaccines containing equivalent doses of soluble signals not assembled into iPEMs.

Commonly used biomaterial polymers used to encapsulate therapeutic agents exhibit intrinsic immunogenic features that that can elicit inflammation even in the absence of other immune signals.[77,78] These effects can be a confounding variable in developing therapeutic strategies that require precise understanding and control of therapeutic outcomes to establish safety and clinical translation. With this challenge in mind, our lab developed stable iPEM capsules that did not rely on a particle core.[105-108] This was achieved by assembling alternating layers of cationic peptide antigens and anionic adjuvants on a calcium carbonate template. The template was then dissolved out to create hollow capsules composed entirely of the immune signals (**Fig. 5A**). These structures juxtapose immune signals at tunable ratios with 100% cargo loading; this is unique relative to polymer or lipid-based particles in which the carrier represents a significant fraction of the formulation. In a melanoma mouse model, mice vaccinated with iPEMs containing antigen and adjuvant significantly slowed tumor growth and increased median survival time (**Fig. 5B**).[105]

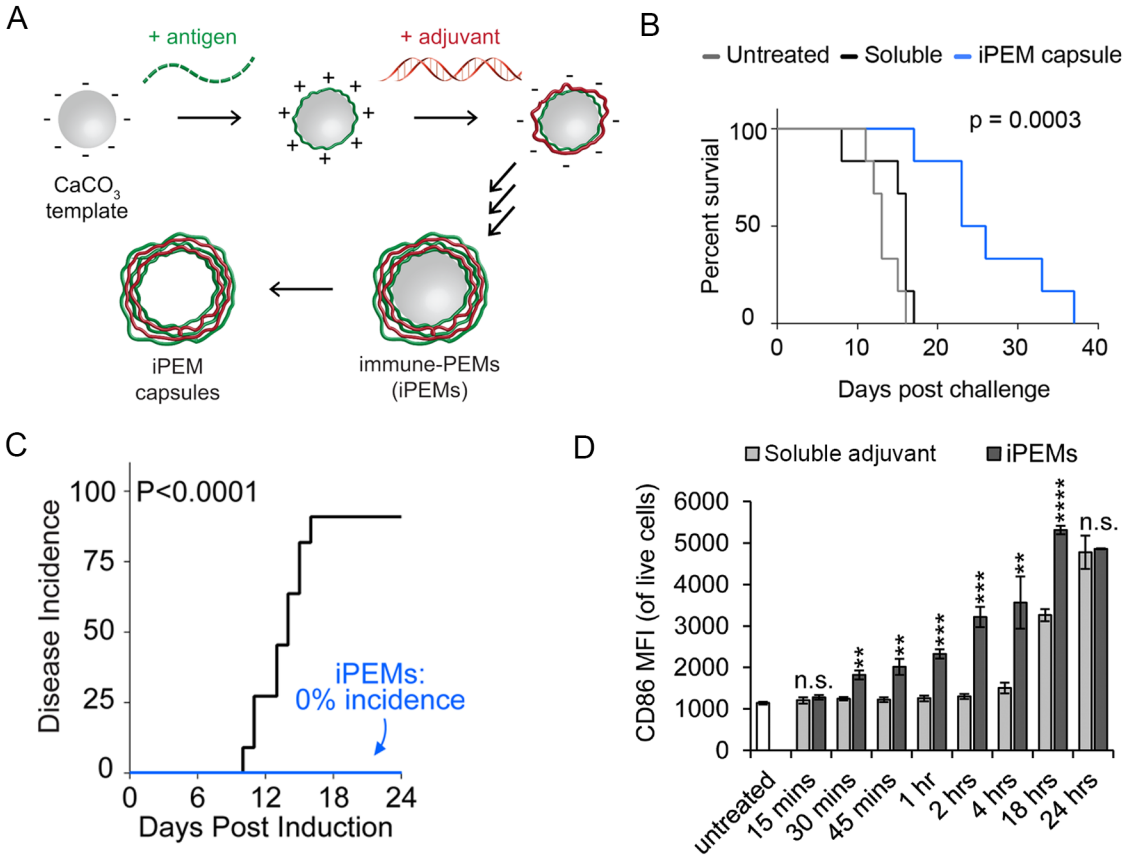

Figure 5. A) Assembly of iPEMs B) Treatment with iPEMs lengthened survival time in a mouse tumor model. A+B are adapted from ref. 105. C) iPEMs completely prevented onset of disease in a mouse model of multiple sclerosis. Adapted from ref. 106. Further permissions related to material excerpted should be directed to ACS. D) iPEMs activated DCs faster than soluble adjuvant, measured by expression of the activation marker CD86. Adapted from ref. 112 with permission from Wiley.

Because of the modular assembly of iPEMs, we have also been able to easily extend the concept to autoimmune disease and promotion of immunological tolerance.[106,108] The goal of immunotherapies for autoimmune disease is to deliver self-antigens attacked during disease to antigen presenting cells and have the cells present self-antigen without co-stimulatory signals. The hypothesis is that when T cells bind cognate self-antigen without co-stimulatory signals, T cells will not become activated or will be polarized towards regulatory phenotypes that maintain tolerance to self-tissue. To achieve this outcome, we developed iPEMs composed of antigen targeted by T cells in a mouse model of multiple sclerosis and a regulatory immune signal that

inhibits an inflammatory pathway that is active during autoimmunity. In vitro studies indicated that iPEMs successfully inhibited presentation of co-stimulatory signals by dendritic cells and reduced antigen-specific T cell activation in response to cognate antigen. When tested in vivo, iPEM treatment completely prevented disease in mice (**Fig. 5C**), establishing the promise of this platform to promote tolerance.

From a manufacturing perspective, iPEMs are relatively simple compared to other common formulation methods that involve complex polymers or excipients and additional energy input for encapsulation of immune signals. We have shown that assembly of iPEMs is pH dependent with respect to both antigen and adjuvant components, and the relative loading of both components can be tuned by controlling the pH.[109] With increasing understanding of the engineering criteria that drive assembly, iPEMs create the possibility of incorporating and delivering a range of antigens and adjuvants with control over the relative combinations of signals.

Other aspects of immunotherapies, such as cellular trafficking and route of injection, are also important to understand to develop clinically relevant therapies.[23,110] We have shown that the signals delivered by iPEMs were co-localized in lymph nodes and induced more potent T cell activation than when signals were delivered in soluble form.[111] Using quantitative analysis, we have also confirmed that 95% of cells that contained at least one signal present in iPEMs (i.e., antigen or adjuvant) also contained the other signal.[109] iPEMs also activated dendritic cells faster than soluble signals (**Fig. 5D**) and quickly trafficked through endosomal/lysosomal pathways involved in antigen presentation.[112] These are desired outcomes to achieve efficient delivery of immunotherapeutics that target endosomal receptors such as toll-like receptors. Utilizing layer-by-layer assembly, the Hammond lab recently revealed that targeting of particular cells and trafficking pathways can be tuned as a function of the surface chemistry.[113] This observation is intriguing as

it indicates that the choice of signals incorporated into iPEMs can be extended to target a broad range of pathways with the right design. Thus, iPEMs mimic key benefits of micro- and nanoparticles, such as co-delivery of signals and rapid internalization, but eliminate some of the disadvantageous. For example, iPEMs do not have additional components that could exhibit carrier effects or create intrinsic immunogenicity; the latter could be problematic in exacerbating autoimmune diseases.

In addition to some of the targeting concepts discussed above, the route of administration can impact this aspect. In particular, the skin is an environment rich with immune cells, and thus has significant potential for immunotherapies. For example, intradermal injection often leads to efficient immune responses relative to intramuscular or subcutaneous injections, and we have seen similar effects with iPEM capsules.[114] It is not surprising then that microneedle patches have seen increasing interest as alternative technologies to needle-based injections. These patches utilize polymer needles that are long enough to penetrate the skin but too short to reach pain receptors. Thus, microneedles allow pain-free treatment, and more specifically for immunotherapy, efficient delivery to the immune cell-rich dermal layer. The Irvine and Hammond labs employed layer-by-layer assembly to develop microneedles coated with polycationic polymers, anionic nucleic-acid based adjuvant, and plasmid DNA encoding a model antigen for transfection of antigen presenting cells in the skin.[115] Microneedles successfully delivered cargo to antigen presenting cells in the dermal region of mice and non-human primates. In these studies, UV light was used to activate the surface of the microneedles and initiate release of the layers from the microneedle surface. In an attempt to develop more practical methods of cargo release, the Hammond lab recently developed charge invertible microneedles that rapidly released the signals upon insertion into the skin (**Fig. 6A)**.[116] Charge inversion due to the shift to physiological pH resulted in three consecutive layers

of negative charge that strongly repelled each other and detached the film from the microneedle surface within one minute (**Fig. 6B)**. These microneedles efficiently delivered antigen to APCs in mice, induced a strong antibody response, and were able to deliver adjuvant to APCs in human skin ex vivo.

Our lab recently applied iPEM coatings on microneedles for cancer vaccination (**Fig. 6C**).[117] The advantage of iPEMs in this context is the ability to concentrate tumor antigens and adjuvants to specialized immune cells in the skin. For the specific application of melanoma, skin delivery is also relevant because the skin is the location of many melanomas. Upon vaccination of mice with microneedles coated with a human melanoma antigen and adjuvant, the signals were co-localized at the site of injection. T cells specific for the melanoma antigen expanded over 4 weeks in response to a prime-boost immunotherapy strategy (**Fig. 6D)**, indicating the iPEM-coated

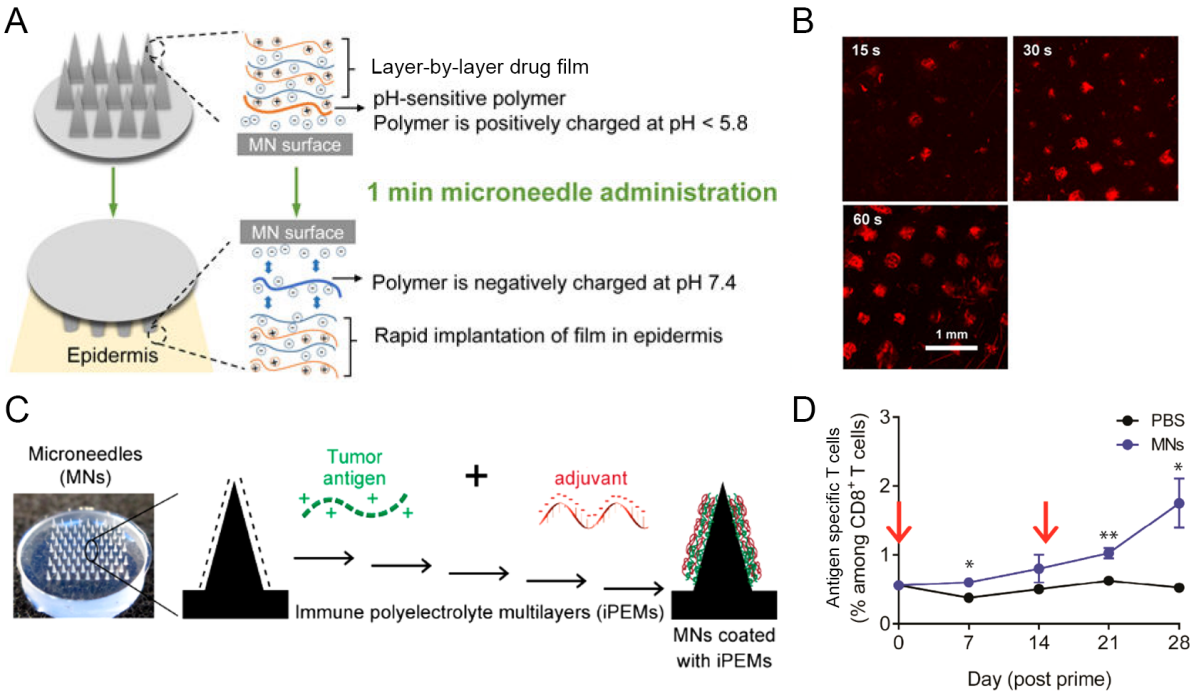

Figure 6. A) Charge invertible microneedles. B) Release of microneedle films (red) into the skin of mice. A+B adapted with permission from ref. 116. Copyright 2018 American Chemical Society. C) iPEM coated microneedles. D) Expansion of melanoma specific T cells after microneedle vaccination. C+D adapted from ref. 117.

microneedles promoted a tumor-specific immune response against the melanoma antigen. Studies from our lab indicate that modulation of immune responses over extended periods of time can be achieved by controlling the release kinetics of iPEM films.[118] Thus, an interesting direction could be the development of rapidly releasing but slowly degrading iPEM films that release from microneedle substrates to form depots of immune signals within the dermal layer and modulate immune responses over time.

2.7) One step electrostatic adsorption provides a facile method of conjugation

Another self-assembly approach is to simply mix two oppositely charged components in aqueous solution, allowing electrostatic interactions to drive self-assembly into entropically favorable complexes. Historically, these structures – formed from oppositely-charged polymers – are termed polyplexes. Several efforts have used electrostatic assembly to adsorb antigen and/or adjuvants with preformed carrier components, such as micelles or nanofibers.[119-123] A common observation among these studies is improved T cell activation and higher antibody titers compared to when antigen and adjuvant are delivered in soluble form. This recurring observation further highlights the importance of co-delivering immune signals and delivery in a particulate form to increase signal potency.

Our lab has used electrostatic assembly to create complexes composed entirely of immune signals by incubating oppositely charged signals in aqueous conditions.[72,124-127] For example, using analogous signals discussed above for iPEMs, these polyplex-like structures can be created from self-antigens and regulatory immune signals to combat autoimmune disease (**Fig. 7A**).[72] Compared to layer-by-layer assembly, this approach sacrifices the ability to control the relative loading of multiple signals but simplifies assembly into a single step. However, these complexes still retain other benefits, such as eliminating any confounding carrier effects, enable co-delivery of signals,

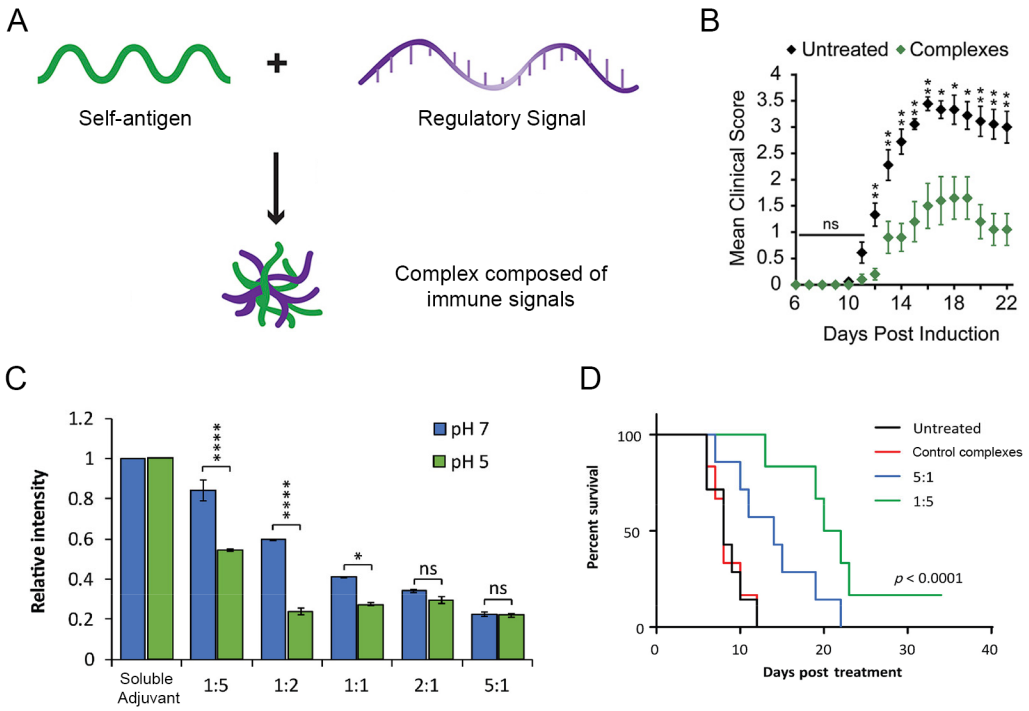

Figure 7. A) Complexes for autoimmune disease. B) Treatment with complexes reduced severity of disease, indicated by reduced mean clinical score. A+B adapted from ref. 72 with permission from Elsevier. C) Relative intensity decreased as cationic to anionic charge ratio increased, indicating stronger binding of adjuvant at higher ratios. D) Cancer survival after treatment with complexes. C+D adapted from ref. 125 with permission from Springer Nature.

and allowing 100% of the administered dose to be therapeutic cargo (i.e., no carrier). Treating mice with complexes in a mouse model of multiple sclerosis reduced the severity of disease over time (**Fig. 7B**), highlighting the method's potential for therapeutic application. Mechanistic studies using this one-step approach revealed some interesting correlations between biophysical properties during complex formation and biological effects. For example, a binding assay indicated high cationic to anionic charge ratios resulted in stronger adjuvant binding (**Fig. 7C**).[125] However, complexes assembled with a low cationic to anionic charge ratio were more effective in prolonging survival in a melanoma mouse model (**Fig. 7D**). Reconciling these findings revealed high cationic to anionic charge ratio could result in tighter binding but hindered accessibility and functionality of the signals in therapeutic settings. Thus, the studies revealed a balance between driving forces

needed to promote assembly and the need to maintain accessibility of the cargo to promote desired immunotherapeutic functions.

2.8) Self-assembled complexes composed of immune cues promote tolerance in a model of autoimmunity

The dissertation research covered in Chapters 3 and 4 was motivated in large part by the results just reviewed in Chapters 2.6 and 2.7. This section describes some additional technical background and previous work from our lab completed by Hess et al., that directly preceded the dissertation work covered in the subsequent chapters.

Our lab developed self-assembled complexes composed of a myelin self-antigen (MOG) attacked during multiple sclerosis and GpG, an oligonucleotide sequence that acts as an antagonist to toll-like receptor 9.[72] As mentioned in Chapter 1, toll-like receptors are a family of receptors found in innate immune cells that recognize molecular patterns common in foreign pathogens but uncommon in humans. Activation of these receptors induces inflammatory signaling and activation of an inflammatory immune response. Interestingly, studies have revealed that toll-like receptors are overexpressed in multiple sclerosis and other human autoimmune diseases, as well as pre-clinical models.[128-137] For example, in a pre-clinical mouse model of multiple sclerosis, disease is significantly reduced in mice without toll-like receptor 9 (TLR9) (**Fig. 8A)**. Further, disease is eliminated in mice without MyD88, one of the main adaptor proteins in multiple toll-like receptor signaling pathways.[131] This example highlights the importance of toll-like receptor signaling in driving disease. Motivated by these findings and others, inhibition of toll-like receptor signaling has been studied as a therapeutic strategy to promote tolerance in the context of autoimmune disease. One group has shown that repeated treatments with GpG modestly attenuates disease severity in a mouse model of multiple sclerosis (**Fig. 8B**).[138] Induction of tolerance was

further enhanced when GpG was co-delivered with plasmid DNA that encodes self-antigen that is targeted during disease (**Fig. 8C**).[139]

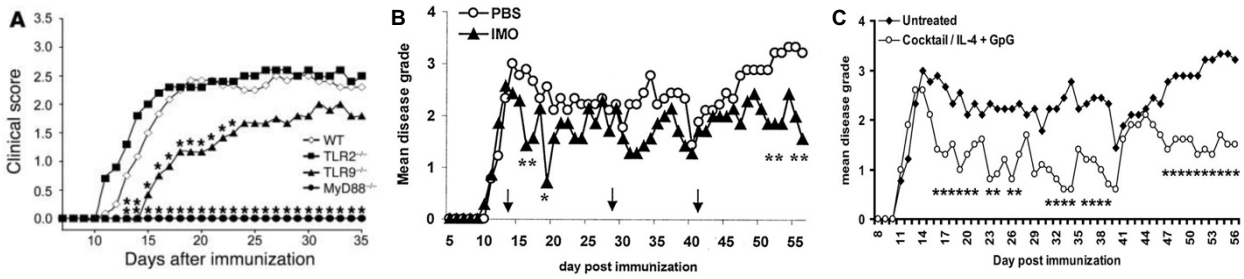

Figure 8. A) Disease progression is reduced in TLR9 knockout mice and completely prevented in MyD88 knockout mice. B) Treating mice repeatedly with GpG (IMO) reduced severity of disease compared to PBS controls. C) Treating mice with GpG and a cocktail containing plasmid DNA that encodes self-antigen reduced severity of disease compared to untreated controls.

Motivated by these findings, our lab reasoned that juxtaposing MOG and GpG in nanoparticle complexes might reduce inflammatory signaling during processing and presentation of MOG by APCs.[72] Owing to this blunted toll-like receptor signaling, T cells reactive against MOG might then be biased away from differentiating toward inflammatory phenotypes (e.g., T_H1, T_H17) associated with autoimmune disease and towards regulatory phenotypes (e.g., T_{REG}) associated with tolerance. MOG peptide antigens were anchored with cationic arginine residues to increase positive charge of the peptide sequence and facilitate self-assembly with negatively charged GpG via electrostatic interactions. Complexes were created over a range of MOG:GpG mass ratios and characterized before testing *in vitro* and *in vivo*.

To determine how uptake of complexes impacted activation of dendritic cells (DCs), DCs were treated either with CpG, CpG + GpG, CpG + soluble MOG peptide, or CpG + MOG/GpG complexes. CpG is a DNA motif common in bacteria that activates toll-like receptor 9 signaling and induces APCs to express co-stimulatory markers, such as CD80, CD86, and CD40. DCs treated with CpG alone or CpG + soluble MOG peptide expressed high levels of CD80 (**Fig. 9A**)

and CD40 (**Fig. 9B**). DCs treated with CpG + GpG expressed baseline levels of CD80 and CD40, indicating that GpG inhibited activation of DCs by CpG. DCs treated with CpG + MOG/GpG complexes expressed lower levels of CD80 and CD40 than DCs treated with CpG alone. These results indicated that MOG/GpG complexes impeded toll-like receptor 9 activity in DCs in the presence of CpG. Expression levels of CD80 and CD40 were variable depending on the MOG:GpG mass ratio and whether MOG was anchored with one or two arginine residues. This observation was one preliminary indicator that the design of complexes may impact processing of the signals by DCs.

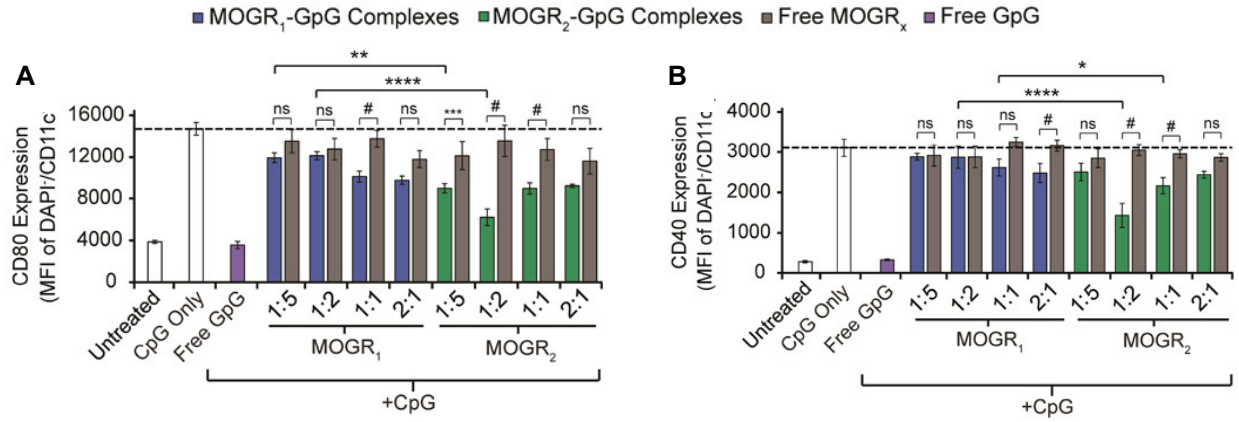

Figure 9. Expression of A) CD80 and B) CD40 by DCs measured by flow cytometry. Statistics were analyzed by One-way ANOVA with Tukey post-test to correct for multiple comparisons. *p<0.05, **p<0.01, ***p<0.001, #p<0.0001, ns = not significant

After determining that MOG/GpG complexes reduced expression of co-stimulatory markers on the surface of DCs, this change in DC phenotype was tested on T cell proliferation and phenotype. DCs were treated in the same manner as described above. After 24 hours, MOG-specific T cells were added to the samples and the T cells and DCs were co-cultured for 48 hours. After 48 hours, the T cells were analyzed by flow cytometry to assess proliferation and phenotype. In samples that were treated with CpG + MOG/GpG complexes, T cell proliferation was reduced compared to samples that were treated with CpG + soluble MOG antigen (**Fig. 10A**). Additionally,

in samples that were treated with CpG + MOG/GpG complexes, fewer inflammatory T_H1 T cells were found compared to samples that were treated with CpG + soluble MOG antigen (**Fig. 10B**). These results indicated that in samples treated with CpG + MOG/GpG complexes, DCs presented MOG to T cells in a manner that reduced T cell activation. Again, there were some differences in T cell proliferation depending on the MOG:GpG mass ratio and whether MOG was anchored with one or two arginine residues. Importantly, this observation was a preliminary indicator that the design of antigen sequence may impact how antigen is processed and presented by DCs to T cells.

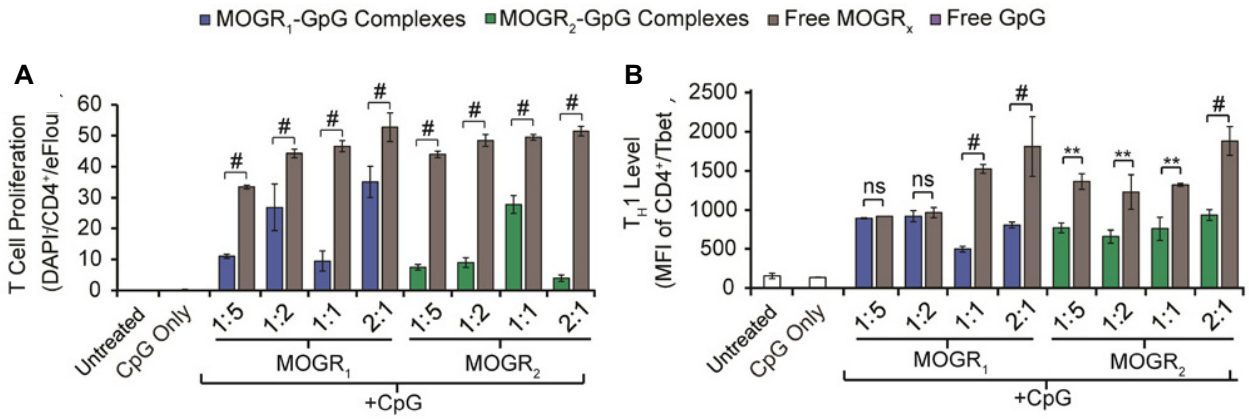

Figure 10. A) Proliferation and B) T_H1 phenotype of MOG-specific T cells after incubation with DCs for 48 hours. Statistics were analyzed by One-way ANOVA with Tukey post-test to correct for multiple comparisons. **p<0.01, #p<0.0001, ns = not significant

After observing that MOG/GpG complexes reduced inflammatory signaling in DCs and T cells *in vitro*, complexes were tested in vivo to determine their potential as a treatment strategy for multiple sclerosis. Mice were induced with disease on days 0 and 1 and then treated with complexes on days 6, 12, and 18 (**Fig. 11A**). Starting on day 6, mice were monitored for disease progression by assessing mean clinical score, where increased disease severity is indicated by increasing clinical scores. Compared to untreated controls, complexes ameliorated disease progression over the course of the study (**Fig. 11B**) and reduced overall severity of disease, measured by the maximum clinical score (**Fig. 11C**). These studies showed that co-delivering

MOG antigen and GpG promoted tolerance in mice and could be a useful platform for studying how design parameters impact immunological outcomes *in vivo*.

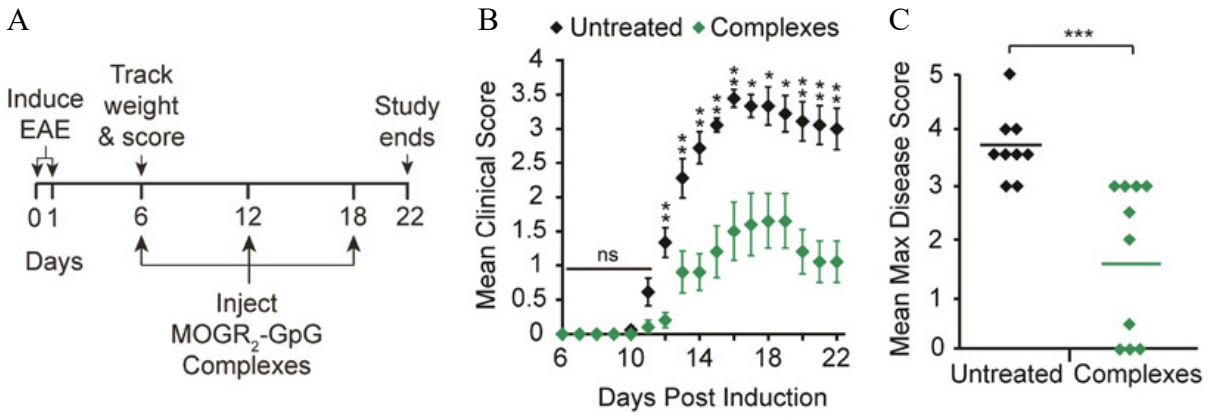

Figure 11. A) In vivo timeline indicating time of disease induction and treatment over the course of the study. B) Average mean clinical scores in mice treated with complexes and untreated controls over the course of the study. C) Average maximum disease score of mice treated with complexes and untreated controls. n= 8-10 mice for all studies. Unpaired t-tests were used to compare clinical scores between groups. *p<0.05, **p<0.01, ***p<0.001, ns = not significant

Taken together, we have seen promising results indicating that MOG/GpG complexes can reduce inflammatory signaling in DCs and T cells and promote tolerance in an autoimmune disease setting. However, we do not understand what was driving the differences observed in the *in vitro* studies and therapeutic effects were only partially effective after three administrations. To achieve more robust efficacy and to be able to generalize this platform to other autoimmune settings, a better understanding of how to design immune signals for self-assembly is needed. As discussed in Chapter 3, we addressed this issue by using MOG/GpG complexes as a platform to better understand specific molecular principles that for the first time connect engineered antigen structure, biophysical properties of the resulting immunotherapies, and ultimately the immune outcomes.

2.9) Computational modeling can help understand interactions between charged molecules

Employing established computational modeling techniques could help shed light on how the biophysical properties of immune signals impact self-assembly. For example, one recent study used molecular dynamics simulations to observe and quantify how arginine and lysine interact with the cellular membrane.[140] This model revealed that arginine can attract more phosphate groups and water molecules in the membrane due to its ability to form more hydrogen bonds than lysine. A similar type of analysis discussed in Chapter 4 provided insight into how changing the amino acid anchored to peptide antigens from arginine to lysine changed the interactions between immune signals during self-assembly. Another recent study used field-theoretic simulations to study how two oppositely charged polyelectrolytes interact in a polar solution.[141] Some important variables in the model are length of the polyelectrolytes, charge of the polyelectrolytes, charge density within the polyelectrolytes, and overall number of each polyelectrolyte in solution. The model described at what point coacervation occurs, a phenomenon describing the phase-separation of oppositely charged species in aqueous solution. The phase separation creates two distinct "phases" in solution: a concentrated aqueous phase containing the charged species and a dilute aqueous phase that is mostly devoid of the charged species.[142] The authors discussed how this approach could be extended to more complex models that include salt ions in solution or different charge densities and chain lengths. Similar analyses methods could be applied to MOG/GpG complex formation, where cationic peptide antigen and anionic oligonucleotide are mixed in water to facilitate self-assembly. Chapter 3.3.4 mentions the possibility of coacervates forming with the neutrally charged MOG/GpG complexes.

As highlighted throughout Chapter 2, strategies utilizing self-assembly benefit from facile, low energy manufacturing methods that result in consistent and controlled formulation of immunotherapies. These self-assembly strategies harness hydrophobicity and charge polarity as driving forces to spontaneously assembly immune signals and other biomaterials in aqueous solution. Certain self-assemblies with hydrophobic domains uniquely benefit from the ability to stimulate immune responses in specific immune cells without additional adjuvants. This aspect can reduce broad inflammation but may also limit what parts of the immune system can be targeted with this strategy. Assemblies utilizing electrostatic interactions benefit from the ability to easily tune biophysical interactions between two charged components by simply changing the charge density of each component or the ratio of the two components in solution. However, the design principles may be limited by their effect on the functionality of the signals after assembly. Electrostatic assemblies may benefit from utilizing hydrophobic and/or hydrogen bonding motifs that stabilize formulation and increase the capacity to incorporate a range of signals. Understanding how charge polarity and hydrophobicity can be utilized together can position self-assembly to be a powerful modality for the development of new and improved immunotherapies.

CHAPTER 3: BIOPHYSICAL PROPERTIES OF SELF-ASSEMBLED IMMUNE SIGNALS IMPACT SIGNAL PROCESSING AND THE NATURE OF REGULATORY IMMUNE FUNCTION[‡]

As reviewed in Chapters 1 and 2, antigen-specific therapies have not been successful in patients with autoimmunity,[42,73-75] in part due to the difficulty of targeting immune cues to spatially restricted receptors on and within immune cells. Whether the immune system elicits inflammation or tolerance against self-antigens depends on how self-antigens are encountered and the immune cues integrated during antigen presentation, such as toll-like receptor signaling. Elucidating specific links between biophysical properties and immune interactions could provide more sophisticated levers to direct innate and adaptive immune response for rational control of clinical outcomes. Thus, technologies that enable more precise control over immune signal integration would be transformative for autoimmune therapies.

3.1) Leveraging self-assembly to study the links between biophysical design and immune outcomes

Self-assembled materials offer some unique properties to address the gap mentioned above, including definable molecular structures and homogenous compositions (see Chapter 2).[24] We posited that these capabilities could be used to connect structural features that drive self-assembly to biophysical properties, and ultimately, to the resulting innate and adaptive immune functions. As reviewed in Chapter 2.8, we recently showed complexes formed from a regulatory toll-like receptor 9 ligand (GpG) and a self-antigen (MOG) attacked during multiple sclerosis improve paralysis in a mouse model of multiple sclerosis.[72] However, the selectivity of this tolerance is unknown. Here, we first show efficacy depends on the presence of myelin-relevant antigen (i.e., MOG) in a mouse model of multiple sclerosis. Building on this exciting result, we used these

[‡] Adapted from **Froimchuk, E.**, et al. Biophysical properties of self-assembled immune signals impact signal processing and the nature of regulatory immune function. *Nano Letters.* 2021. 21 (9): 3762-71.

immune signals as the base to create a library of complexes assembled from anionic GpG and cationic MOG peptides; the latter were designed with specific charge densities by anchoring cationic amino acids to MOG. We hypothesized modifying MOG on the C-terminus with these anchors – rather than throughout the sequence – would allow electrostatic assembly without impacting the fidelity of MOG antigen presented to T cells by APCs. We show the molecular features and charge densities of the anchors control biophysical properties of self-assembled complexes, including binding affinity between MOG peptides and GpG, and complex surface charge and diameter. These changes resulted in altered processing by innate immune cells and controlled the polarization of MOG-specific T cells between regulatory and inflammatory phenotypes. Intriguingly, MOG peptide designs that drove assembly with weak binding affinities resulted in better inhibition of inflammatory gene expression in DCs shortly after uptake and the greatest polarization towards regulatory T cell phenotypes. These results suggest important design criteria for material assembly, immune signal availability, and the resulting immune outcomes.

3.2) Materials and Methods

3.2.1) Materials

GpG DNA (5'-T*G*A*C*T*G*T*G*A*A*G*G*T*T*A*G*A*G*Z*T*G*A*-3') and CpG DNA (5'-T*C*C*A*T*G*A*C*G*T*T*C*C*T*G*A*C*G*T*T*-3') were purchased from IDT (Coralville, IA). Biotinylated GpG was synthesized with a biotin tag on the 5' end. MOG (MEVGWYRSPFSRVVLHLYRNGK) and SIINFEKLR$_9$ (SIINFEKLRRRRRRRRR) were synthesized by Genscript (Piscataway, NJ). MOG peptides were anchored with either 2, 3, or 9 arginine (R) or lysine (K) residues on the C-terminus. FITC labeled MOGR$_2$ was synthesized with a FITC tag on the N-terminus. HBS-N running buffer (0.01 M HEPES, 0.15 M NaCl, pH 7.4,

filtered, degassed), 10 mM sodium acetate pH 5, amine couple kits (1-ethyl-3- (3-dimethylaminopropyl) carbodiimide (EDC) and N-hydroxysuccinimide (NHS)), 1 M ethanolamine, and Series S CM4 sensor chips were provided by Cytiva. β-mercaptoethanol, ethylenediaminetetraacetic acid (EDTA), 5x tris-borate-EDTA (TBE) buffer, and bovine serum albumin (BSA) were purchased from Sigma Aldrich (St. Louis, MO). Molecular biology grade water, fetal bovine serum (FBS), 20X PBS, 20% sodium dodecyl sulfate (SDS), HEPES, and non-essential amino acids were purchased from VWR (Radnor, PA). RPMI-1640 media, SYBR Gold gel stain, l-glutamine, penicillin-streptomycin, neutravidin protein, Ultrapure Agarose, DAPI viability stain, cell proliferation dye CFSE, RT-qPCR grade water, SuperScript IV VILO Master Mix, TaqMan Gene Expression Master Mix, Taqman probes glyceraldehyde 3-phosphate dehydrogenase (Gapdh); actin beta (Actb), Mm00607939_s1; 18s rRNA (18s), Mm03928990_g1; interleukin 6 (Il6), Mm00441891_m1; tumor necrosis factor (Tnf), Mm00443258_m1; myeloid differentiation primary response 88 (Myd88), Mm00440338_m1; were purchased from Thermo Fisher Scientific (Grand Island, NY). Spleen Dissociation Medium and CD4 negative selection kits were from STEMCELL Technologies (Vancouver, BC). CD11c MicroBeads were purchased from Miltenyi Biotec (Cambridge, MA). HEK-Blue™ TLR9 report cells, detection media, and antibiotics were supplied by Invivogen (San Diego, CA). Fluorescent antibody conjugates and enzyme-linked immunosorbent assay (ELISA) reagents were purchased from BD (San Jose, CA). Heat-inactivated TB (hiTB, nonviable desiccated Mycobacterium tuberculosis H37 Ra) and Incomplete Freud's Adjuvant was purchased from BD Difco. Quick-RNA microprep Kit and RNA lysis buffer was provided by Zymo Research (Irvine, CA). MicroAmp Optical 384-well reaction plates and optical adhesive film were purchased from Applied Biosystems (Waltham, MA). Pertussis toxin was purchased from List Biological Laboratories (Campbell, CA).

3.2.2) Cells and animals

Female C57BL/6J mice (9 weeks old, stock #000664) purchased from Jackson Laboratories (Bar Harbor, ME) were used for the in vivo EAE study. All primary cells were harvested from female C57BL/6J mice (6–12 weeks old, stock #000664) and female C57BL/6-Tg(Tcra2D2,Tcrb2D2)1Kuch/J (2D2) mice (10–16 weeks old, stock #006912) purchased from Jackson Laboratories (Bar Harbor, ME). 2D2 mice have transgenic $CD4^+$ T cell receptors specific for MOG. All animal care and experiments were carried out in compliance with federal, state, and local guidelines, and using protocols reviewed and approved by the University of Maryland's Institutional Animal Care and Use Committee (IACUC).

3.2.3) Complex formulation

Complexes were formed by mixing aqueous solutions of GpG with $MOGR_x$ (x = 2, 3, or 9) and $MOGK_x$ (x = 2, 3, or 9) in molecular biology grade water. The components were mixed at defined MOG:GpG charge ratios ranging from 1:20 to 20:1. In characterization and in vitro studies, the total concentration of GpG was fixed at 0.1 mg/mL while the concentration of MOG peptides was varied to control the charge ratio.

3.2.4) In vivo EAE efficacy study

EAE induction was accomplished using an injection of $MOG_{35–55}$ and adjuvant, as previously reported.[143] Briefly, an ampule of heat-inactivated TB (hiTB) was ground with a mortar and pestle to improve mixing. Complete Freund's Adjuvant (CFA) was made by suspending hiTB in Incomplete Freund's at 4 mg/mL and then mixed with a 2 mg/mL solution of peptide $MOG_{35–}$

$_{55}$ in sterile PBS. These solutions were mixed thoroughly at a 50:50 ratio (v/v) to make a solution of 2 mg hiTB and 1 mg $MOG_{35–55}$ per mL of suspension. This suspension was emulsified using a probe sonicator (Qsonica, CL-18 and 1/8 inch probe) while in a chilled ice bath. Mice were anesthetized under isoflurane and injected with 50 µL of suspension at two sites in the dorsal subcutaneous space for a total of 100 µL per injection. Mice were then injected i.p. with 60 ng of pertussis toxin in PBS at 2 and 24 hrs after the emulsion injection. Mice were monitored daily for weight and paralysis to assess health. Mice were weight matched prior to the first treatment. Treatments were administered on days 5, 10, and 15 after induction of EAE. Treatments were administered through two 50 µL injections in the dorsal subcutaneous space, near the tail base and avoiding the injection site of the emulsion. On the day of treatment, complexes composed of $MOGK_3$ and GpG (indicated as MOG/GpG) or $SIINFEKLR_9$ and GpG (indicated as SIINFEKL/GpG) were formulated by mixing peptide and GpG at a 1:1 charge ratio in molecular biology grade water. Enough MOG/GpG complexes were made to treat each mouse with a total complex dose of 285 µg (174 µg $MOGK_3$, 111 µg GpG). Mice treated with SIINFEKL/GpG complexes were dose matched to mice treated with MOG/GpG complexes so that all mice received equivalent doses of GpG per treatment. Sham treated mice received two 50 µL injections of PBS.

Mice were monitored daily for paralysis and graded using a clinical score rubric. Scores were assigned as follows: 0 = paralysis free, 0.5 = partial tail paralysis, 1 = full tail paralysis, 1.5 = decrease in hind limb stability, 2 = hind limb weakness and altered gait, 2.5 = partial hind limb paralysis, 3 = hind limb paralysis, 3.5 = hind limb paralysis and trunk weakness, 4 = hind limb paralysis and partial front limb paralysis, 4.5 = hind and front limb paralysis, and 5 = moribund. Humane end points were set for a score of 4 for 2 days in a row or anytime a score was >4.5 or when the weight of a mouse dropped to 70% of its initial weight. Water and food were localized

at the cage floor level to accommodate the levels of paralysis during the disease course. No mice were euthanized during the course of the study.

3.2.5) Surface plasmon resonance

Experiments were performed on the Biacore T200 instrument. GpG was immobilized to a Series S CM4 sensor chip and the different MOG peptides were flowed over the chip to analyze binding affinity between MOG and GpG. Flow rates during the experiment were 30 ul/min unless indicated otherwise and detection temperature was 25°C. To start, the CM4 chip was activated with an 8 minute injection of a mixed solution of 0.4 M EDC and 0.1 M NHS. Neutravidin was diluted in 10 mM sodium acetate pH 5 to a final concentration of 50 ug/mL and injected for 10 minutes to couple neutravidin to the sensor chip. The surface was then blocked with a 7 minute injection of 1 M ethanolamine pH 8.5 to remove any remaining reactive species on the surface. After couple neutravidin to the surface, biotinylated GpG was immobilized on the surface by diluting GpG in HBS-N running buffer to 1 ug/mL and injecting for 20-60 seconds. To measure kinetic curves of $MOGK_2$ and $MOGR_2$, peptides were diluted in HBS-N running buffer to concentrations of 4800, 2400, 1200, and 600 nM and flown over the sensor chip with a total contact time of 2 minutes. To measure kinetic curves of $MOGK_3$ and $MOGR_3$, peptides were diluted in HBS-N running buffer to concentrations of 3600, 1800, 900, and 450 nM and flowed over the sensor chip with a total contact time of 2 minutes. HBS-N buffer with no peptide (0 nM) was used as a baseline for each run. In between each kinetic curve, the surface of the chip was regenerated with two 15 second injections of 50 mM NaOH. For each MOG peptide, the five concentrations (including 0 nM) were fitted to a two-state binding model and K_D was calculated based on the association and dissociation rates between MOG peptides and GpG.

3.2.6) Agarose gels

Complexes were created at different charge ratios as mentioned above. 2% agarose gel were created with UltraPure Agarose in TBE buffer and stained with SYBR Gold nucleic acid gel stain. To run studies, 10 μL of samples were loaded into the gels and run for 5 minutes at 120V. For studies in Figure 2c and Figure 2d, complexes were created as indicated and then diluted in 1% and 0.01% SDS, respectively, before loading into the gels. Images were taken on the ProteinSimple FluorChem E System Gel Imager.

3.2.7) Characterization of complex size and surface charge

Hydrodynamic diameter and zeta potential of complexes were measured in triplicate using samples prepared in molecular biology grade water as described above and subsequently analyzed on a NanoBrook Omni_Particle Sizer and Zeta Potential Analyzer. Size was measured by dynamic light scattering and zeta potential was measured by phase analysis light scattering.

3.2.8) Toll-like receptor 9 reporter cell assay

HEK-Blue™ mTLR9 cells are co-transfected with the murine TLR9 gene and an inducible secreted embryonic alkaline phosphatase (SEAP) reporter gene. Stimulation of the cells with an unmethylated CpG-ODN sequence (TLR-9 agonist) activates NF-κB and AP-1, which leads to the production of SEAP to allow colorimetric detection. Cells were grown and plated in HEK-Blue detection media according to manufacturer instructions. After plating, mTLR9 cells were treated with media (negative controls), 0.5 μg/mL CpG (positive control), or 0.5 μg/mL CpG and either 1 μg/mL GpG, MOG/GpG complexes to a final concentration of 1 μg/mL GpG, or soluble MOG peptides dose matched to the amount of peptide in samples treated with complexes. After a 16 hr

incubation period, the level of SEAP was measured by spectrophotometry at 650 nm using a Tecan Spark Multimode Microplate Reader.

3.2.9) Dendritic cell activation assay

$CD11c^+$ DCs were isolated from the spleens of female C57BL/6J mice through positive selection with Spleen Dissociation Medium and CD11c MicroBeads according to the manufacturer protocol. DCs were plated in a 96 well plate at 100,000 cells per well and cultured in RPMI 1640 media supplemented with 10% FBS, 2 mM l-glutamine, 1X non-essential amino acids, 10 mM HEPES buffer, 1X penicillin and streptomycin, and 55 μM β-mercaptoethanol at 37 °C and 5% CO_2. DCs were left untreated (negative control), stimulated with 0.5 μg/mL CpG (positive control), or stimulated with 0.5 μg/mL CpG and then treated with either 1 μg/mL GpG, MOG/GpG complexes to a final concentration of 1 μg/mL GpG, or soluble MOG peptides dose matched to the amount of peptide in samples treated with complexes. To measure DC activation, cells were stained after 20 hrs for viability (DAPI) and for classic surface activation markers CD86, CD80, and CD40 using fluorescent antibody conjugates. Expression of surface markers was measured by flow cytometry using a BD FACS Celesta on the BD FACSDivaTM software and data were analyzed with FlowJo v.10.7 (TreeStar, Ashland, OR).

3.2.10) Dendritic cell RT-qPCR

CD11c+ DCs were isolated, plated, and treated for 6 hrs as described above. After the 6 hour incubation, RNA was isolated using a Quick-RNA Microprep Kit according to manufacturer's protocol. Cells were lysed in their wells using RNA lysis buffer, genomic material was captured in a column, and DNA was degraded with DNase I. Concentration and purity of

RNA were assessed on a Nanodrop 2000c (Thermo Fisher), and RNA was diluted to 20 ng/µL in RT-qPCR grade water. cDNA was reverse transcribed using a SuperScript IV VILO Master Mix. The qPCR reaction mix was made using TaqMan Gene Expression Assay probes in TaqMan Gene Expression Master Mix. The Taqman probes we used were Gapdh, Actb, 18s, Myd88, Tnf, and Il6. qPCR was performed in a MicroAmp Optical 384-well reaction plate with optical adhesive film on a QuantStudio 7 Flex Real-Time PCR System (Applied Biosystems). Sample normalization was done using an average of three housekeeping genes: Gapdh, Actb, 18s. Analysis and hierarchal clustering were done in MatLab using the clustergram function. The data were standardized for each gene to compare across multiple groups. Clustering was performed using a single linkage (nearest neighbor).

3.2.11) Dendritic cell/T cell co-cultures

DCs were isolated, plated, and treated for 24 hrs as described above. After 24 hrs, $CD4^+$ T cells were isolated from the spleens of 2D2 mice via a CD4 negative selection kit and stained with CFSE to assess proliferation. 300,000 T cells were added to the wells containing the DCs and incubated for 72 hrs at 37 °C and 5% CO_2. After 72 hrs, cells were stained for markers CD4, CD25, and FoxP3 to assess polarization towards T_{REG}. Cells were also stained with DAPI to assess viability. Expression of markers was measured by flow cytometry using a BD FACS Celesta on the BD FACSDivaTM software and data were analyzed with FlowJo v.10.7 (TreeStar, Ashland, OR).

3.2.12) Enzyme-linked immunosorbent assay

Supernatants from DC/T cell co-cultures were collected. Cytokine secretion levels were analyzed via ELISA using mouse interferon gamma (IFN-γ) and interleukin-6 (IL-6) reagents. Briefly, 96-well plates were coated with either IFN-γ or IL-6 capture antibody and after an overnight incubation, the supernatant samples were added. An IFN-γ or IL-6 detection antibody and streptavidin-horseradish peroxidase conjugate mixture was then added to the wells for 1 hr. A tetramethylbenzidine and hydrogen peroxide mixture was added to each well for 30 min and the reaction was stopped by the addition of 1 M phosphoric acid. Absorbance of each sample at 450 nm was measured with a Tecan Spark Multimode Microplate Reader. IFN-γ and IL-6 concentrations were calculated from absorbance by comparing to a standard curve.

3.2.13) Statistical analysis

All characterization studies were replicated at least three times and all data points, along with mean ± standard deviation, were reported. Cellular analyses were replicated at least twice to ensure reproducibility of biological effects. For surface plasmon resonance, DC activation, and T cell studies, one-way ANOVA with Tukey post-test corrections for multiple comparisons was used to compare groups. For sizing and surface charge studies, two-way ANOVA with Tukey post-test corrections for multiple comparisons was used to compare the effect of MOG:GpG charge ratio and MOG peptide sequence. Only differences for the 1:1 ratio were reported. For the EAE study, a non-parametric Steel-Dwass test was used to compare clinical scores of each treatment group at day 25 of the study ($p<0.05$). For the RT-qPCR studies, a Tukey-Kramer test for multiple comparisons with an adjusted $p<0.05$ was used to compare all groups. Statistical calculations were performed using JMP Pro (v14, SAS institute).

3.3) Results and Discussion

3.3.1) Complexes induced antigen-specific tolerance in a pre-clinical model of multiple sclerosis

A critical limitation of existing autoimmune therapies is the inability to generate antigen-specific tolerance, creating immunosuppression and immunotoxicty for patients. Thus, we first tested if complexes generate antigen-specific tolerance in a pre-clinical model of multiple sclerosis, experimental autoimmune encephalomyelitis (EAE). In these studies mice were treated with complexes 5, 10, and 15 days after EAE induction, representing an early therapuetic intervention. Excitingly, we discovered MOG/GpG complexes generated significant therapuetic improvements in paralysis relative to both sham injections (PBS) and complexes composed of GpG and a disease-irrelevant antigen (SIINFEKL) (**Fig. 12A-B**). Likewise, MOG/GpG complexes reduced weight loss and promoted return to healthy baseline weights (**Fig. 12C**). These results demonstrate the importance of antigen sequence, motivating our studies to understand how the electrostatic interactions between MOG and GpG impacted binding affinity, the subsequent

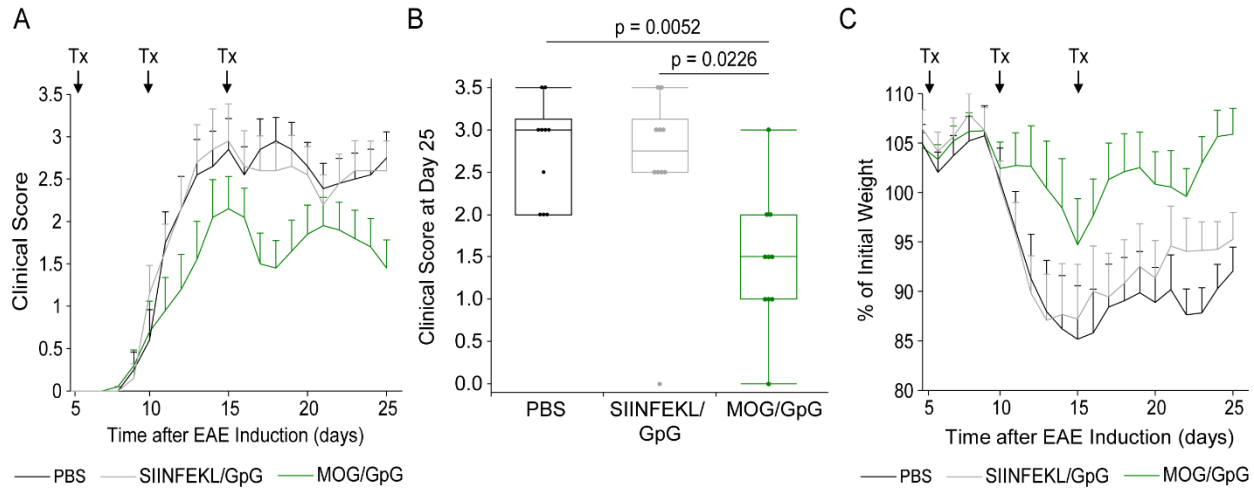

Figure 12. A) Disease progression assessed by daily measurements of clinical scores. 0 = paralysis free, 1 = tail paralysis, 2 = hind-limb weakness, 3 = hind-limb paralysis, 4 = partial front-limb paralysis. B) Distribution of clinical scores within each treatment group at the conclusion of the study (day 25). Statistical significance ($p<0.05$) is indicated for Steel-Dwass tests for all pairs at day 25. C) Disease progression assessed by daily measurements of body weight and reported as a percentage of the initial weight at the start of the study. n=10 for all treatment groups.

interactions and processing by APCs, and ultimately the role these changing biophysical aspects played in polarizing myelin-specific T cells.

3.3.2) Binding affinity between immune signals could be tuned as a function of total charge and type of anchored amino acid residue

We first designed a library of MOG peptide sequences anchored with distinct types and numbers of cationic amino acid residues (**Fig. 13A**). In particular, the native MOG sequence was appended with 2, 3, or 9 residues of either lysine (K) or arginine (R). Complexes were then spontaneously formed by mixing each cationic MOG peptide with the anionic oligonucleotide, GpG, at defined charge ratios (**Fig. 13B**).

A

Signal	Sequence	Total Charge
$MOGR_2$	MEVGWYRSPFSRVVLHLYRNGKRR	+5
$MOGR_3$	MEVGWYRSPFSRVVLHLYRNGKRRR	+6
$MOGR_9$	MEVGWYRSPFSRVVLHLYRNGKRRRRRRRRR	+12
$MOGK_2$	MEVGWYRSPFSRVVLHLYRNGKKK	+5
$MOGK_3$	MEVGWYRSPFSRVVLHLYRNGKKKK	+6
$MOGK_9$	MEVGWYRSPFSRVVLHLYRNGKKKKKKKKK	+12
GpG	TGACTGTGAAGGTTAGAGATGA	-22

B

Figure 13. A) Sequence and total charge of all MOG peptides and GpG used to form complexes. Red amino acids indicate additional amino acids anchored to MOG. B) MOG and GpG are mixed in aqueous solution to form MOG/GpG complexes.

We next used surface plasmon resonance to measure the binding affinity with which MOG peptides assembled with GpG (**Fig. 14A**). Using a range of concentrations, peptides were flowed over a sensor chip coated with GpG to measure the association and dissociation rates. The kinetic

binding curves were then fitted to a two-state binding model and the dissociation rate constants (K_D) were calculated for binding between GpG and $MOGK_2$, $MOGK_3$, $MOGR_2$, and $MOGR_3$ (**Fig. 14B-F**). A two-state binding model was chosen based on the expectation that the peptide-oligo complex is formed after an initial binding event, followed by a subsequent solvent exclusion-like step to readjust to an entropically favorable conformation.[144]

When anchoring MOG with either arginine or lysine, K_D values decreased as the number of anchored residues was increased from 2 to 3 (**Fig. 14B**). This observation indicated that the binding affinity between MOG and GpG increased when MOG exhibited a more positive charge. Interestingly, when comparing $MOGK_2$ to $MOGR_2$ and $MOGK_3$ to $MOGR_3$, K_D values were lower

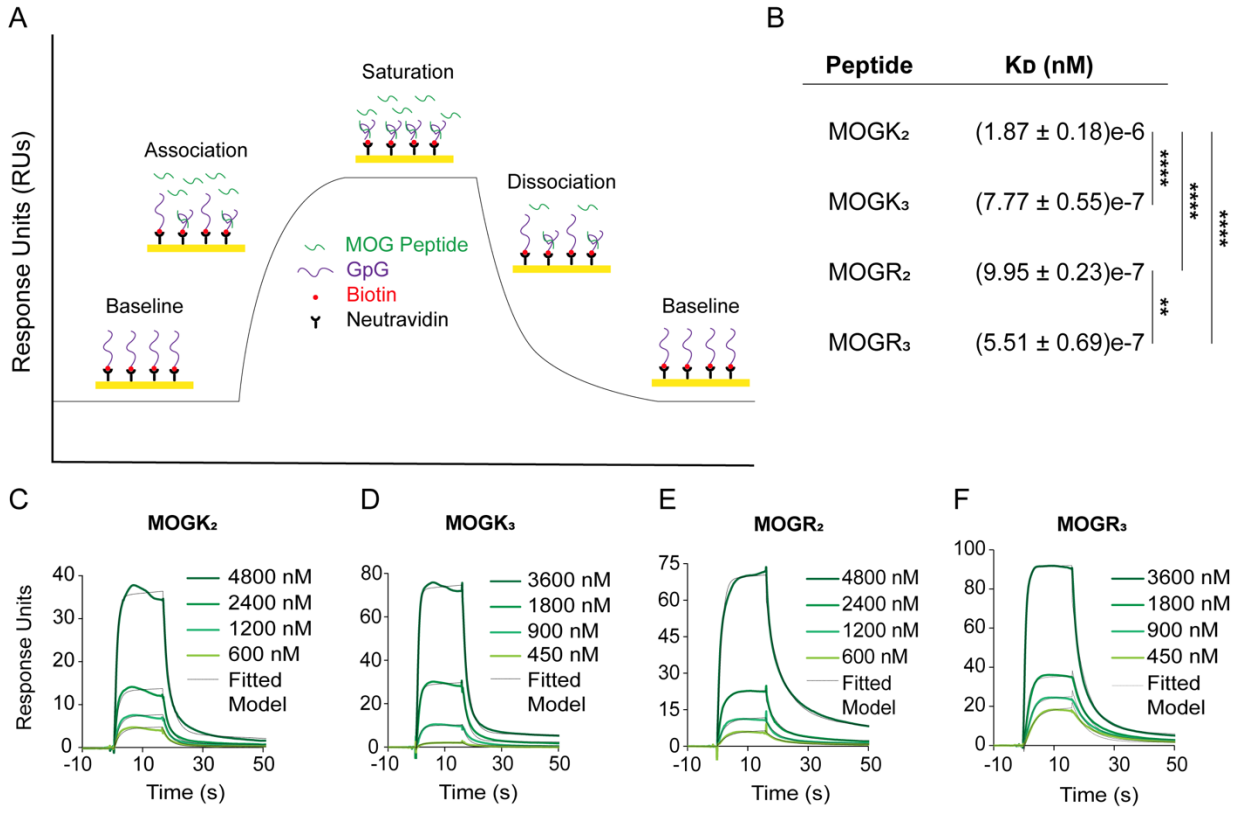

Figure 14. A) Graphic representation describing the kinetic curves generated by surface plasmon resonance as MOG associates and dissociates from GpG. B) Average K_D values (n = 3) calculated for binding between MOG peptides and GpG. Representative kinetic curves from one experiment are shown for C) $MOGK_2$, D) $MOGK_3$, E) $MOGR_2$, and F) $MOGR_3$. Statistics were analyzed by One-way ANOVA with Tukey post-test to correct for multiple comparisons. **p<0.01, ****p<0.0001

when MOG was anchored with arginine residues rather than lysine residues. Since the peptides for a given number of residues exhibited the same overall charge, this finding suggested additional factors may have impacted the molecular interactions between MOG peptides and GpG. One potential explanation is hydrogen bonding with the side chain of the amino acids. For example, a recent molecular dynamics simulation study revealed arginine attracted more phosphate groups and water molecules relative to lysine through greater hydrogen bond formation.[140] This possibility is supported by computational modeling studies described in Chapter 4. Alternatively, differences in the side chain acidity of arginine and lysine could have altered the charge states of the peptides and resulted in differential electrostatic interactions when adsorbed to GpG. Laboratory studies have also revealed that replacing lysine with arginine improved stability of proteins in the presence of chemical denaturants.[145] Thus, differences in amino acid side chain structure might have also impacted the self-assembly between MOG peptides and GpG. To further test this, we attempted lengthier anchoring sequences in these binding studies (i.e., $MOGK_9$, $MOGR_9$). Unfortunately, we could not achieve sufficient signal resolution with these high charge designs to distinguish between binding of peptides to GpG in the probe channel and high background level of peptide binding measured on the uncoated reference channel of the sensor chip.

3.3.3) Assembly ratio and peptide sequence impacted signal loading and complex stability.

After establishing a link between MOG peptide design and binding affinity with GpG, we studied how peptide sequence impacted assembly of MOG and GpG into complexes. Since complexes were formed due to electrostatic interactions, we first determined the effect of charge balance on complex formation. This was accomplished by fixing the concentration of GpG (anionic) constant and varying the input concentration of MOG peptides (cationic) across a range of positive to negative charge ratios - the MOG:GpG charge ratio. We then performed gel

electrophoresis to assess the amount of GpG in complexes, relative to the amount unbound in solution, as a function of MOG:GpG charge ratio. Beginning with $MOGR_2$, analysis of a broad range of charge ratios (1:20 – 20:1) revealed GpG was complexed at charge ratios ≥1:1 (**Fig. 15A**); this was indicated by the absence of migrating bands compared to the free GpG migrating in the control lane. Subsequently, we created complexes with the entire library of MOG peptide sequences and assessed complex formation over MOG:GpG ratios of 1:5 – 5:1. Full complexation of GpG was associated with the ratio at which the charge balance was neutral (i.e., 1:1) and at positive MOG:GpG charge ratios (i.e., >1:1) (**Fig. 15B**). This suggested that loading of signals into complexes was determined by the aggregate charge ratio during formulation. These results were consistent with all MOG peptide sequences, indicating that irrespective of the charge of an individual peptide design, the assembly charge ratio drove loading of GpG into complexes.

We next directly assessed the proportion of MOG and GpG in the complexes and remaining unbound in solution. To do this, we created complexes with FITC-labeled $MOGR_2$ and GpG, used centrifugation to isolate the complexes from the supernatants, and then added a surfactant, 1% sodium dodecyl sulfate (SDS), to each fraction. Diluting the samples in SDS dissociated MOG and GpG in the pellets and coated the peptides with a negative surface charge; this allowed both uncomplexed MOG peptides and GpG to migrate through the gel. Using FITC-labeled $MOGR_2$ allowed us to detect migrating peptide within the gel (unlabeled $MOGR_2$ could not be visualized). At the 1:1 charge ratio, MOG and GpG were observed in pellets, but not supernatants, indicating both MOG and GpG were loaded into complexes (**Fig. 15C**). At ratios <1:1, minimal levels of GpG were observed in the pellets, indicating negative charge ratios were insufficient to fully load GpG. At ratios >1:1, MOG and GpG were each observed in the pellets, but an increasing amount

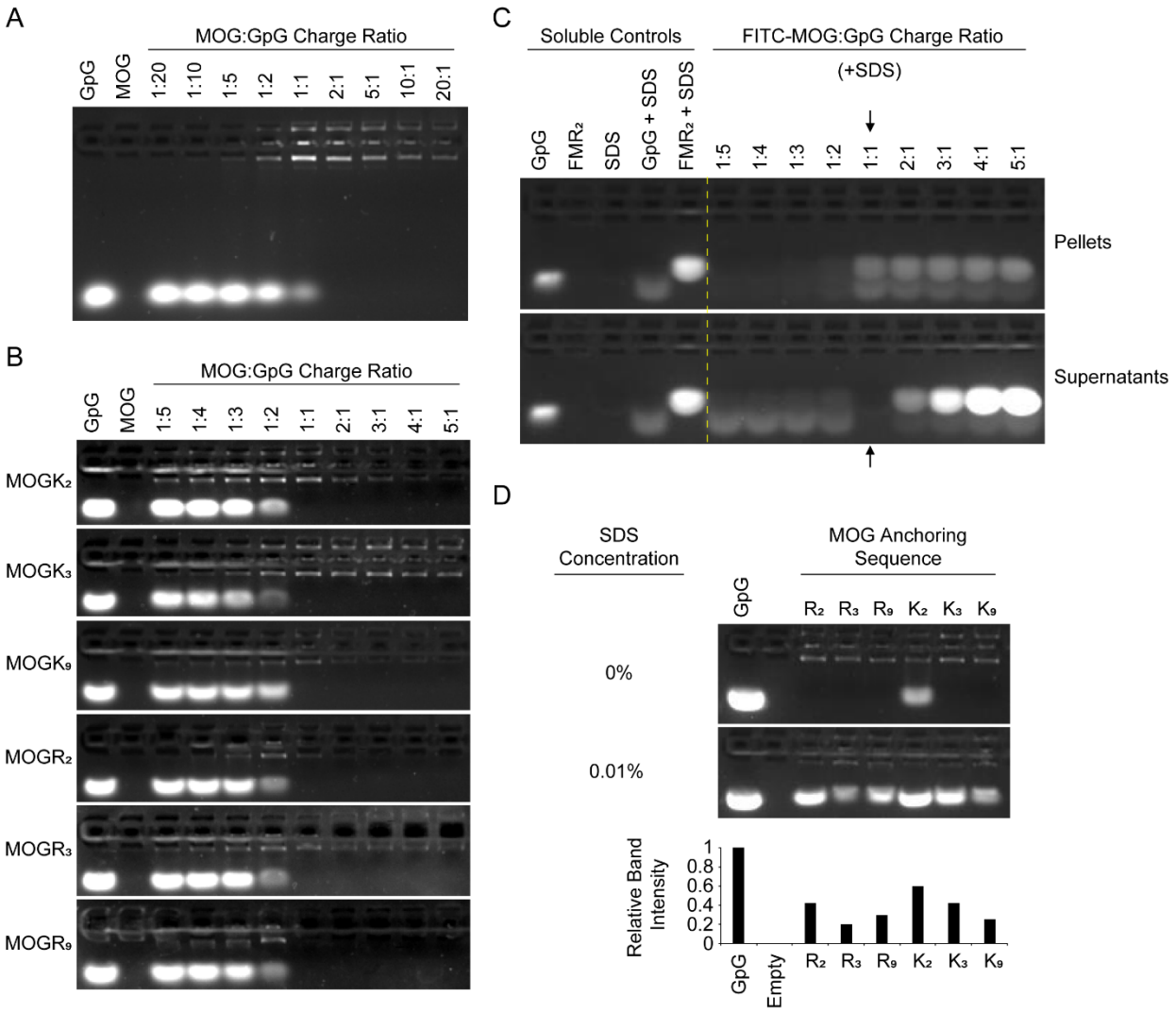

Figure 15. A) Agarose gel of $MOGR_2$/GpG complexes over a wide range of charge ratios. B) Agarose gel of MOG/GpG complexes with the entire library of MOG peptide sequences over a narrow range of 1:5 – 5:1. C) Agarose gel of complex pellets and supernatants after dilution with 1% SDS. Complexes were formed with FITC-$MOGR_2$ (FMR_2) and GpG. D) Agarose gel of complexes create at a 2:1 charge ratio and then diluted in 0.01% SDS after formulation.

of MOG was also detected in the supernatants as the MOG:GpG charge ratio increased. This indicated an excess of uncompensated positive charge at higher ratios that resulted in uncomplexed MOG. These different assembly features were notable since high levels of self-antigen in isolation (i.e., without regulatory signals) might exacerbate autoimmune disease. Similarly, high doses of regulatory signals alone (i.e., without self-antigen) might drive broad, non-specific suppression. Delivery of signals in particulate form is also a desired characteristic, as this state typically

improves uptake and potency of the signals compared to soluble forms (see Chapter 1).[34-36,146] Particulate delivery also provides more precise control over the mechanism through which the signals are taken up, which is important for targeting spatially restricted receptors involved in inflammation, such as toll-like receptors.

Our findings above indicated that MOG peptide sequence impacted the interactions between MOG and GpG, but not loading of GpG into complexes. Since the strength of interaction between MOG and GpG changed as a function of peptide sequence in **Fig. 14**, we tested if the peptide sequence used to form complexes was correlated with better colloidal stability. To investigate this question, we created complexes at a 2:1 MOG:GpG charge ratio with each MOG peptide sequence, exposed complexes to SDS, then used gel electrophoresis to determine if complexes remained bound. We chose this ratio since the complexes exhibited the most uniform properties across the different peptide designs. In these studies, a lower concentration of SDS (0.01%) was used to allow measurement of relative interaction as a function of peptide sequence. We discovered complexes synthesized with $MOGK_2$ and $MOGR_2$ resulted in greater amounts of migrating GpG relative to lanes with complexes assembled using $MOGR_3$, $MOGR_9$, $MOGK_3$, and $MOGK_9$ (**Fig. 15D**). These results correlated with the results from **Fig. 14**, which revealed $MOGK_2$ and $MOGR_2$ exhibited the lowest affinity for GpG. Together, the data suggested the binding affinity between self-assembled immune signals impacted stability of the complexes in the presence of environmental stresses, such as the presence of surfactants.

3.3.4) Peptide sequence and charge density impacted complex size and surface charge

As reviewed in Chapter 1, biophysical parameters, such as particle diameter and surface charge, have dramatic impacts on uptake by immune cells and the subsequent intracellular signal processing. Thus, we characterized complex diameter and surface charge over a MOG:GpG charge

ratio range of 1:2 – 5:1 for each MOG peptide. The size of particles generally ranged from 120 – 200 nm in diameter across charge ratios and peptide designs (**Fig. 16A**, **Table 1**). This size range readily enables endocytic uptake,[147] a property desired for targeting toll-like receptor 9 receptors located in endosomes and lysosomes of innate immune cells. Other biophysical properties - such as distribution of toll-like receptor ligands along carriers with distinct surface curvature - have recently been shown to impact endosomal access to toll-like receptors.[148] In macrophages, an important APC, this report demonstrated a change in innate signaling resulting from changes in endosome structure. Thus, designing delivery systems with appropriate biophysical properties provides a new dimension to influence upstream events and control downstream immune outcomes.

The surface charge of complexes changed as a function of the charge ratio. Complexes were negatively charged at ratios <1:1, positively charged at ratios >1:1, and varied in surface charge at 1:1 (**Fig. 16B**). In all cases, a common result was an inversion of surface charge as the positive to negative charge balance shifted from <1:1 to >1:1. We were particularly interested in the physical properties of complexes at the 1:1 ratio, as this was the ratio where MOG and GpG were fully loaded in complexes (**Fig. 16C**). Interestingly, when focusing on complexes at the 1:1 ratio, complexes containing $MOGK_2$ were ~1 μm (**Fig. 16A**, **16C**), which was an order of magnitude larger than complexes containing other peptide sequences. From **Fig. 14**, this antigen design exhibited the lowest binding affinity for GpG, which might suggest a loose association that maintained a particulate form, but that did not tightly complex GpG. Further, depending on the antigen design, complexes at the 1:1 ratio exhibited a range of surface charges between positive, negative, and neutral (**Fig. 16D**). The $MOGK_2$ complexes were near-neutral in surface charge at this ratio. Previous studies by us and others have made similar observations where complexes with

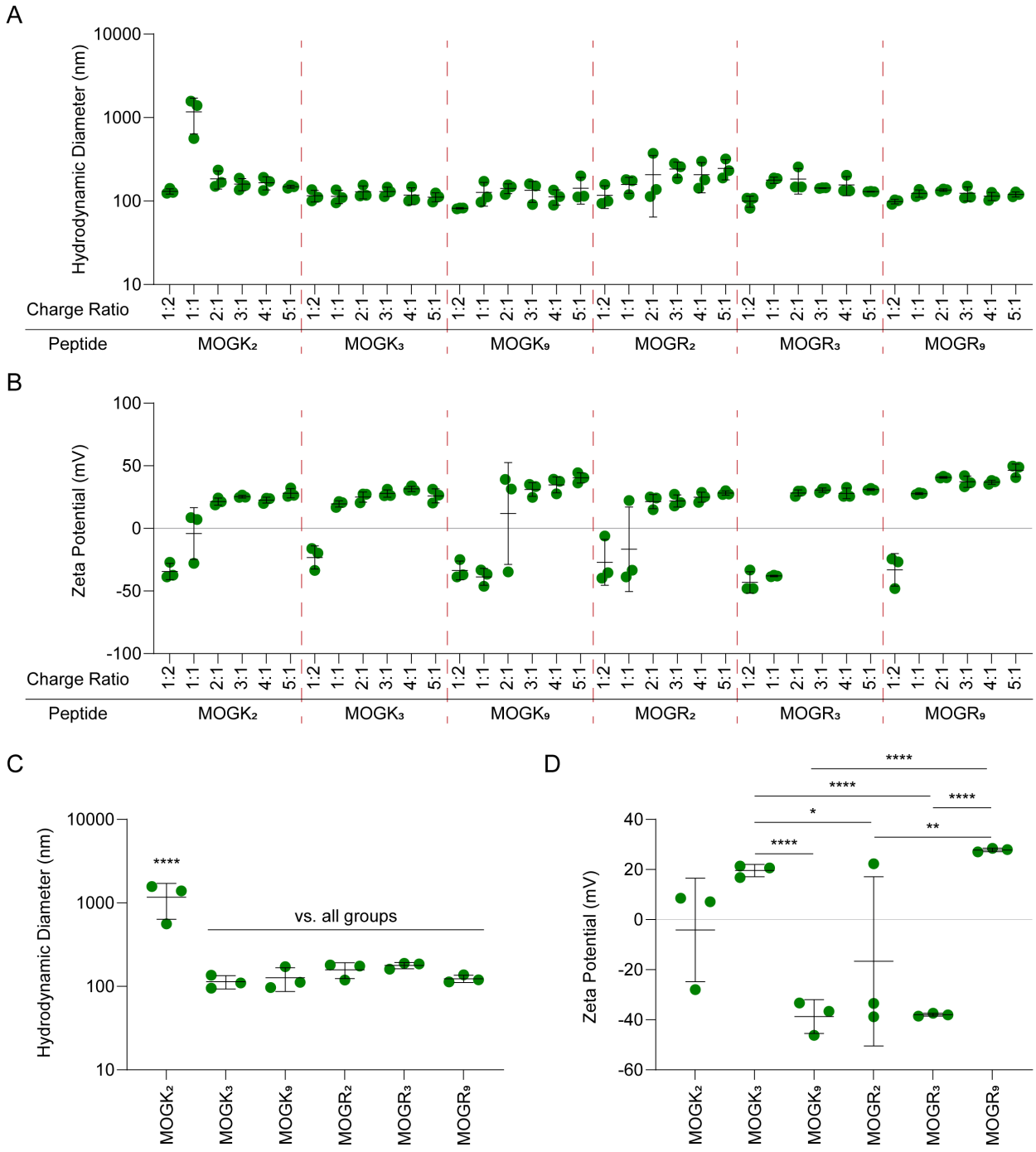

Figure 16. A) Hydrodynamic diameter and B) surface charge of complexes formed over a charge ratio range of 1:2 – 5:1 with different MOG peptides. C) Hydrodynamic diameter and D) surface charge of complexes formed at the 1:1 charge ratio with different MOG peptides. Statistics were analyzed by two-way ANOVA with Tukey post-test to correct for multiple comparisons (n=3). *p<0.05, **p<0.01, ****p<0.0001

near-neutral surface charge appeared larger than complexes with positive or negative surface

charge.[125,149,150] In certain situations, the neutral charge balance in solution may drive the formation of coacervates,[142] causing the complexes to appear larger when measured by dynamic light scattering. Additionally, because near-neutral ratios result in low levels of uncompensated charge, the driving force for tight electrostatic assembly of complexes is reduced. Futures studies using transmission electron microscopy or other techniques could help reveal the nature for these specific complexes. The variability in surface charge highlighted an area where better understanding of how to design peptides for self-assembly could improve control over biophysical properties of self-assembled immunotherapies and create uniformity across formulations.

Table 1: Average count rates and PDI (n=3) of MOG/GpG complexes.

	Charge Ratio	Count rate (kilo counts per second)	STD	PDI	STD
$MOGK_2$	1:2	509	46	0.238	0.017
	1:1	500	37	0.171	0.120
	2:1	529	35	0.253	0.021
	3:1	571	52	0.234	0.007
	4:1	518	59	0.173	0.095
	5:1	673	208	0.174	0.050
$MOGK_3$	1:2	558	55	0.200	0.002
	1:1	566	6	0.194	0.015
	2:1	564	72	0.203	0.028
	3:1	581	56	0.219	0.012
	4:1	561	89	0.239	0.010
	5:1	418	142	0.265	0.010
$MOGK_9$	1:2	505	59	0.232	0.027
	1:1	469	98	0.230	0.037
	2:1	510	50	0.219	0.015
	3:1	514	3	0.214	0.014
	4:1	506	30	0.217	0.026
	5:1	517	33	0.233	0.029
$MOGR_2$	1:2	463	57	0.259	0.004
	1:1	482	32	0.259	0.035
	2:1	513	36	0.252	0.038
	3:1	565	15	0.269	0.012
	4:1	560	81	0.273	0.030

	5:1	567	119	0.210	0.087
$MOGR_3$	1:2	525	13	0.243	0.028
	1:1	573	48	0.284	0.012
	2:1	565	30	0.281	0.027
	3:1	520	66	0.257	0.014
	4:1	534	41	0.262	0.026
	5:1	521	44	0.251	0.003
$MOGR_9$	1:2	537	16	0.252	0.028
	1:1	462	54	0.221	0.012
	2:1	492	17	0.243	0.012
	3:1	478	15	0.241	0.023
	4:1	506	7	0.239	0.013
	5:1	546	62	0.249	0.009

3.3.5) Complexes inhibited toll-like receptor 9 signaling and restrained inflammatory gene expression in dendritic cells

We next investigated whether changes in biophysical properties resulting from peptide design impacted innate immune signaling. We incubated complexes with TLR9 reporter cells that were activated with a molecular agonist of TLR9, CpG. This activation resulted in strong TLR9 signaling that was blunted by both soluble GpG and MOG/GpG complexes (**Fig. 17A-B**). GpG in complexes was equally effective in inhibiting TLR9 stimulation relative to soluble GpG, regardless of the MOG peptide sequence (**Fig. 17A**) or the charge ratio (**Fig. 17B**); this result indicated GpG retained full functionality even when delivered in complexes.

Figure 17. TLR9 activity in reporter cells as a function of A) MOG peptide sequence and B) charge ratio. C) Representative analysis scheme of dendritic cells analyzed by flow cytometry. D) CD86 and E) CD40 expression as a function of MOG peptide sequence. In panels D and E, comparisons between MOG/GpG complexes and soluble MOG within the same peptide sequence are indicated. Statistics were analyzed by One-way ANOVA with Tukey post-test to correct for multiple comparisons (n=3, ****$p<0.0001$). F) A heat map and log2 gene expression data for G) Myd88, H) Tnf, and I) Il6 is shown. In panels G-I, statistical significance indicates an adjusted $p<0.05$ compared to CpG (b) and CpG + GpG (c) following a Tukey-Kramer multiple comparisons test.

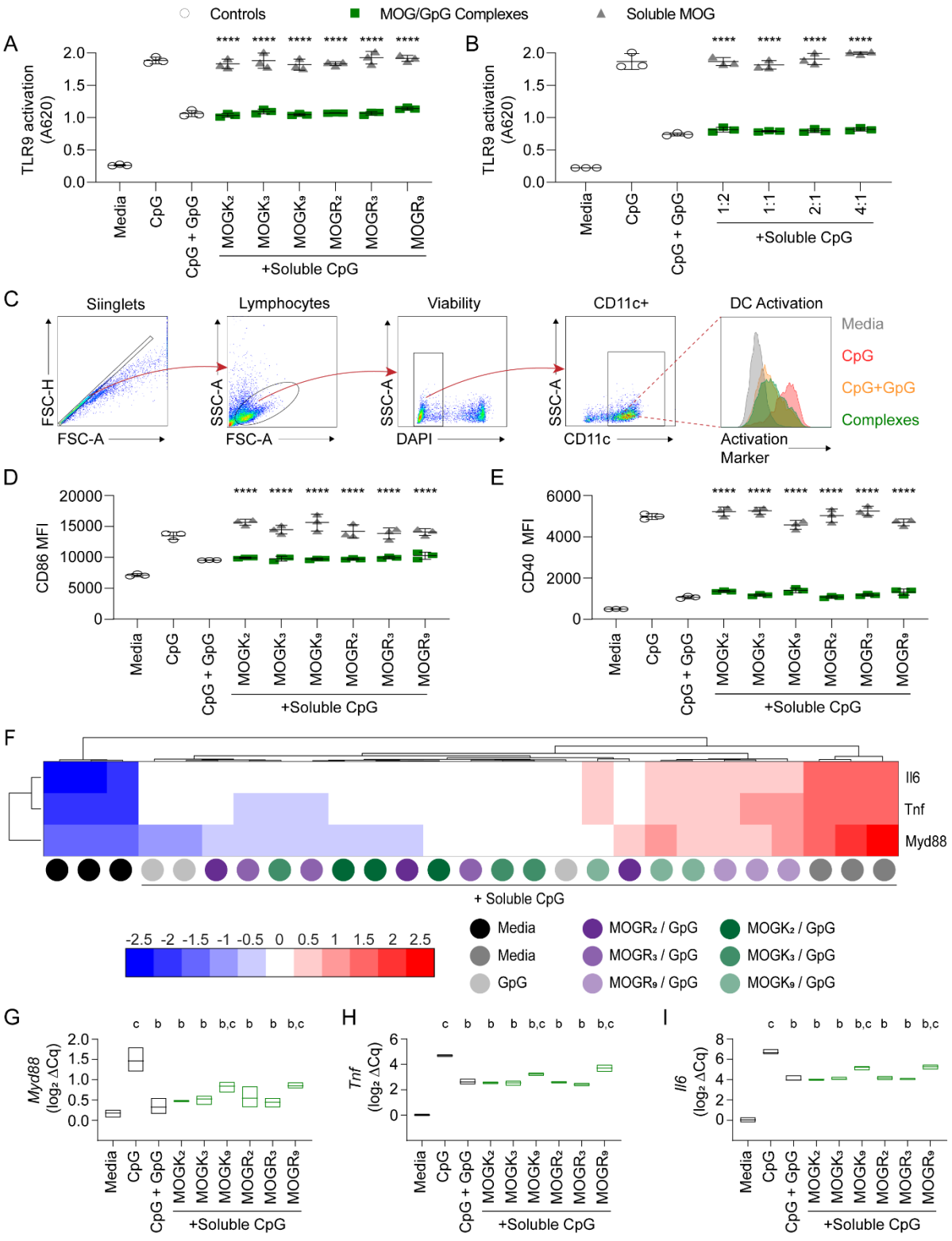
Controls
MOG/GpG Complexes
Soluble MOG
A
TLR9 activation (A620)
Media
CpG
CpG + GpG
MOGK₂
MOGK₃
MOGK₉
MOGR₂
MOGR₃
MOGR₉
+Soluble CpG
B
1:2
1:1
2:1
4:1
C
Siinglets
Lymphocytes
Viability
CD11c+
DC Activation
FSC-H
FSC-A
SSC-A
DAPI
CD11c
Activation Marker
Media
CpG
CpG+GpG
Complexes
D
CD86 MFI
E
CD40 MFI
F
Il6
Tnf
Myd88
+ Soluble CpG
-2.5 -2 -1.5 -1 -0.5 0 0.5 1 1.5 2 2.5
Media
Media
GpG
MOGR₂ / GpG
MOGR₃ / GpG
MOGR₉ / GpG
MOGK₂ / GpG
MOGK₃ / GpG
MOGK₉ / GpG
G
Myd88 (log₂ ΔCq)
H
Tnf (log₂ ΔCq)
I
Il6 (log₂ ΔCq)

During healthy immune processes, when toll-like receptors are activated, dendritic cells present antigens along with co-stimulatory signals to T cells. As reviewed in Chapter 1, when T cells bind antigen and co-stimulatory signals on the surface of dendritic cells, T cells differentiate into inflammatory phenotypes and mount immune responses against cells or tissue expressing the antigens they are specific for. Dendritic cells can also present antigen without co-stimulatory signals or with regulatory signals, as in the case of antigen originating from self-tissue during cellular turnover. T cells that bind antigen in the absence of co-stimulatory signals can be rendered inactive or adopt regulatory phenotypes. This is a key mechanism by which the body promotes immune tolerance and prevents inadvertent attack of self-antigens expressed on host tissue.

Thus, we next tested the ability of this library of complexes to inhibit TLR9 activation in primary dendritic cells isolated from mice. Dendritic cells were activated with CpG and cultured with complexes as described above. CpG activates dendritic cells and triggers upregulation of co-stimulatory markers, such as CD86, CD40, and CD80. Thus, after 20 hours, dendritic cells were analyzed by flow cytometry for expression of CD86, CD40, and CD80 to determine if GpG

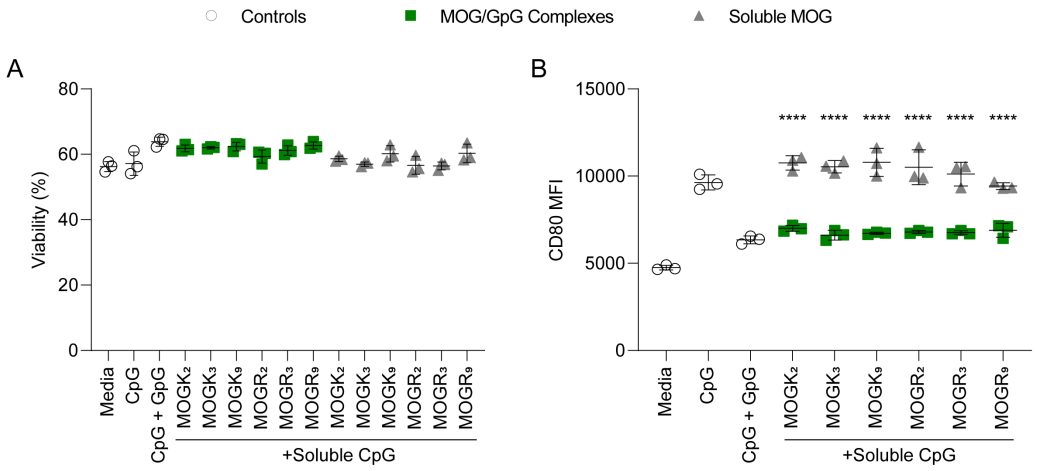

Figure 18. A) Viability of dendritic cells as a function of treatment. B) CD80 expression by dendritic cells as a function of treatment. Comparisons between MOG/GpG complexes and soluble MOG within the same peptide sequence are indicated. Statistics were analyzed by One-way ANOVA with Tukey post-test to correct for multiple comparisons (n=3). ****p<0.0001

effectively inhibited TLR9-induced activation (**Fig. 17C**). None of the complexes impacted cell viability (**Fig. 18A**). Dendritic cells cultured with CpG and MOG/GpG complexes exhibited reduced levels of CD86 (**Fig. 17D**), CD40 (**Fig. 17E**), and CD80 (**Fig. 18B**) that were similar to cells cultured with CpG and soluble GpG.

These results indicated that the modulatory component of this therapy, GpG, remained available to exert pathway-specific functions when delivered in complexes. To directly probe the fate and action of these complexes after uptake, we analyzed the gene expression of MyD88, a master regulator of the TLR9 signaling pathway, and inflammatory cytokines TNF and IL-6 six hours after treatment. As expected, stimulation with CpG significantly increased expression of *Myd88*, *Tnf*, and *Il6* in dendritic cells compared to untreated media controls (**Fig. 17F-I**). However, when dendritic cells were treated with MOG/GpG complexes or soluble GpG in addition to CpG, expression of *Myd88*, *Tnf*, and *Il6* was significantly reduced. These results indicated that complexes are taken up and processed at least in part via endosomal processes where GpG can inhibit TLR9 stimulation and prevent inflammatory signaling via MyD88. Interestingly, dendritic cells treated with $MOGK_9$/GpG and $MOGR_9$/GpG complexes expressed significantly more *Myd88*, *Tnf*, and *Il6* relative to cells treated with other complex formulations or soluble GpG (**Fig. 17G-I**). This result may indicate that GpG was not as readily available to inhibit TLR9 activation when complexed with $MOGK_9$ or $MOGR_9$ because of tighter binding due to the larger cationic charge per MOG peptide.

3.3.6) T cell proliferation and polarization were influenced by peptide design

We hypothesized that although complexation of GpG did not impact expression of co-stimulatory markers by DCs, the peptide design might lead to distinct antigen-specific T cell responses resulting from the altered binding affinity with GpG and biophysical properties driven

by peptide charge density. To investigate this possibility, primary dendritic cells were cultured with CpG and MOG/GpG complexes as above for 24 hours, then co-cultured with MOG-specific T cells isolated from 2D2 transgenic mice (**Fig. 19A**). These cells exhibit T cell receptors specific for MOG antigen. When the T cells encounter MOG presented by dendritic cells with the appropriate molecular machinery and co-stimulatory signals, they proliferate and secrete inflammatory signals, mimicking some aspects of MOG-driven autoimmune inflammation during multiple sclerosis. Thus, after 72 hours, we analyzed the T cells by flow cytometry for proliferation and to determine the extent to which each complex design could polarize these cells towards T_{REG} phenotypes (**Fig. 19B-D**) and away from inflammatory functions. The latter was assessed by measuring secretion of key inflammatory cytokines by ELISA (**Fig. 19E-F**).

In all cases, complexes drove significant levels of MOG-specific proliferation (**Fig. 19C**). Interestingly, proliferation was impacted by the number of lysine and arginine residues in the peptide design. Of note, ~65% of T cells proliferated in response to $MOGK_2$, which was significantly lower than proliferation of T cells in response to all other MOG peptides. In all cases, the level of proliferation in cells treated with MOG/GpG complexes was similar to that of cells treated with soluble MOG peptides without GpG. These results indicated that peptide sequence, and not delivery of GpG, impacted T cell proliferation. Intriguingly, however, when we assessed the function of the proliferating MOG-specific T cells, significant differences existed between cells treated with MOG/GpG complexes vs. soluble MOG peptides without GpG, and as a function

Figure 19. A) Representative analysis scheme of T cells analyzed by flow cytometry. B) Proliferation, C) regulatory phenotype, and presence of inflammatory cytokines D) IFNγ and E) IL-6 as a function of MOG peptide sequence. In panel C, green asterisks indicate comparisons between MOG/GpG complexes, black asterisks indicate comparisons between soluble MOG peptides. In panels D, E, and F, comparisons between MOG/GpG complexes and soluble MOG within the same peptide sequence are indicated. Statistics were analyzed by One-way ANOVA with Tukey post-test to correct for multiple comparisons (n=3). *p<0.05, **p<0.01, ***p<0.001, ****p<0.0001

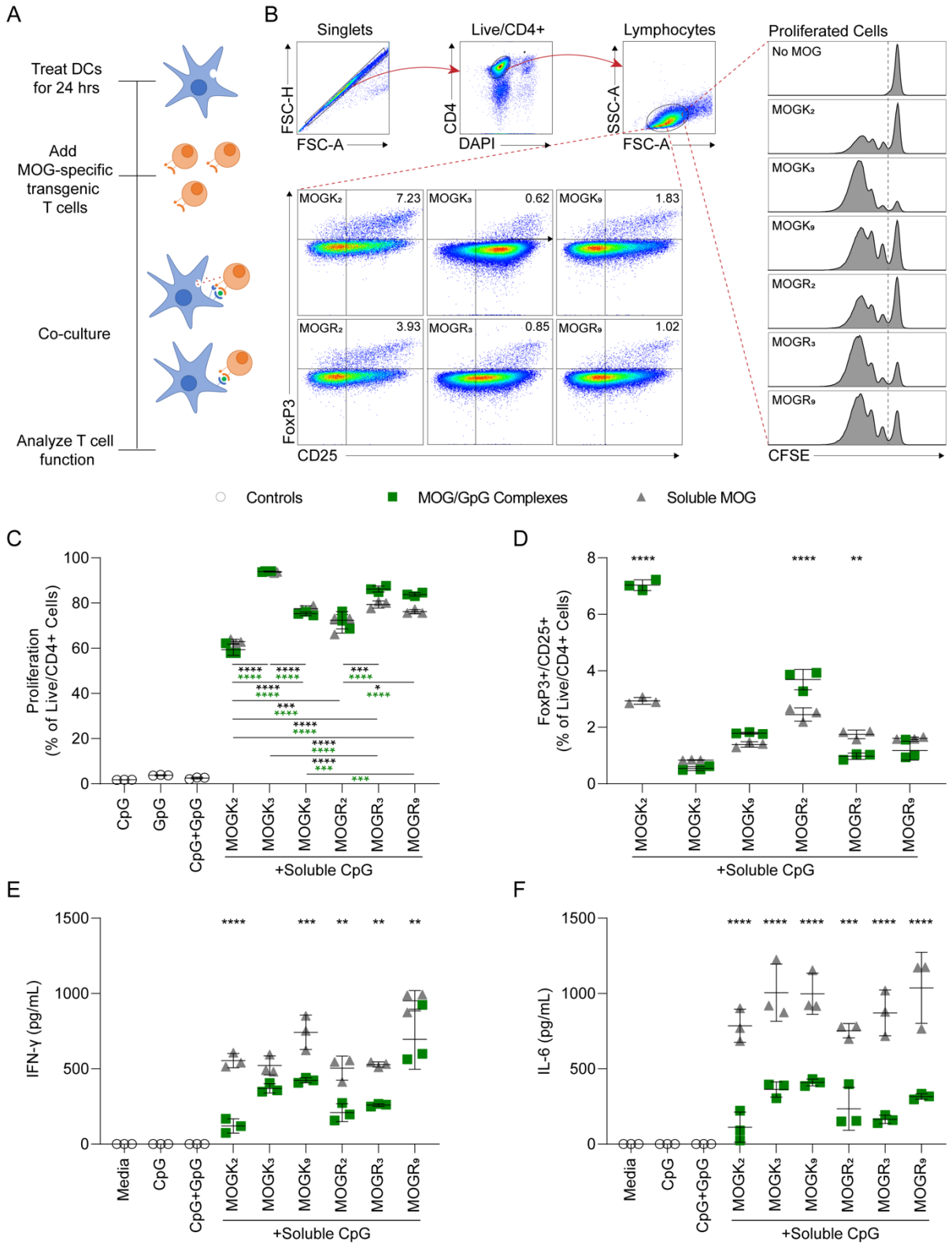

of MOG peptide design. T cells treated with $MOGK_2$ and $MOGR_2$ complexes were strongly polarized towards regulatory phenotypes relative to soluble $MOGK_2$ and $MOGR_2$, respectively

(**Fig. 19D**). These results indicated that presence of GpG was necessary for polarization of T cells towards regulatory phenotypes. Intriguingly, the size of the effect was dependent on MOG peptide design. Polarization towards T_{REG} was inversely correlated with the dissociation constant (K_D) between MOG and GpG (**Fig. 20)**: peptides with the largest K_D ($MOGK_2$ and $MOGR_2$) polarized T cells towards regulatory phenotypes while the other peptide sequences did not. When assessing the impact of complexes on inflammatory signaling, inflammatory cytokines were not produced by untreated cells or cells treated with CpG or CpG + GpG. This is not surprising as there was no MOG antigen present to activate the MOG-specific T cells in these controls. Of the cells stimulated with MOG antigen, all complex formulations reduced inflammatory cytokines, including IFNγ (**Fig. 19E**) and IL-6 (**Fig. 19F**), relative to control treatment using soluble MOG peptides without GpG. This result indicated that delivery of GpG was important for suppressing inflammatory signaling during dendritic cell and T cell interactions.

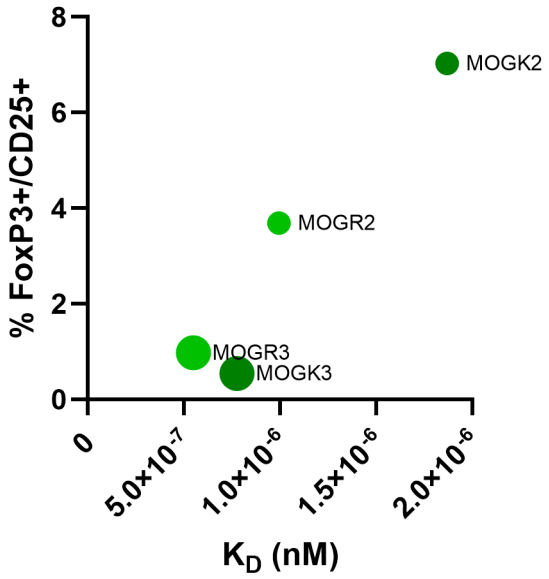

Figure 20. Percentage of T cells polarized towards regulatory phenotypes (FoxP3+/CD25+) vs. measured dissociation constant (K_D) between MOG peptides and GpG.

3.4) Concluding remarks

Taken together, our results suggest that a complex design that was sufficient to load immune signals without limiting availability of antigen during processing and presentation by dendritic cells was most effective in polarizing antigen-specific responses toward tolerance. Additionally, distinct MOG peptide designs may have impacted how or when antigen was processed by dendritic cells and presented to T cells; both concentration and duration of antigen display impact T cell response. After uptake, dendritic cells present external antigens in major MHC-II proteins. The ability of peptide antigens to be loaded into MHC complexes and the interactions between antigens and MHC within the binding groove depend on physical properties such as the geometry, charge distribution, and hydrophobicity of both the binding groove and the peptide, as well as the length of the peptide.[6,7] Any changes in this regard could impact the ability of T cells to recognize and respond to antigen within MHC. For example, the affinity with which a T cell binds antigen as well as the duration of the interaction impacts the T cell's level of activity and specificity.[11,151] Furthermore, loading of antigen into MHC-II with low affinity has been proposed as a mechanism for induction of autoimmune reactions in settings such as in type 1 diabetes.[152,153] Thus, further elucidation of the connections between design of peptide antigens and loading of antigen into MHC complexes will be a key consideration in the development of effective antigen-specific therapies. Overall, these results highlight key connections that could inform how to design immune cues with biophysical properties that help direct immunological outcomes.

CHAPTER 4: INTEGRATING MOLECULAR DYNAMICS SIMULATIONS TO ENABLE RATIONAL ASSEMBLY OF IMMUNE SIGNALS FOR IMMUNOTHERAPY

In Chapter 3.3.2, we discussed how total charge and anchored amino acid residue impacted the binding affinity between cationic MOG peptides and anionic GpG oligonucleotide. In particular, our studies revealed that MOG peptides anchored with arginine residues self-assembled with a higher binding affinity compared to MOG peptides anchored with lysine residues.[126] The differences in binding affinity impacted availability of GpG to inhibit inflammatory signaling in dendritic cells, illustrating the importance of biophysical design when engineering immunotherapies to program immune response. Incorporating biophysical design when engineering immunotherapies can provide a powerful lever to direct immune function to combat autoimmune disease. However, leveraging biophysical design to direct immune function requires a systematic understanding of how specific design parameters impact biophysical properties of self-assembled immunotherapies. Only once this understanding is achieved can immune signals be rationally designed to self-assemble with specific biophysical characteristics. Building off our previous studies, Chapter 4 implements the use of molecular dynamics simulations as tool to study how molecular interactions between MOG peptide and GpG change as a function of peptide design. Using computational methods, we compare molecular contacts - including hydrogen bonding and salt bridges - across a library of MOG peptides. These insights are used to define what contributed to differences in binding affinity between MOG peptides and GpG oligonucleotide, Insights from these analyses inform how rational design of immune cues can build self-assembled immunotherapies with specifically tuned biophysical properties.

4.1 Replica exchange molecular dynamics is a practical method for modeling self-assembly

Understanding the molecular interactions that take place during self-assembly of immune signals is important for rational design of immunotherapies. However, studying the initial self-assembly step is challenging to characterize experimentally due to the short timescale of assembly. From this perspective, computational approaches can be powerful tools to study self-assembly processes. Conventional molecular dynamics simulations have limited applications for studying self-assembly because these simulations can become trapped in local free-energy minimum conformations. Thus, traditional molecular dynamics approaches do not guarantee a sampling of all possible conformations of self-assembled biomolecules. Replica exchange molecular dynamics (REMD) is one enhanced sampling method that can be used to overcome this limitation.[154,155]

The REMD method combines molecular dynamics simulations with a Monte Carlo algorithm. During a REMD simulation, several replicas of the same system are simulated in parallel using molecular dynamics simulations at different temperatures. Periodically, swaps between neighboring replicas are attempted with a predefined probability of success (**Fig. 21**).

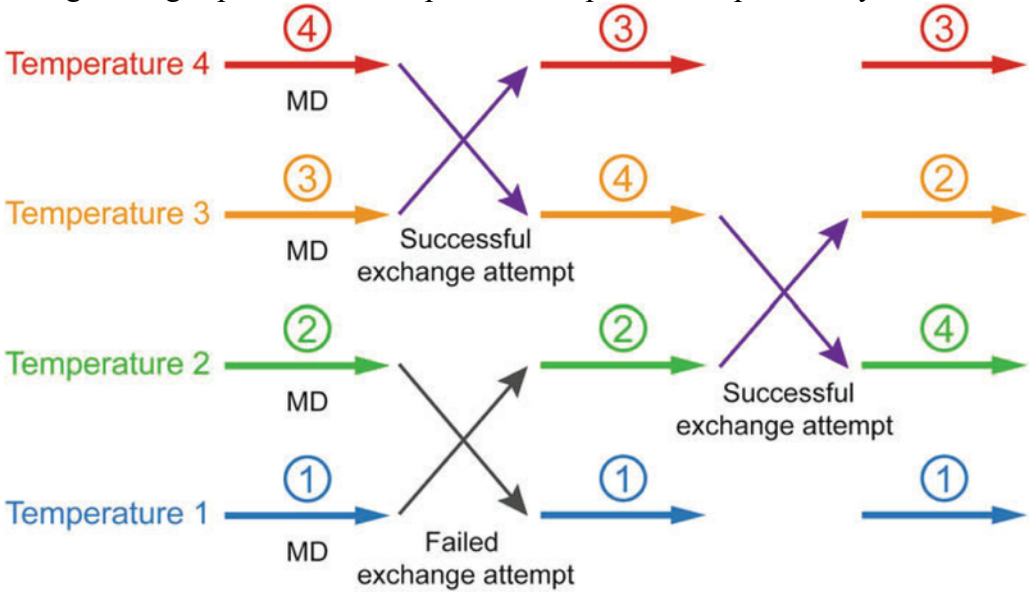

Figure 21: Illustration of replica exchange molecular dynamics method (ref 154).

Over the course of the simulation, this method can overcome high energy barriers and sufficiently sample all possible conformations. For example, if a conformation is trapped in an energy minimum, the conformation can eventually swap to a higher temperature replica where there is enough energy in the system to exit the local minima. In the following studies, we leveraged the REMD method to simulate self-assembly between MOG peptides and GpG oligonucleotide.

Motivated by our exciting results discussed in Chapter 3, we sought to develop tools that can inform rational design of immunotherapies with distinct biophysical properties. With this goal in mind, we employed REMD as a tool elucidate how molecular interactions between MOG peptides and GpG changed as a function of MOG peptide design. We hypothesized that MOG peptides anchored with arginine residues facilitated more electrostatic interactions with GpG than MOG peptides anchored with lysine residues. To test this hypothesis, we studied how peptide design influences molecular interactions between five MOG peptides ($MOGK_2$, KMOGK, $MOGR_2$, $MOGK_9$, $MOGR_9$) and GpG oligonucleotide. Elucidating differences in molecular interactions helped explain the experimentally measured differences we observed in binding affinity and highlights the use of molecular dynamics as a tool to inform biophysical design of immunotherapies.

4.2 Materials and Methods

4.2.1) Materials and software

For molecular dynamics simulations, MOG peptide and GpG oligonucleotide structures were generated with The PyMOL Molecular Graphics System, Version 2.0 Schrodinger, LLC. Simulations were set up using the CHARMM forcefield[156] and executed with the freely available GROMACS software package.[157] All simulations were completed with resources from University

of Maryland's High Performance Computing Cluster made available for conducting research reported in this manuscript. Data analysis was completed with both Python and Matlab.

For surface plasmon resonance studies, GpG DNA (5'-T*G*A*C*T*G*T*G*A*A*G*G*T*T*A*G*A*G*Z*T*G*A*-3') was purchased from IDT (Coralville, IA). GpG was synthesized with a biotin tag on the 5' end. MOG (MEVGWYRSPFSRVVHLYRNGK) peptides were synthesized by Genscript (Piscataway, NJ). MOG peptides were anchored with either arginine (R) or lysine (K) residues on the C-terminus or both the N-terminus and C-terminus. The MOG peptides studied by surface plasmon resonance included MOG, $MOGK_2$, $MOGR_2$, KMOGK, and RMOGR. HBS-N running buffer (0.01 M HEPES, 0.15 M NaCl, pH 7.4, filtered, degassed), 10 mM sodium acetate pH 5, amine couple kits (1-ethyl-3- (3- dimethylaminopropyl) carbodiimide (EDC) and N-hydroxysuccinimide (NHS)), 1 M ethanolamine, and Series S CM4 sensor chips were provided by Cytiva. Ethylenediaminetetraacetic acid (EDTA) was purchased from Sigma Aldrich (St. Louis, MO).

4.2.2) Temperature replica exchange molecular dynamics simulations

MOG peptide and GpG oligonucleotide sequences were generated with the Pymol software. After all sequences were generated, MOG/GpG systems were created for each MOG peptide. Each system contained a single MOG peptide and a single GpG oligonucleotide separated by 1 nm. A total of 5 systems were created: $MOGK_2$ + GpG, $MOGR_2$ + GpG, $MOGK_9$ + GpG, $MOGR_9$ + GpG, and KMOGK + GpG. Each system was contained in a 10x10x10 nm box with periodic boundaries. Each system was solvated with water and salt ions using the solution builder tool on CHARMM.[156] Total salt concentration was 150 mM of monovalent salt ions. Once solvated, energy minimization and equilibration steps were completed for each system as directed

by the output files from CHARMM using GROMACS 2019.4 on University of Maryland's High Performance Computing Cluster. After equilibration, an initial 50ns simulation was completed for each individual system. The MOG/GpG conformations found at the end of this step were used as the starting conformations in subsequent simulations.

After the initial simulation was completed, water and salt ions were removed from each system, leaving just the complexed MOG peptide and GpG oligonucleotide. Each system was then run through the Enhanced Sampler tool on CHARMM. During this step, the system was solvated again with the same conditions mentioned above. Additionally, the CHARMM36m force field was applied to the system and the Temperature Replica Exchange MD (T-REMD) option was selected under the Enhanced Method Input Options. The minimum and maximum temperatures were set to 298K and 440K, respectively, with an exchange probability of 0.21. Dynamics Input Generation Options was set to NVT Ensemble. The number of replicas and Enhanced Sampler inputs were generated for each of the systems after completing these steps. Energy minimization and equilibrium steps were completed for each system as directed by the output files from CHARMM. Once equilibrated, all replicas within each system were simulated in parallel using GROMACS 2019.4 on University of Maryland's High Performance Computing Cluster. Each system was simulated for 300-350ns until convergence was achieved.

4.2.3) Computational analysis

After a simulation was terminated, the data was demultiplexed in GROMACS using the demux.pl script. This step created replica_index.xvg and replica_temp.xvg files that are necessary to analyze data at specific temperatures of interest. Once the files were created, the total energies for all frames in each temperature replica were extracted. Then, MDAnalysis was used to identify

and extract values for radius of gyration, total contacts, hydrogen bonds, and salt bridges.[158] The radius_of_gyration() attribute was used to calculate the radius of gyration of complexed MOG and GpG in each frame. All atoms on MOG and GpG were treated as a single entity to compute the radius. Total contacts were calculated by computing the distance of all non-hydrogen atoms on the MOG peptide and all non-hydrogen atoms on the GpG oligonucleotide. Any non-hydrogen atoms within a 4.5 Å distance were recorded as a contact. The cutoff of 4.5 Å was recommended by MDAnalysis usage documentation for native contact analysis of all-atom simulations. The hydrogen bond analysis (HBA) class was used to identify hydrogen bond donors and acceptor on both MOG peptide and GpG oligonucleotide. Only hydrogen bond pairs between an atom on MOG peptide and an atom on GpG oligonucleotide were computed, and the total hydrogen bonds formed were recorded for each frame. Salt bridges were computed using the same native contact analysis as mentioned for total contacts, but more parameters were specified. Salt bridges were identified as a contact between a nitrogen atom on arginine, lysine, or histidine residues of MOG peptide and an oxygen atom on GpG oligonucleotide. A 4 Å cutoff distance was used for salt bridges.[159,160] Once all measures of interest were computed, free energy differences were computed using the multistate Bennet acceptance ratio estimator (MBAR).[161] The code for completing the analysis was obtained from Github.[162] In short, values for total energies and torsions from each simulation were read in by temperature. The trajectories of each replica in each simulation were reconstructed to reflect their true temporal correlation, and then subsampled to produce statistically independent samples and collected by temperature. Then, dimensionless free energies were calculated at each temperature using MBAR; the dimensionless free energies are referred to as the Potential Mean Force (PMF). The torsions were binned into sequentially labeled bins in two dimensions and the relative free energies and uncertainties were estimated at 298K. The dimensions used for analysis

were the parameters of interest identified above (radius of gyration, total contacts, hydrogen bonds, salt bridges). The outputs contained values for PMF as a function of the parameters of interest.

4.2.4) Surface plasmon resonance

Experiments were performed on the Biacore T200 instrument. GpG was immobilized to a Series S CM4 sensor chip and the different MOG peptides were flowed over the chip to analyze binding affinity between MOG and GpG. Flow rates during the experiment were 30 ul/min unless indicated otherwise and detection temperature was 25°C. To start, the CM4 chip was activated with an 8 minute injection of a mixed solution of 0.4 M EDC and 0.1 M NHS. Neutravidin was diluted in 10 mM sodium acetate pH 5 to a final concentration of 50 ug/mL and injected for 10 minutes to couple neutravidin to the sensor chip. The surface was then blocked with a 7 minute injection of 1 M ethanolamine pH 8.5 to remove any remaining reactive species on the surface. After couple neutravidin to the surface, biotinylated GpG was immobilized on the surface by diluting GpG in HBS-N running buffer to 1 ug/mL and injecting for 20-60 seconds. To measure kinetic curves, all MOG peptides were diluted in HBS-N running buffer to concentrations of 4800, 3600, 2400, and 1200 nM and flown over the sensor chip with a total contact time of 2 minutes. HBS-N buffer with no peptide (0 nM) was used as a baseline for each run. In between each kinetic curve, the surface of the chip was regenerated with a single injection of HBS-N running buffer for 60 seconds. For each MOG peptide, the five concentrations (including 0 nM) were fitted to a two-state binding model and K_D was calculated based on the association and dissociation rates between MOG peptides and GpG.

4.2.5) Statistical analysis

Statistical analysis for the modeling data was completed during the MBAR analysis. As mentioned, the trajectories of each replica in each simulation were reconstructed to reflect their true temporal correlation, and then subsampled to produce statistically independent samples. Explanations of how uncertainties for free energies and PMF were estimated can be found from the source.[161] For surface plasmon resonance, one-way ANOVA with Tukey post-test corrections for multiple comparisons was used to compare groups. Statistical calculations were performed using JMP Pro (v14, SAS institute).

4.3) Results and Discussion

4.3.1) MOG peptide and GpG oligonucleotide self-assemble into 13 Å conformations

In Chapter 3, we described how surface plasmon resonance studies indicated that MOG peptides anchored with arginine residues bound to GpG oligonucleotide with a higher affinity than MOG peptides anchored with lysine residues. We hypothesized that this difference occurred because MOG peptides anchored with arginine residues facilitate more electrostatic interactions with GpG than MOG peptides anchored with lysine residues. We also observed that increasing the total charge of MOG peptide increased its binding affinity to GpG. We hypothesized that this difference occurred because MOG peptides formed more molecular interactions with GpG as more cationic amino acid residues were anchored to the peptide sequence. To test our hypotheses, we used the REMD method to simulate self-assembly of $MOGK_2$, $MOGR_2$, $MOGK_9$, and $MOGR_9$ with GpG. We also simulated self-assembly of KMOGK with GpG and compared to $MOGK_2$ to study how charge distribution in the peptide influenced molecular interactions during self-assembly when total charge was held constant.

After simulations were completed, we performed two quality control analyses before interpreting the data. First, we plotted the radius of gyration of the MOG/GpG complex over two non-overlapping time intervals in the last 100ns of each simulation. If the simulations converged, we would expect to see the same results within both time intervals. Determining where the simulation converges is important for identifying the time interval over which computational analyses can be completed. Second, we generated heatmaps that illustrated the temperatures of all replicas over the course of the simulation. These plots were used to confirm that temperature mixing occurred throughout the replicas, which provides confidence that all possible conformations had been sampled during the simulation. Completing this quality control step ensures that any analysis of molecular interactions factors in all possible conformations.

Examining the $MOGK_2$ first, we plotted Potential Mean Force (PMF) vs. radius of gyration to visualize the conformations at four different time intervals (**Fig. 22A**). This graph illustrates the relative free energy (PMF) of the $MOGK_2$/GpG complex at different radii. When analyzing the intervals of 250-300ns and 300-350ns, we observed little separation between the two graphs. When analyzing the 0-100ns and 100-250ns intervals, we saw large differences compared to the 250-300ns and 300-350ns graphs. These results indicate that the $MOGK_2$ simulation converged over the last 100ns of the simulation. Next, we analyzed the temperature mixing of the $MOGK_2$ simulation (**Fig. 22B**). The heatmap illustrates the temperature at which a replica (y-axis) is being simulated at a given timestep (x-axis) of the simulation, where yellow indicates high temperature and blue indicates low temperature. The substantial mix of yellow and blue colors across all replicas and time steps indicates that temperature mixing did indeed occur during the $MOGK_2$ simulation. Similar observations were made for $MOGR_2$ (**Fig. 22C-D**), KMOGK (**Fig. 22E-F**), $MOGK_9$ (**Fig. 23A-B**), and $MOGR_9$ (**Fig. 23C-D**). The PMF vs. radius of gyration graphs did

exhibit some separation at larger radii for all simulations. This indicated that the simulations could be run for longer to gather more data to see if better convergence may be reached at the larger radii. To avoid analyzing potentially non-converged data, the analyses in subsequent sections focus on conformations with radii less than 15 Å where convergence was achieved. We were particularly

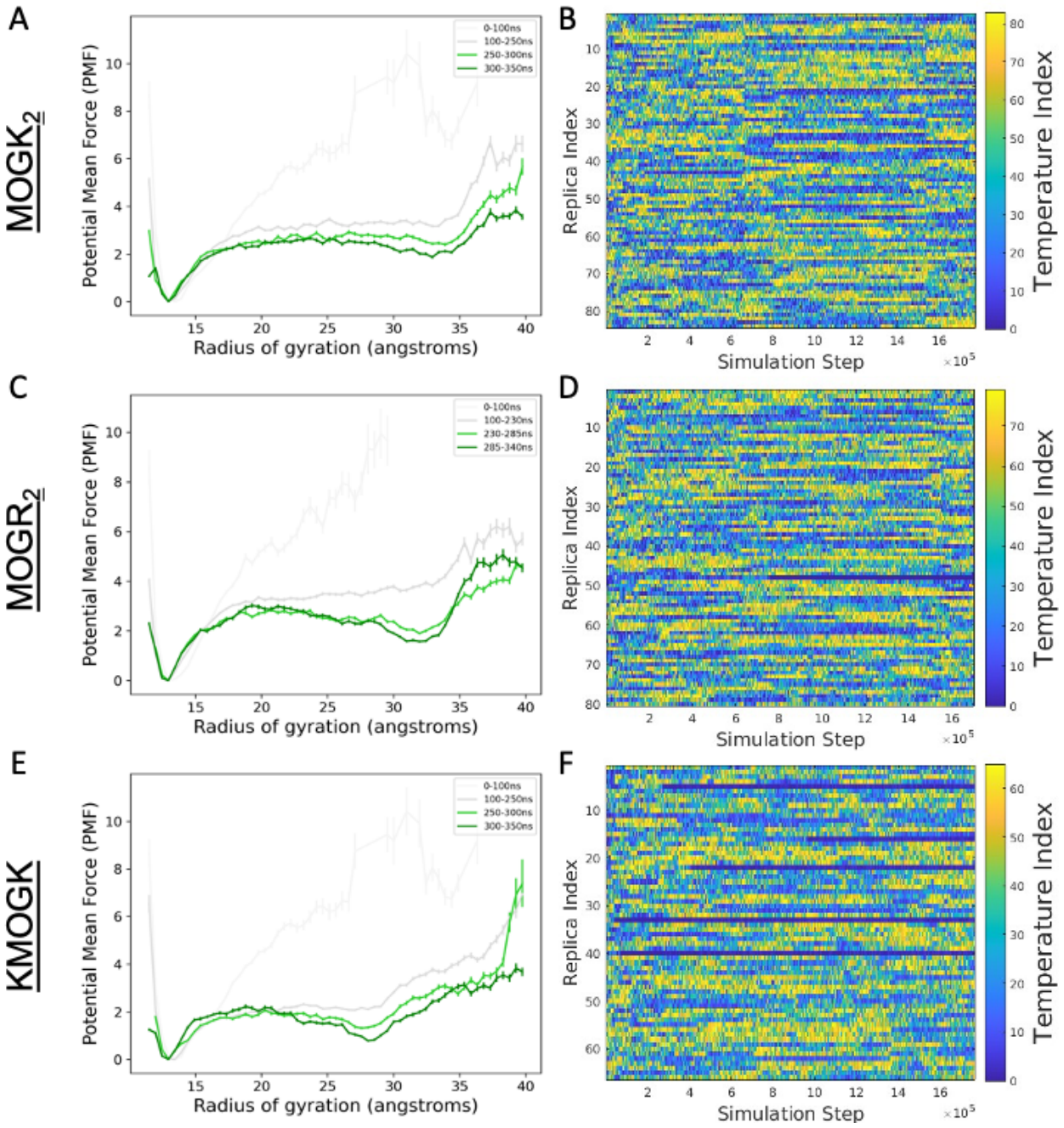

Figure 22. Quality control data looking at simulation convergence and temperature mixing for A+B) $MOGK_2$, C+D) $MOGR_2$, and E+F) KMOGK.

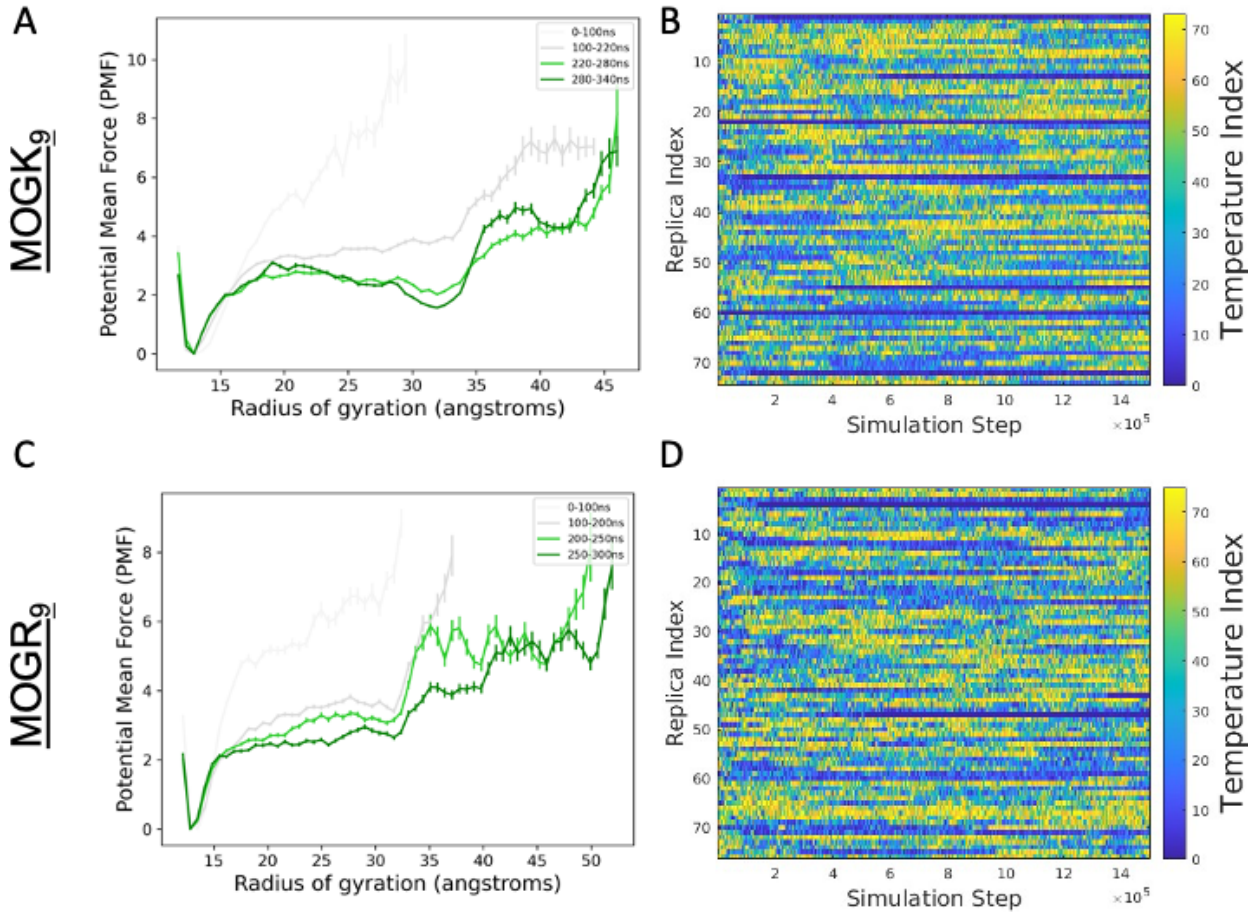

Figure 23. Quality control data looking at simulation convergence and temperature mixing for A+B) $MOGK_9$ and C+D) $MOGR_9$.

interested in the conformation at these radii to study the interactions that facilitate the lowest energy conformations. Understanding the interactions within the lowest energy conformations informs what biophysical factors and design parameters facilitate the most stable conformations during self-assembly of immune signals.

After confirming convergence and temperature mixing, we more closely examined the conformations of MOG/GpG complexes and what percentage of time during the simulation the complexes were found in each conformation. We used differences in radius of gyration to distinguish between different conformations. Comparing the conformations of all 5 peptide simulations, we found that all MOG/GpG complexes were at their lowest energy states when the

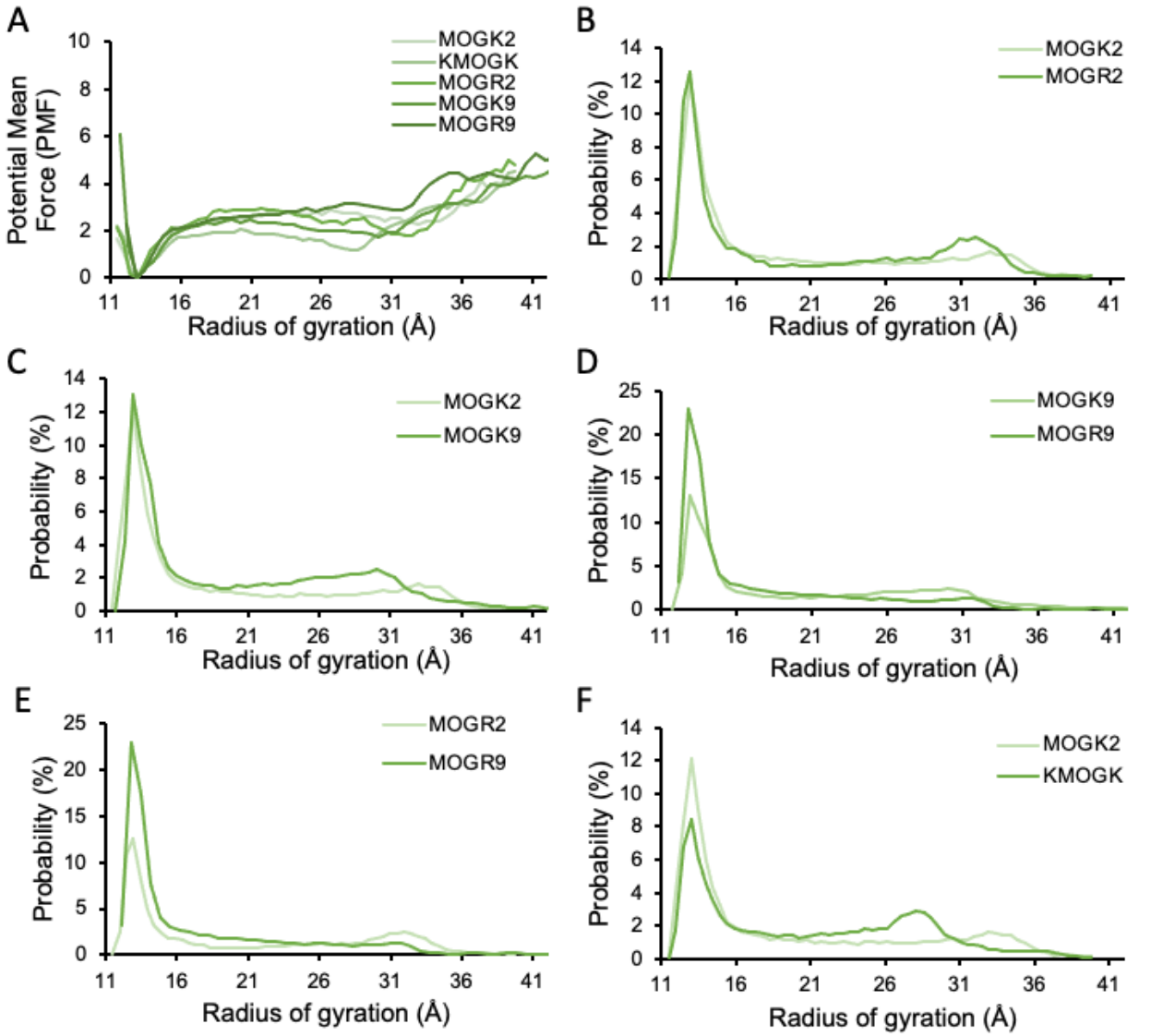

Figure 24. A) Relative energies (PMF) of MOG/GpG conformations at different radii of gyration. Comparing probability of MOG/GpG conformations to be found with different radii over the course of the simulation for B) $MOGK_2$ vs. $MOGR_2$, C) $MOGK_2$ vs. $MOGK_9$, D) MOGK9 vs. $MOGR_9$, E) $MOGR_2$ vs. $MOGR_9$, and F) $MOGK_2$ vs. KMOGK.

radius of the MOG/GpG complex was between 12-15Å (**Fig. 24A**). All MOG/GpG complexes were at their lowest energy state at 13Å, indicating that neither the peptide length nor charge impacted the size of the most stable complex. However, we did observe differences in the probabilities of MOG/GpG complexes to be found in their lowest energy conformations. Probabilities were calculated by dividing the number of frames found in each radius of gyration bin by the total number of frames being analyzed. For this analysis, different converged time

intervals were analyzed for each MOG peptide simulation so that the total number of frames being analyzed were all within 1% of each other. $MOGK_2$ had very similar conformation profiles to $MOGR_2$ (**Fig. 24B**) and $MOGK_9$ (**Fig. 24C**). Interestingly, when comparing $MOGK_9$ to $MOGR_9$ (**Fig. 24D**), $MOGR_9$ was almost twice as likely to be in its lowest energy conformation as $MOGK_9$. Similarly, $MOGR_9$ was almost twice as likely to be in lowest energy conformation as $MOGR_2$ (**Fig. 24E**). Given $MOGR_9$'s significantly higher cationic charge than $MOGR_2$, one can intuit that $MOGR_9$ binds to GpG with a higher binding affinity, and thus is more likely to be found in a tightly bound conformation than $MOGR_2$. Given that arginine confers a higher binding affinity than lysine (Chapter 3),[126] the same trend makes sense when comparing $MOGR_9$ to $MOGK_9$. The same large difference was not observed when comparing $MOGK_2$ and $MOGK_9$ at its 13Å conformation (**Fig. 24C**). $MOGK_9$ does have a secondary conformation at ~30Å that is almost twice as likely as $MOGK_2$ (**Fig. 24C**). $MOGK_2$ was more likely to be found in its lowest energy conformation than KMOGK, and KMOGK had a secondary conformation that it was more likely to be in than $MOGK_2$ (**Fig. 24F**). This result indicates that, in addition to total charge and anchored amino acid residue, charge distribution on MOG peptide also impacts self-assembly of MOG peptide and GpG oligonucleotide.

Overall, analyzing differences in conformation was not enough of a predictor, on its own, of the binding affinity between MOG peptides and GpG. For example, we know that MOG peptides with more cationic charge have a higher binding affinity for GpG than MOG peptides with less cationic charge.[126] However, $MOGR_9$ was almost twice as likely to be in its lowest energy conformation as $MOGR_2$ (**Fig. 24E)**, while $MOGK_9$ was equally likely to be in its lowest energy conformation as $MOGK_2$ (**Fig. 24C)**. Thus, additional insights are necessary that explain the differences in binding affinity in order to have predictive power with molecular dynamics.

4.3.2) Peptide charge, anchored residue, and charge density alter interaction profiles between MOG and GpG

To better understand how the conformational differences correspond to binding affinity between MOG peptides and GpG, we next analyzed how many contacts are formed during self-assembly as a function of peptide design. When comparing $MOGK_2$ to $MOGK_9$ (**Fig. 25A**) and

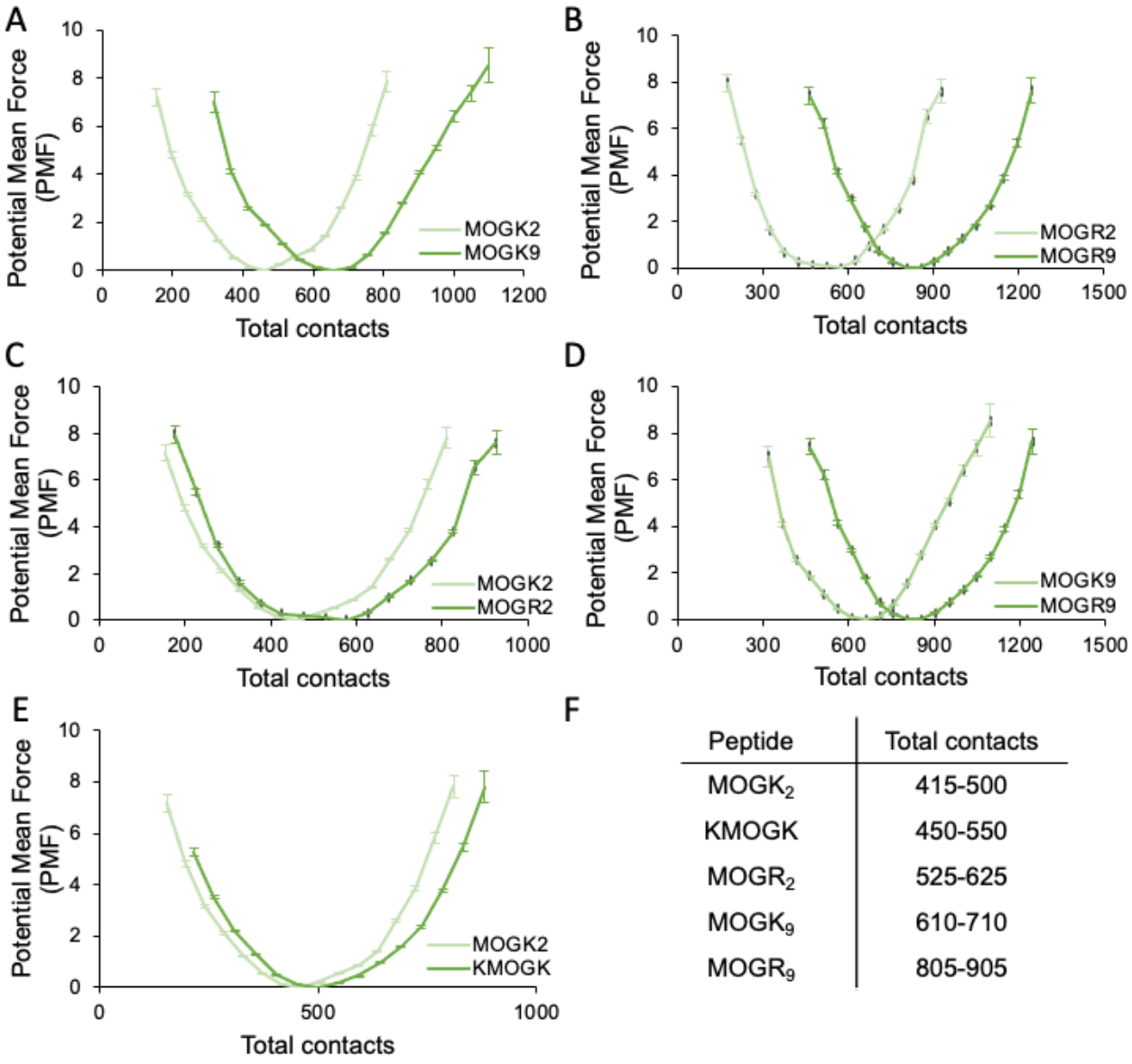

F

Peptide	Total contacts
$MOGK_2$	415-500
KMOGK	450-550
$MOGR_2$	525-625
$MOGK_9$	610-710
$MOGR_9$	805-905

Figure 25. Comparisons of total contacts formed between MOG peptides and GpG for A) $MOGK_2$ vs. $MOGK_9$, B) $MOGR_2$ vs. $MOGR_9$, C) $MOGK_2$ vs. $MOGR_2$, D) $MOGK_9$ vs. $MOGR_9$, and E) $MOGK_2$ vs. KMOGK. F) Total contacts formed between each MOG peptide and GpG at their lowest energy conformations.

$MOGR_2$ to $MOGR_9$, (**Fig. 25B**), we observed large differences in the total contacts formed when MOG/GpG complexes were in their lowest energy states. Compared to $MOGK_9$, $MOGK_2$ formed 200 fewer contacts with GpG in its lowest energy states (**Fig. 25A, 25F**). Even more strikingly, $MOGR_2$ formed almost 300 fewer contacts than $MOGR_9$ in its lowest energy states (**Fig. 25B, 25F**). Given that $MOGK_9$ and $MOGR_9$ peptides have more cationic charge and longer sequence lengths than $MOGK_2$ and $MOGR_2$, this result holds physical significance. Interestingly, when comparing $MOGK_2$ to $MOGR_2$ (**Fig. 25C, 25F**) and $MOGK_9$ to $MOGR_9$ (**Fig. 25D, 25F**), we observed that MOG peptides anchored with arginines residues formed 100-200 more contacts than MOG peptides anchored with lysine residues. These data align well with the experimental results that indicate arginine confers a higher binding affinity than lysine during electrostatic self-assembly (Chapter 3). When comparing $MOGK_2$ to KMOGK (**Fig. 25E, 25F**), $MOGK_2$ formed slightly fewer contacts with GpG than KMOGK. The larger range of contacts formed by KMOGK likely contributed to the increased probability of being found in a secondary conformation compared to $MOGK_2$ (**Fig. 24F**).

In addition to total contacts between MOG peptides and GpG, we were also interested in analyzing the specific contacts formed between amino acids of the MOG peptide sequence and nucleotides of the GpG oligonucleotide sequence. To perform this analysis, we computed all contacts formed between amino acids of MOG and nucleotides of GpG and then calculated what frequency each amino acid and nucleotide pair was of the total contacts formed. Using this data, heatmaps were generated to visualize frequencies of each amino acid and nucleotide contact relative to all contacts formed.

Figure 26 illustrates clear differences in the types of contacts that drive self-assembly between MOG peptides and GpG. $MOGK_2$ (**Fig. 26A**) interacted more with the 5' end of GpG,

indicated by the presence of contacts with a relative frequency of ~0.25-0.3 on the left side of the heatmap and contacts with a relative frequency of ~0.1 on the right side of the heatmap. The heatmap of $MOGR_2$ (**Fig. 26B**) indicates contacts with relative frequency of ~0.2-0.25 were formed with both the 5' and 3' ends of GpG. Intriguingly, anchoring MOG peptide with arginine

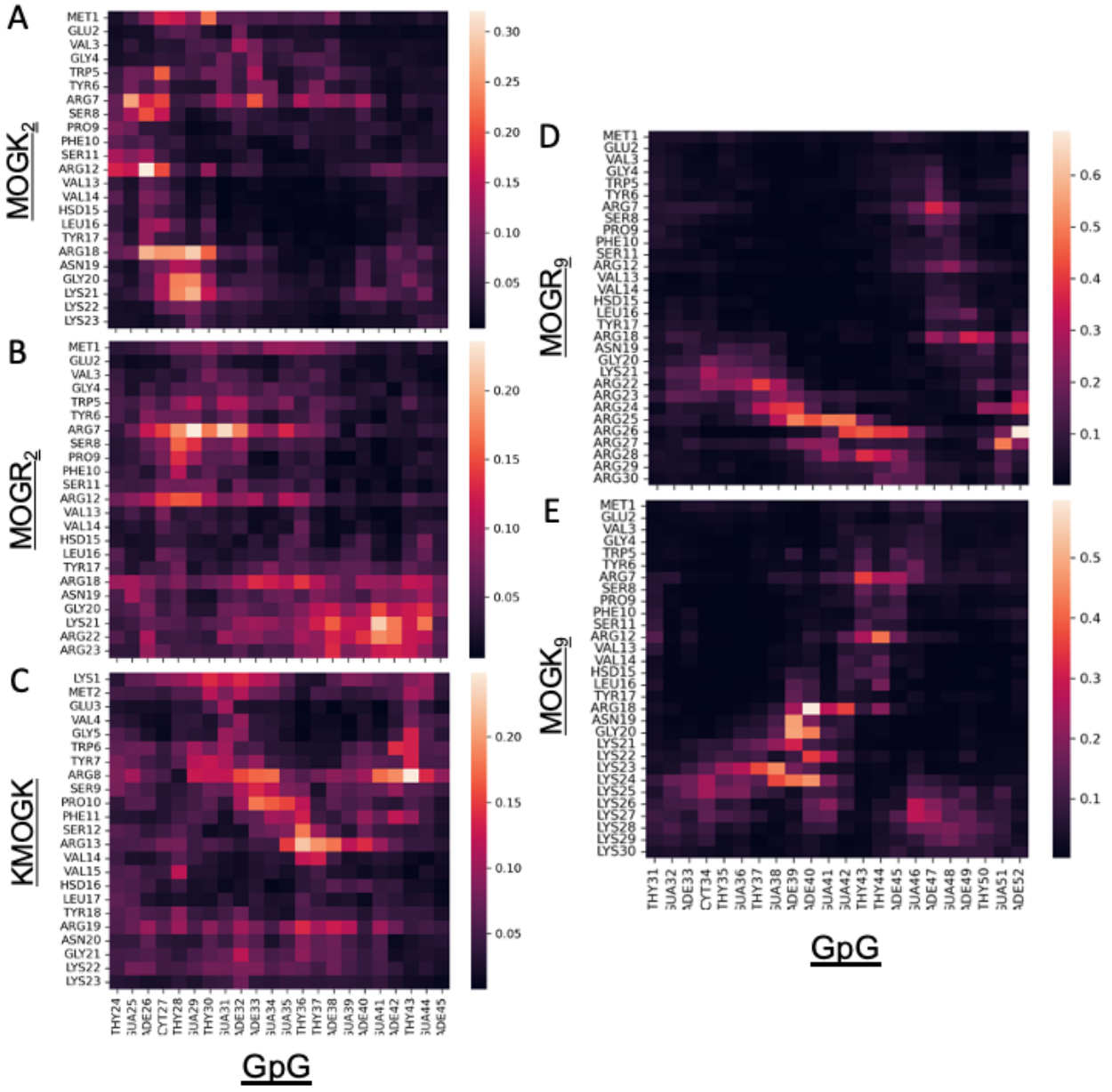

Figure 26. Contact heatmaps showing relative contact frequency between (y-axis) amino acids of A) $MOGK_2$, B) $MOGR_2$, C) KMOGK, D) $MOGR_9$, E) $MOGK_9$ and (x-axis) nucleotides of GpG. Color bars indicate relative frequency, with bright colors as high frequency and dark colors as low frequency.

residues on the C terminus facilitated more contacts with the 3' end of GpG, while anchoring MOG peptide with lysine residues on the C terminus facilitated more contacts with the 5' end of GpG. When MOG peptide was anchored with lysine residues on both the N and C terminus (**Fig. 26C**), contacts with a relative frequency of 0.2 or higher were not seen at the 5' end of GpG like they were with $MOGK_2$. These data indicate molecular interactions between MOG peptide and GpG are influenced by both the type of anchored amino acid residue and the distribution of charge on the peptide sequence.

Analyzing the contact heatmaps of $MOGR_9$ (**Fig. 26D**) and $MOGK_9$ (**Fig. 26E**), the differences in interaction profiles are even more stark compared to the lower charge peptides. The highest frequency contacts of $MOGR_9$ and $MOGK_9$ range from ~0.5-0.7, which is more than double the ~0.2-0.3 range of $MOGK_2$, $MOGR_2$, and KMOGK. The heatmaps of $MOGK_9$ and $MOGR_9$ contain broad areas with contact frequencies less than 0.1 and tight zones of high frequency contacts of ~0.4-0.7. The higher total charge and high charge density of the arginine and lysine tales of $MOGK_9$ and $MOGR_9$ facilitated fewer types of contacts between MOG peptide and GpG, but these contacts occurred at high frequency. This contrasts with the heatmaps of $MOGK_2$, $MOGR_2$, and KMOGK, which have broad areas where contact frequencies are ~0.1-0.3. Thus, the lower charge peptides facilitated more types of contacts between MOG peptide and GpG, but these contacts occurred at lower overall frequencies.

Considering these results with the surface plasmon resonance data described in Chapter 3, we see an intriguing association between experimentally measured binding affinity and computationally modeled molecular interaction. Self-assembly of MOG peptides characterized with a lower binding affinity for GpG ($MOGK_2$ and $MOGR_2$) were driven by more types of contacts that were weaker and occurred at lower frequencies. Self-assembly of MOG peptides

characterized with a higher binding affinity for GpG ($MOGK_9$ and $MOGR_9$) were driven by fewer types of contacts that were stronger and occurred at higher frequencies. This kind of insight highlights the potential of using computational modeling to help design self-assembly of immune signal with designed biophysical characteristics, such as high or low binding affinity. For example, one may need to design immune signals with a binding affinity that's high enough to achieve self-assembly but low enough to effectively exert their biological function, as described in Chapter 3. Another context may require more tightly bound immune signals to facilitate better protection from environmental factors such as enzymatic degradation. To achieve such granularity and predictive power, it will be important to understand not only where and how many contacts are forming, but also the specific type of molecular interactions that influence differences in biophysical characteristics. One commonality with all MOG peptides was that the highest frequency contacts always included arginine or lysine residues. This points to the importance of charged amino acids in driving molecular interactions during electrostatic self-assembly of MOG peptides and GpG oligonucleotide.

4.3.3) Arginine residues facilitate more electrostatic interactions than lysine residues

Since self-assembly of MOG peptides and GpG oligonucleotide is driven by electrostatics, we analyzed how molecular interactions driven by charge polarity changed as a function of MOG peptide design. We started by computing how many hydrogen bonds were formed between MOG and GpG in the different simulations and analyzed how the number of hydrogen bonds changed with different MOG peptide designs. When comparing $MOGK_2$ vs. $MOGK_9$ (**Fig. 27A 27F**) and $MOGR_2$ vs. $MOGR_9$ (**Fig. 27B, 27F**), we observed $MOGK_2$ and $MOGR_2$ formed 6 and 10 fewer hydrogen bonds, respectively, with GpG in their lowest energy states. These results indicate that MOG peptides with higher cationic charge and longer sequence lengths formed more hydrogen

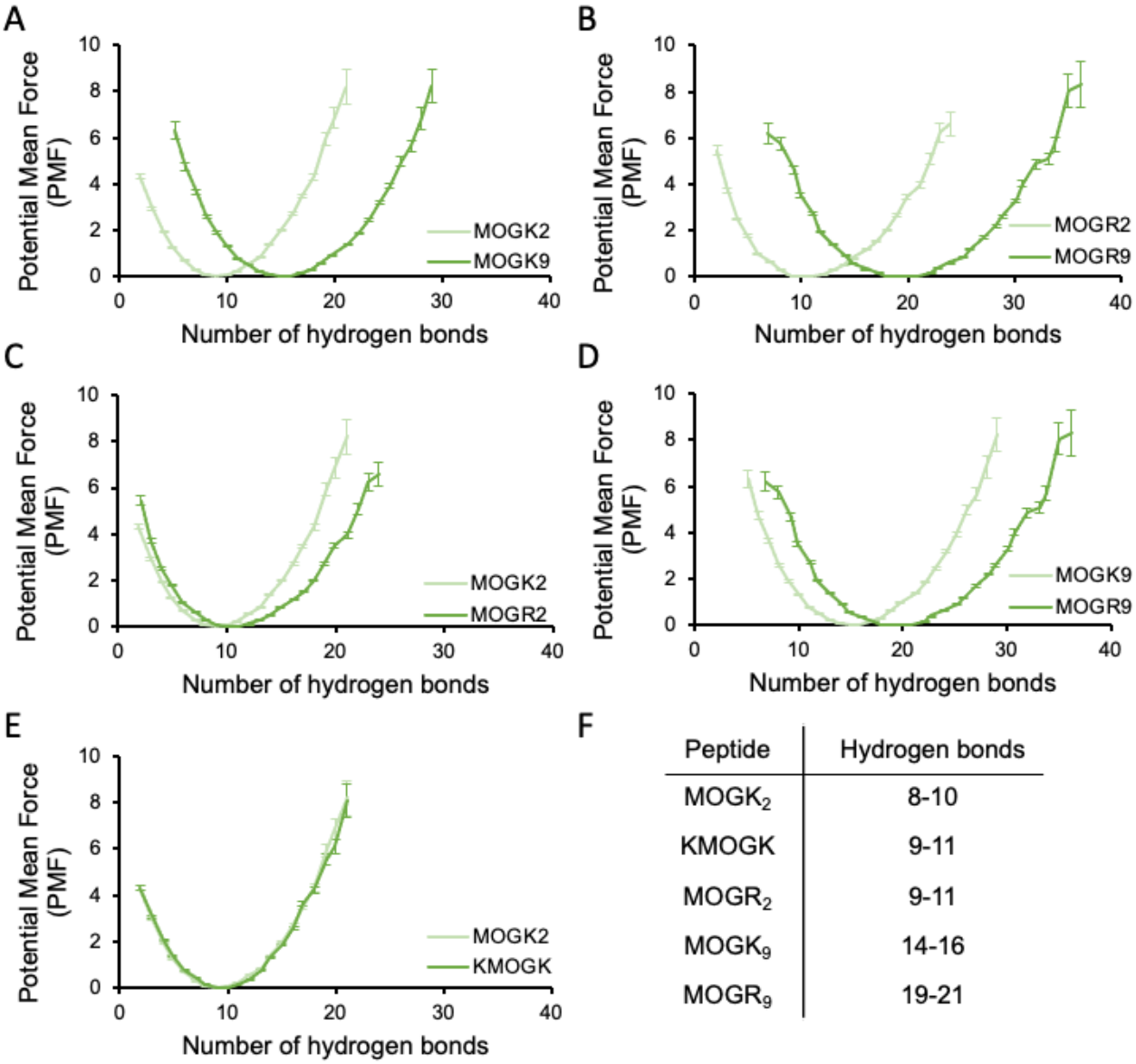

F

Peptide	Hydrogen bonds
$MOGK_2$	8-10
KMOGK	9-11
$MOGR_2$	9-11
$MOGK_9$	14-16
$MOGR_9$	19-21

Figure 27. Comparisons of hydrogen bonds formed between MOG peptides and GpG for A) $MOGK_2$ vs. $MOGK_9$, B) $MOGR_2$ vs. $MOGR_9$, C) $MOGK_2$ vs. $MOGR_2$, D) $MOGK_9$ vs. $MOGR_9$, and E) $MOGK_2$ vs. KMOGK. F) Number of hydrogen bonds formed between each MOG peptide and GpG at their lowest energy conformations.

bonds compared to MOG peptides with lower cationic charge and shorter sequence lengths. When comparing $MOGK_2$ vs. $MOGR_2$ (**Fig. 27C, 27F**) and $MOGK_9$ vs. $MOGR_9$ (**Fig. 27D, 27F**), we observed $MOGK_2$ and $MOGK_9$ formed 1 and 5 fewer hydrogen bonds, respectively, with GpG in their lowest energy states. When comparing $MOGK_2$ vs. KMOGK (**Fig. 27E, 27F**), we observed $MOGK_2$ formed 1 less hydrogen bond with GpG than KMOGK in their lowest energy states. These

results indicate that MOG peptides anchored with arginine residues formed more hydrogen bonds with GpG than MOG peptides anchored with lysine residues. The number of hydrogen bonds was not impacted when distributing the charge by anchoring lysine on both the N and C terminus (KMOGK), as opposed to just the C terminus ($MOGK_2$).

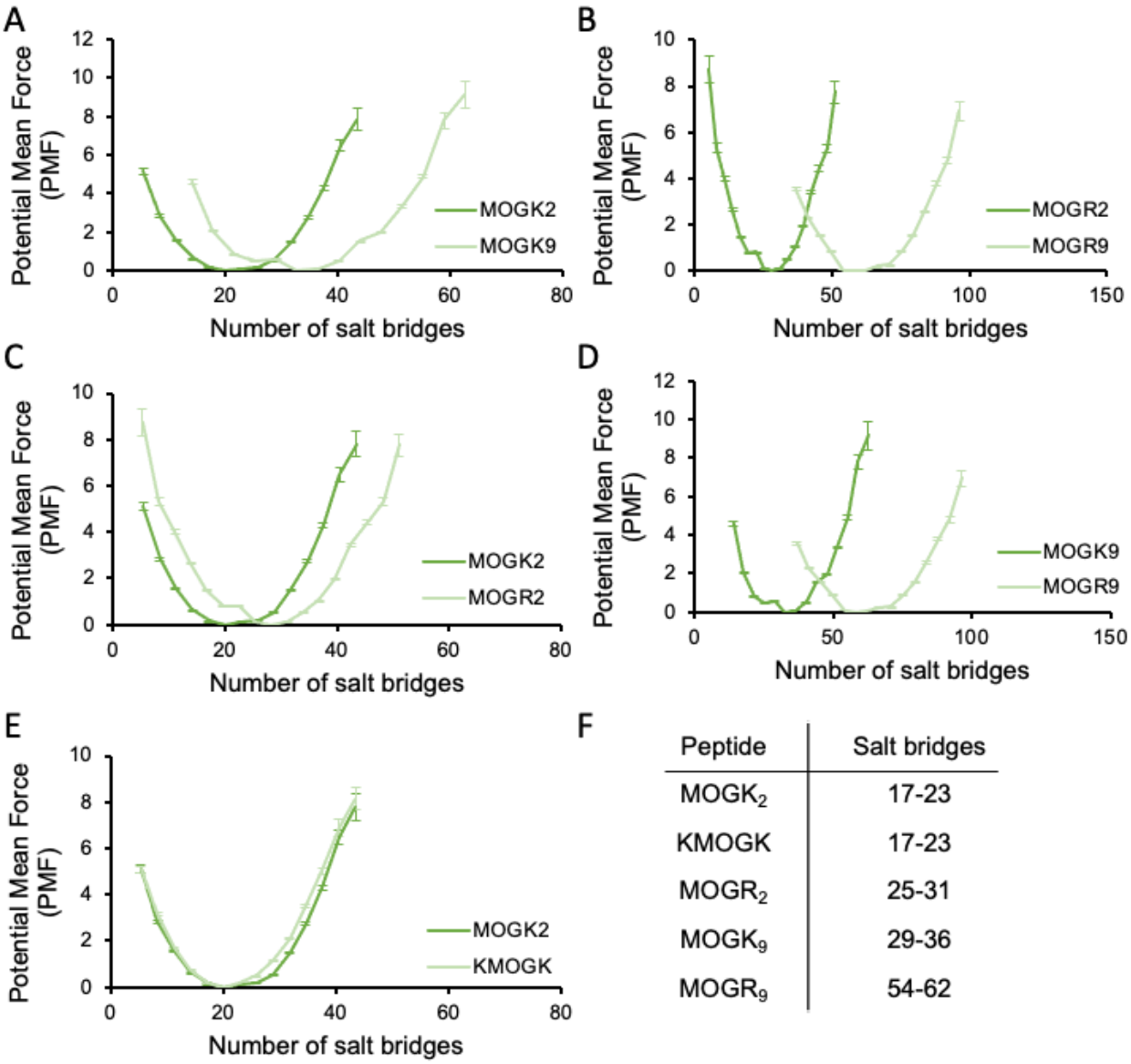

Peptide	Salt bridges
$MOGK_2$	17-23
KMOGK	17-23
$MOGR_2$	25-31
$MOGK_9$	29-36
$MOGR_9$	54-62

Figure 28. Comparisons of salt bridges formed between MOG peptides and GpG for A) $MOGK_2$ vs. $MOGK_9$, B) $MOGR_2$ vs. $MOGR_9$, C) $MOGK_2$ vs. $MOGR_2$, D) $MOGK_9$ vs. $MOGR_9$, and E) $MOGK_2$ vs. KMOGK. F) Number of salt bridges formed between each MOG peptide and GpG at their lowest energy conformations.

Because MOG and GpG are designed to self-assemble via electrostatic interactions, we also analyzed formation of salt bridges and how the number of salt bridges changed with different MOG peptide designs. Salt bridges were defined as a contact between a nitrogen on arginine, lysine, or histidine on the MOG peptide and an oxygen on the GpG oligonucleotide. When comparing $MOGK_2$ vs. $MOGK_9$ (**Fig. 28A, 28F**) and $MOGR_2$ vs. $MOGR_9$ (**Fig. 28B, 28F**), we observed $MOGK_2$ and $MOGR_2$ formed 12-13 and 29-31 fewer salt bridges, respectively, with GpG in their lowest energy states. These results indicate that MOG peptides with higher cationic charge and longer sequence lengths formed more salt bridges compared to MOG peptides with lower cationic charge and shorter sequence lengths. When comparing $MOGK_2$ vs. $MOGR_2$ (**Fig. 28C, 28F**) and $MOGK_9$ vs. $MOGR_9$ (**Fig. 28D, 28F**), we observed $MOGK_2$ and $MOGK_9$ formed 8 and 25-26 fewer salt bridges, respectively, with GpG in their lowest energy states. When comparing $MOGK_2$ vs. KMOGK (**Fig. 28E, 28F**), we observed $MOGK_2$ and KMOGK formed the same number of salt bridges with GpG in their lowest energy states. These results indicate that MOG peptides anchored with arginine residues formed more salt bridges with GpG than MOG peptides anchored with lysine residues. The number of salt bridges was not impacted when distributing the charge by anchoring lysine on both the N and C terminus (KMOGK), as opposed to just the C terminus ($MOGK_2$).

Our analysis of electrostatic interactions reveals that arginine residues facilitate a greater number of hydrogen bonds and salt bridges, compared to lysine residues, during self-assembly of MOG peptide and GpG oligonucleotide. Given that self-assembly of MOG and GpG is driven by electrostatics, the ability of arginine to form more hydrogen bonds and salt bridges than lysine likely conferred a higher binding affinity to MOG peptides anchored with arginine residues during the surface plasmon resonance studies described in Chapter 3. Similarly, MOG peptides with

higher total charge ($MOGK_9$ and $MOGR_9$) facilitated a greater number of hydrogen bonds and salt bridges compared to MOG peptides with lower total charge ($MOGK_2$ and $MOGR_2$). However, with this analysis, it is difficult to distinguish between the effect of the inherent peptide charge and the presence of more amino acids to facilitate more electrostatic interactions. A different modeling approach, like coarse grained methods, would be more suitable to elucidating the effects of overall charge balance on self-assembly. Anchoring MOG with lysine residues on both the N and C terminus did not result in differences in hydrogen bond or salt bridge formation compared to anchoring MOG with lysine residues on only the C terminus. From a design perspective, this may indicate that computing differences in electrostatic interactions would not on its own predict the effect of charge distribution on biophysical properties like binding affinity. Modeling peptides such as RMOGR, K_4-MOG-K_5, and R_4-MOG-R_5 and comparing the results to $MOGR_2$, $MOGK_9$, and $MOGR_9$, respectively, would provide valuable insight to better determine how electrostatic interactions change as a function of charge distribution.

4.3.5) Effects of distributing charge density are different when comparing lysine to arginine

Seeing no differences in electrostatic interactions as a function of charge distribution, one initial hypothesis was that utilizing the contact heatmaps as a secondary indicator would be useful in predicting how binding affinity would change as a function of charge density. When comparing contact heatmaps of $MOGR_2$ and $MOGK_2$ (**Fig. 26A, 26B**), we observed fewer areas of low frequency contacts with $MOGR_2$ than $MOGK_2$, Given that $MOGR_2$ binds to GpG with a higher binding affinity than $MOGK_2$, a greater distribution of contacts between MOG and GpG could be another indicator of relatively higher binding affinity. When comparing MOGK2 and KMOGK (**Fig. 26B, 26C**), we observed that KMOGK has fewer areas of low frequency contacts than $MOGK_2$. Since KMOGK has the same total charge and sequence length as $MOGK_2$, we

hypothesized that the larger range of contacts seen with KMOGK would indicate a higher binding affinity for GpG.

To test this initial hypothesis, we used surface plasmon resonance to measure the binding affinity between GpG and MOG (**Fig. 29A**), $MOGK_2$ (**Fig. 29B**), $MOGR_2$ (**Fig. 20C**), KMOGK

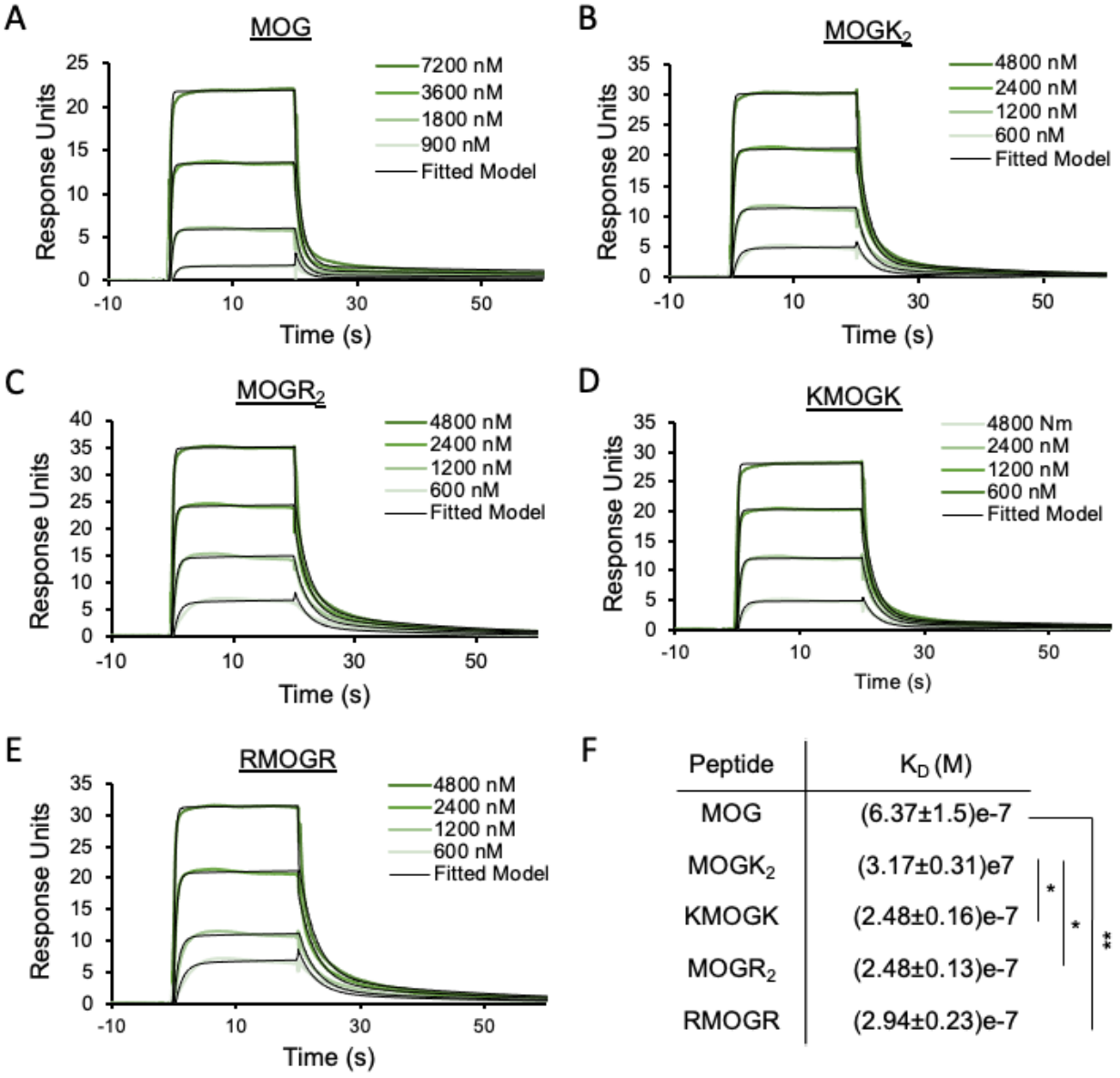

Figure 29. Representative kinetic curves from one surface plasmon resonance experiment are shown for A) MOG, B) $MOGK_2$, C) $MOGR_2$, D) KMOGK, and E) RMOGR. F) Average K_D values (n=3) calculated for binding between MOG peptides and GpG. Statistics were analyzed by One way ANOVA with Tukey post-test to correct for multiple comparisons. *p<0.05, **p<0.01

(**Fig. 29D**), and RMOGR (**Fig. 29E**). MOG peptides were flowed over a sensor chip coated with GpG to measure the association and dissociation rates between peptides and GpG. The kinetic binding curves were then fitted to a two-state binding model and the dissociation rate constants (K_D) between MOG peptides and GpG were calculated. A two state binding model was chosen with the expectation that the peptide-oligonucleotide complex is formed after an initial binding event, followed by a subsequent solvent exclusion-like step to readjust to an entropically favorable conformation.[144] This two-state binding event could explain why a secondary conformation was observed in **Figure 24**.

When anchoring MOG with either arginine or lysine, K_D values decreased significantly compared to just the native MOG peptide (**Fig. 29F**). Consistent with previous results, this observation indicated that the binding affinity between MOG and GpG increased when MOG exhibited a more positive charge. Based on the simulation results, native MOG peptide likely did not form as many electrostatic interactions with GpG as MOG peptide anchored with arginine or lysine. When comparing $MOGK_2$ to $MOGR_2$, K_D values were significantly lower when MOG was anchored with arginine residues rather than lysine residues. This is again consistent with previous results. Since both $MOGK_2$ and $MOGR_2$ have the same overall charge, this finding suggests that additional factors impacted the molecular interactions between MOG peptides and GpG. Our simulation data revealed that arginine residues facilitate formation of more hydrogen bonding and salt bridges between MOG and GpG than lysine residues, which predicts the experimental result.

Intriguingly, KMOGK had a significantly lower K_D value than $MOGK_2$. These data indicate that compared to $MOGK_2$, increasing charge distribution by anchoring MOG peptide with lysine on both the N and C terminus increased binding affinity with GpG. This result is in line with our initial hypothesis. The simulation data indicated no differences in electrostatic interactions

between $MOGK_2$ and KMOGK, but KMOGK did form slightly more total contacts than $MOGK_2$ (**Fig. 25**). The contact heatmaps also indicated that KMOGK formed a broader range of contacts with GpG than $MOGK_2$ (**Fig. 26**). Taken together, these data indicate that when considering peptides of the same charge and amino acid composition, increasing charge distribution may impact other types of interactions that were not identified in our analysis. This trend may also be different when distributing charge with lysine residues and arginine residues. When measured by surface plasmon resonance, the binding affinity of RMOGR decreased compared to $MOGR_2$ (**Fig. 29F**). It may be that because arginine forms more electrostatic interactions with GpG than lysine, concentrating arginines together could confer a higher binding affinity compared to distributing the arginines. This hypothesis needs to be confirmed by completing a REMD simulation of RMOGR and GpG.

4.4) Concluding remarks

REMD simulations are a powerful tool to inform design of self-assembling immunotherapies with specific biophysical properties, such as higher or lower binding affinity. The ability to understand and control these design levers will enable innovative methods of programming immune responses to combat diseases such as cancer and autoimmunity. Our studies revealed a stark contrast in molecular interactions when anchoring MOG peptides with different total number (2 vs. 9) and type (lysine vs. arginine) of cationic residues. Specifically, we revealed that MOG peptides with higher total charge or anchored with arginine residues formed more electrostatic interactions with GpG than MOG peptides with lower total charge or anchored with lysine residues, respectively. These data explain experimental measurements discussed in Chapter 3 and 4 that indicate MOG peptides with higher total charge or anchored with arginine residues have a higher binding affinity with GpG than MOG peptides with lower total charge or anchored

with lysine residues, respectively. Additional simulations with completely different peptide antigens would be useful in determining how the insights discussed here translate to different self-assembly systems. If the trends observed in our studies translate to other peptide/oligonucleotide self-assembly systems, we can leverage molecular dynamics as a screening tool for designing modular, self-assembling immunotherapies with specifically designed biophysical characteristics. Since REMD methods are resource intensive, it is likely a different simulation method, like coarse graining, would be used for this purpose in the future. With continued collaboration between immunoengineers and computational researchers, new and more efficient methodologies can be developed to help build the next generation of immunotherapies.

CHAPTER 5: CONCLUSIONS AND FUTURE WORK

5.1) Outlook

The research completed in this dissertation highlights how biophysical design of immunotherapies can directly impact immune outcomes. This work revealed for the first time that immune signals can be self-assembled into immunotherapies with designed biophysical properties, such as higher or lower binding affinity, to influence immune cell signaling and function. Additionally, our work demonstrated how molecular dynamics can be utilized as a tool to understand and identify how design parameters of immune cues, such as total charge and anchored amino acid residue, will influence the biophysical properties of self-assembled immunotherapies. These developments also led to several questions for further exploration, including how design of peptide antigens impacts loading of antigen into MHC-II, and what computational methods may be better suited for future study of how design parameters impact the biophysical properties of immunotherapies. Several of these areas are presented below.

5.2) Exploring loading of MOG peptides into MHC and recognition of MOG by T cells

Loading of peptides into MHC-II complexes is restricted by length; it is estimated that only peptides 13-25 amino acids long can fit into the binding groove of MHC-II.[7] Additionally, MHC-II complexes have open binding grooves, which allows the N-terminus of peptides loaded into MHC-II to protrude out and even bind with different affinities. This indicates that anchoring antigen with amino acids on either terminus may impact how antigen is loaded into MHC-II. This could lead to loading of antigen into MHC-II with lower affinity, which has been proposed as a mechanism for induction of autoimmune reactions in type 1 diabetes.[152,153] Thus, it is important to study if the MOG peptides can be loaded into MHC-II and how loading changes as a function of the structure of the peptide.

Previous studies described in Chapter 3 observed differences in T cell proliferation and polarization towards regulatory phenotypes as a function of the MOG peptide sequence. As discussed at the end of Chapter 3, the ability of peptide antigens to be loaded into MHC complexes depend on physical properties such as the geometry, charge distribution, and hydrophobicity of both the binding groove and the peptide, as well as the length of the peptide.[6,7] Any changes in this regard could impact the ability of T cells to recognize and respond to antigen within MHC. Thus, further elucidation of the connections between design of peptide antigens and loading of antigen into MHC complexes will be a key consideration in the development of effective antigen-specific therapies. I hypothesize that increased T cell polarization towards regulatory phenotypes was at least in part linked to T cells binding MOG in MHC complexes with low affinity. To test this hypothesis, we can study if the MOG sequences can be loaded into MHC-II complexes and how T cells respond to MOG presented by dendritic cells.

We can use surface plasmon resonance to study the interactions between the different MOG sequences and MHC-II. To develop this assay, first we can anchor biotinylated MHC-II on the surface of a gold sensor chip via biotin/neutravidin binding. Then, we can flow each MOG peptide sequence in order to measure the kinetic association and dissociation curves between MOG in solution and MHC-II that is anchored to the chip. As MOG associates with MHC-II, surface plasmon resonance can be used to measure the rate of association and dissociation and subsequently, the dissociation constant (K_D) can be calculated. We can then compare the different peptide sequences to unmodified MOG to determine if anchoring MOG with cationic amino acids hinders loading of MOG into MHC-II. This assay will 1) verify whether or not the different MOG sequences can bind to MHC-II without any modifications during antigen processing and 2) if they do bind to MHC-II, do the peptides bind to MHC-II with different affinities.

To assess how design of MOG impacts T cell response, we can isolate dendritic cells from the spleens of mice and treat the dendritic cells with CpG, CpG + GpG, CpG + soluble MOG peptides, or CpG + MOG/GpG complexes for 24 hours to allow for processing of signals and presentation of MOG by DCs. After 24 hours, we can isolate MOG-specific CD4 T cells from the spleens of mice, stain them with a proliferation dye (CFSE), and co-culture the T cells with the treated dendritic cells for 72 hours to allow time for T cells to bind MOG on the surface of DCs and respond accordingly. After 72 hours, we can measure proliferation and phenotype of T cells by flow cytometry to assess activation of T cells. To quantify inflammatory phenotypes, we can stain for markers associated with T_H1 (T-bet, IFN-γ) and T_H17 (ROR-γ, IL-17). To quantify regulatory phenotypes, we can stain for markers associated with T_{REG} (CD25, FoxP3). Comparing the impact of peptide structure on T cell activation in combination with the observations from the surface plasmon resonance studies measuring association of the different peptide sequences with MHC-II will reveal how antigen structure is associated with T cell response. For example, T cells studies could confirm that T cell response is altered as a function of MOG sequence and surface plasmon resonance studies could reveal that different MOG sequences associate with MHC-II with different affinities compared to unmodified MOG. This combination of results would indicate that T cell response is altered by the affinity that MOG is bound in MHC-II, which in turn affects the affinity with which T cells bind MOG. Alternatively, T cell studies could confirm that T cell response is altered as a function of MOG structure, but surface plasmon resonance studies could reveal there are no distinct differences in the affinity MOG sequences associate with MHC-II. This combination of results may indicate that after uptake of complexes, the structure of MOG alters mechanisms during processing and presentation of antigen that alter how efficiently MOG is presented on the surface of DCs.

5.3) Exploring coarse grained modelling methods to simulate self-assembly of immune signals

Course-graining is a common technique that is useful for creating biomolecular simulations.[163,164] Compared to atomistic models that model interactions of individual atoms, course-grained models map several individual atoms to one larger unit or "interaction site" that approximates the interactions of the underlying atoms **(Fig. 30)**. In doing so, coarse-grained models focus on essential features while averaging over less important details, and thus speed up simulations by reducing the number of computations per timestep. Coarse-grained models are composed of two main mapping components. The system mapping specifies the number, type, and connectivity of the interaction sites that describe the system. Interactions sites are connected with coarse-grained bonds that are based on the chemical bonds connecting the atomic groups. The coordinate mapping describes the configuration of the coarse-grained model as a function of the configuration of the underlying atomistic model. Using a coarse-grained modeling approach to simulate electrostatic self-assembly of charged immune signals could provide valuable insight into the governing biophysical parameters that are required to synthesize self-assembled immunotherapies. While this approach limits the level of detail in modeling the molecular interactions compared to atomistic models, it is well suited to study parameters that can be described without atomistic levels of detail, such as charge balance.

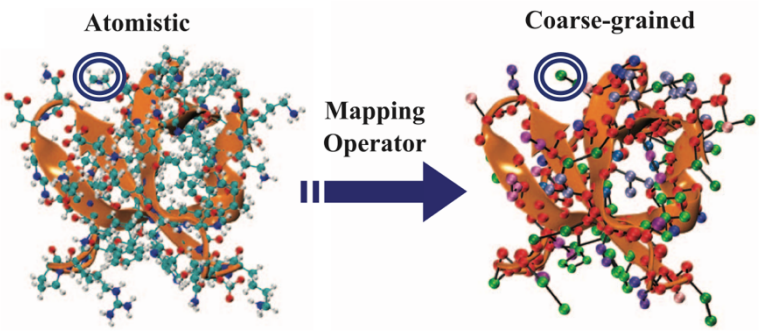

Figure 30. Example of an atomistic structure mapping to a coarse-grained structure. (ref. 163)

We can use coarse gained methods to develop a computational model to model the self-assembly of MOG and GpG in aqueous solution into complexes. In doing so, we can gain insight into general principles of how biophysical design parameters impact self-assembly that can't be gleaned from modeling the self-assembly of a single peptide and oligonucleotide. To increase computational efficiency, we can use a coarse-grained modeling approach to represent groups of atoms with properties of interest as one "interaction site." To model the structure of MOG peptide sequences, we can build off of a peptide model previously described by Dr. Matysiak's group.[165] This model was built off of a previous model that generated peptide secondary structures based on primary amino acid sequences without any built-in bias.[166,167] The course grained peptide would consist of three types of beads: charged (+/-), hydrophobic (H), or polar (P) mapped to an atomistic amino acid sequence (**Fig. 31**).[165] Each amino acid's backbone can be mapped into a single backbone bead (BB) with dummy positive/negative charges. These charges will allow interaction with the environment through electrostatic interactions and within the structure itself to generate induced-dipole effects that allow for formation of secondary structures.[166] Charged residues (e.g., R, K, E) can be represented as two side chain beads (S1/S2), one hydrophobic and one charged,

and uncharged side chains will be represented as one or two hydrophobic beads. Parameters to describe beads that can form hydrogen bonds will also be defined.

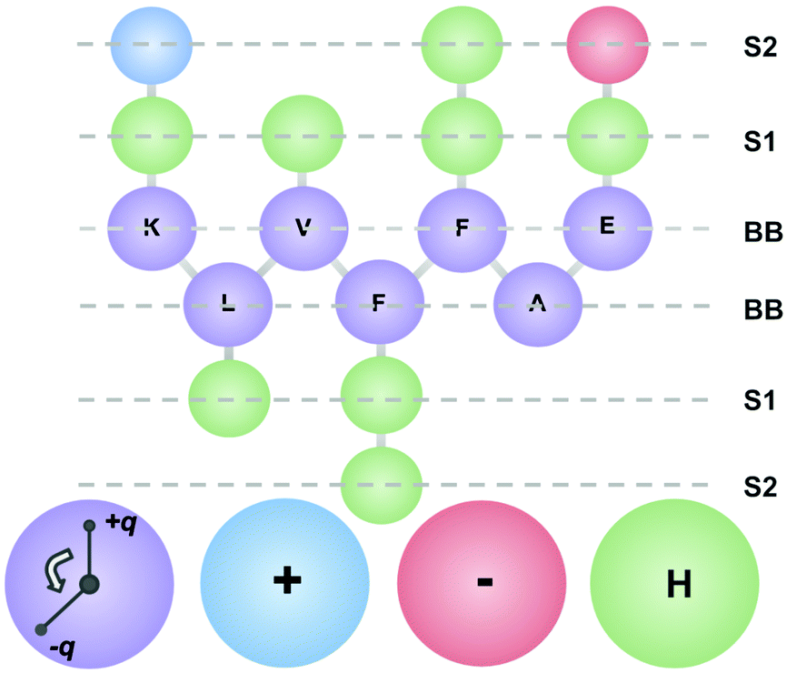

Figure 31. Example schematic of peptide coarse-grained model from ref. 165.

To model the sequence of GpG, we can utilize a Martini coarse grained approach that has been extended to modeling nucleotide sequences.[168] Martini models map roughly four non-hydrogen atoms to one coarse grained bead and have a limited number of beads and interaction types.[169] Each bead describes one or more chemical building blocks and mimics their properties, thus making this model transferrable to different systems and compatible with each other, including the peptide model described above. Nucleotides in GpG would be modeled to six or seven coarse grained beads (**Fig. 32**).[168] In the nucleotide backbone, the phosphate would be modeled to one bead and the sugar will be modeled to two beads. The rings of cytosine and thymine would be modeled to three beads and the rings of adenine and guanine would be modeled to four beads. Parameters would also be defined to describe beads that are charged and beads that can

form hydrogen bonds. We can also include water molecules in the simulation and model four water molecules to one bead using the Martini approach.

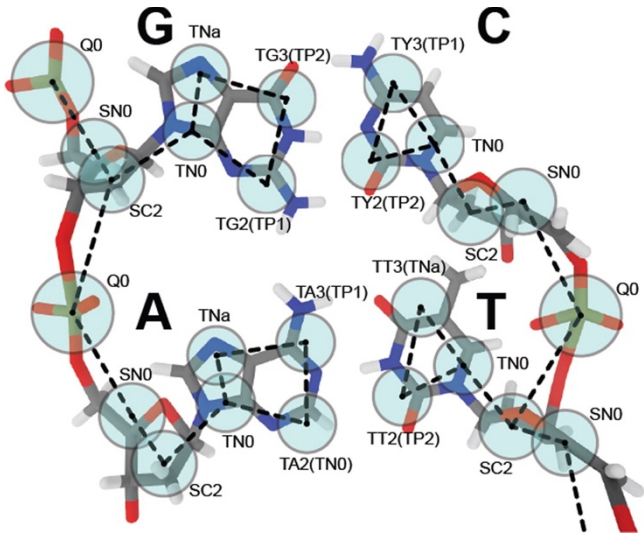

Figure 32. Example schematic of DNA coarse grained model from ref. 168. Letter + number codes identify different beads of each nucleotide.

The molecular simulations would be performed on the GROMACs simulation package. Parameters related to self-assembly, such as timesteps, non-bonding interactions, electric permittivity, etc. can be set and tested based on previous methods.[165,168] The simulations can be developed to study formation of complexes as a function of many formulation conditions, including MOG peptide design, concentration, charge balance in solution, pH, and salinity. Completing these simulations can reveal a wealth of insights that inform how to engineer self-assembled immunotherapies with specifically designed biophysical parameters.

APPENDIX: CONTRIBUTIONS AND FUNDING

First Author Publications

1. **Eugene Froimchuk**, Abhilash Sahoo, Silvina Matysiak, Christopher M. Jewell. "Integrating molecular dynamics simulations to enable rational assembly of immune signals for immunotherapy." (In prep)

2. **Eugene Froimchuk**, Robert S. Oakes, Senta M. Kapnick, Alexis A. Yanes, Christopher M. Jewell. "Biophysical properties of self-assembled immune signals impact signal processing and the nature of regulatory immune function." 2021. *Nano Letters*. 21(9): 3762-3771.

3. **Eugene Froimchuk**, Sean T. Carey, Camilla Edwards, Christopher M. Jewell. "Self-assembly as a molecular strategy to improve immunotherapy." 2020. *Accounts of Chemical Research*. *53*: 2534–2545.

Contributing Author Publications

4. Emily A. Gosselin, Senta M. Kapnick, Shannon J. Tsai, Robert S. Oakes, Zahra A. Habibabady, Sean T. Carey, **Eugene Froimchuk**, Marian A. Ackun-Farmmer, Haleigh B. Eppler, Maeesha Noshin, Lisa H. Tostanoski, Sheneil K. Black, Xiangbin Zeng, Alexis A. Yanes, Agnes Azimzedah, Richard Pierson III, Jonathan S. Bromberg, Christopher M. Jewell. "A single-dose, tolerizing vaccine induces antigen-specific regulatory T cells and durable remission in mouse models of Multiple sclerosis with favorable safety profiles in non-human primates." (In prep).

5. Michelle L. Bookstaver, Qin Zeng, Robert S. Oakes, Senta M. Kapnick, Vikas Saxena, Camilla Edwards, Nishedhya Venkataraman, Sheneil K. Black, Xiangbin Zeng, **Eugene Froimchuk**, Thomas Gebhardt, Jonathan S. Bromberg, Christopher M. Jewell."Self-assembly of immune signals to program innate immunity through rational adjuvant design." *Advanced Science*. 2022. 2202393.

6. Robert S. Oakes, Lisa H. Tostanoski, Senta M. Kapnick, **Eugene Froimchuk**, Sheneil K. Black, Xiangbin Zeng, Christopher M. Jewell. "Exploiting rational assembly to map distinct roles of regulatory cues during autoimmune therapy." 2021. *ACS Nano*. 15: 4305-4320.

7. Robert Oakes, **Eugene Froimchuk**, Christopher Jewell. "Engineering biomaterials to direct innate immunity." 2019. *Advanced Therapeutics*. 2(6).

Conference Presentations

1. **Eugene Froimchuk**, Robert Oakes, Senta Kapnick, Alexis Yanes, Christopher Jewell. Oral: Biophysical Properties of Self-Assembled Immune Signals Influence Regulatory Processing and Function. Materials Research Society. Boston, MA. December 2021.

2. **Eugene Froimchuk**, Robert Oakes, Senta Kapnick, Alexis Yanes, Christopher Jewell. Oral: Biophysical Properties of Self-Assembled Immune Signals Influence Regulatory Processing and Function. Biomedical Engineering Society. Orlando, FL. October 2021.

3. **Eugene Froimchuk**, Christopher Jewell. Poster: "Engineering delivery of immune signals to direct antigen-specific T cell differentiation for autoimmune disease therapies." Keystone Symposia – Emerging Cellular Therapies: Cancer and Beyond. Banff, AB, Canada. February 2020.

4. **Eugene Froimchuk**, Christopher Jewell. Poster: "Tuning self-assembled nanoparticle composition to optimize therapeutic efficacy in autoimmune disease." American Chemical Society National Conference. Orlando, FL. April 2019.

Fellowships

1. National Science Foundation Graduate Research Fellowship (#DGE1840340)

2. A. James Clark School Doctoral Fellowship

BIBLIOGRAPHY

1. Fröhlich E. The role of surface charge in cellular uptake and cytotoxicity of medical nanoparticles. *Int J Nanomed*. 2012;7:5577-91. doi:10.2147/ijn.s36111

2. Wen Y, Waltman A, Han H, Collier JH. Switching the Immunogenicity of Peptide Assemblies Using Surface Properties. *ACS Nano*. 10/25/2016 2016;10(10):9274-9286. doi:10.1021/acsnano.6b03409

3. Singha S, Shao K, Yang Y, et al. Peptide-MHC-based nanomedicines for autoimmunity function as T-cell receptor microclustering devices. *Nat Nanotechnol*. Jul 2017;12(7):701-710. doi:10.1038/nnano.2017.56

4. Hess KL, Oh E, Tostanoski LH, et al. Engineering Immunological Tolerance Using Quantum Dots to Tune the Density of Self-Antigen Display. *Adv Funct Mater*. Jun 13 2017;27(22):1700290. doi:10.1002/adfm.201700290

5. Jain A, Pasare C. Innate Control of Adaptive Immunity: Beyond the Three-Signal Paradigm. *J Immunol*. 05/15/2017 2017;198(10):3791-3800. doi:10.4049/jimmunol.1602000

6. Wieczorek M, Abualrous ET, Sticht J, et al. Major Histocompatibility Complex (MHC) Class I and MHC Class II Proteins: Conformational Plasticity in Antigen Presentation. Review. *Front Immunol*. 2017-March-17 2017;8(292)doi:10.3389/fimmu.2017.00292

7. Chicz RM, Urban RG, Lane WS, et al. Predominant naturally processed peptides bound to HLA-DR1 are derived from MHC-related molecules and are heterogeneous in size. *Nature*. 1992/08/01 1992;358(6389):764-768. doi:10.1038/358764a0

8. Oakes RS, Froimchuk E, Jewell CM. Engineering Biomaterials to Direct Innate Immunity. *Adv Ther (Weinheim, Ger)*. Jun 2019;2(6):pii: 1800157. doi:10.1002/adtp.201800157

9. Seong SY, Matzinger P. Hydrophobicity: An Ancient Damage-Associated Molecular Pattern That Initiates Innate Immune Responses. *Nat Rev Immunol*. 2004 Jun 2004;4(6):469-78. doi:10.1038/nri1372

10. Morris GP, Allen PM. How the TCR balances sensitivity and specificity for the recognition of self and pathogens. *Nat Immunol*. 01/19/2012 2012;13(2):121-8. doi:10.1038/ni.2190

11. Stone JD, Chervin AS, Kranz DM. T-cell receptor binding affinities and kinetics: impact on T-cell activity and specificity. *Immunology*. 2009 Feb 2009;126(2):165-76. doi:10.1111/j.1365-2567.2008.03015.x

12. Dintzis H, M., Dintzis R, Z., Vogelstein B. Molecular determinants of immunogenicity: the immunon model of immune response. *Proceedings of the National Academy of Sciences of the United States of America*. 1976 Oct 1976;73(10):3671-5. doi:10.1073/pnas.73.10.3671

13. Germain R, N. T-cell signaling: the importance of receptor clustering. *Curr Biol*. 10/01/1997 1997;7(10):640-644. doi:10.1016/s0960-9822(06)00323-x

14. Wibroe PP, Anselmo AC, Nilsson PH, et al. Bypassing adverse injection reactions to nanoparticles through shape modification and attachment to erythrocytes. *Nat Nanotechnol*. Jul 2017;12(6):589-594. doi:10.1038/nnano.2017.47

15. Chen X, Yan Y, Mullner M, et al. Shape-Dependent Activation of Cytokine Secretion by Polymer Capsules in Human Monocyte-Derived Macrophages. *Biomacromolecules*. Mar 14 2016;17(3):1205-12. doi:10.1021/acs.biomac.6b00027

16.\ Meyer RA, Sunshine JC, Perica K, et al. Biodegradable nanoellipsoidal artificial antigen presenting cells for antigen specific T-cell activation. *Small*. 2015 Apr 2015;11(13):1519-25. doi:10.1002/smll.201402369

17. Sunshine JC, Perica K, Schneck JP, Green JJ. Particle shape dependence of CD8+ T cell activation by artificial antigen presenting cells. *Biomaterials*. Jan 2014;35(1):269-277. doi:10.1016/j.biomaterials.2013.09.050

18. Hardy CL, Lemasurier JS, Mohamud R, et al. Differential uptake of nanoparticles and microparticles by pulmonary APC subsets induces discrete immunological imprints. *J Immunol*. 11/15/2013 2013;191(10):5278-90. doi:10.4049/jimmunol.1203131

19. Kumar S, Anselmo AC, Banerjee A, Zakrewsky M, Mitragotri S. Shape and size-dependent immune response to antigen-carrying nanoparticles. *J Controlled Release*. Dec 28 2015;220(Pt A):141-148. doi:10.1016/j.jconrel.2015.09.069

20. Pompano RR, Chen J, Verbus EA, et al. Titrating T-cell Epitopes Within Self-Assembled Vaccines Optimizes CD4+ Helper T Cell and Antibody Outputs. *Adv Healthcare Mater*. 2014 Nov 2014;3(11):1898-908. doi:10.1002/adhm.201400137

21. Moyano DF, Goldsmith M, Solfiell D, J., et al. Nanoparticle hydrophobicity dictates immune response. *J Am Chem Soc*. Mar 7 2012;134(9):3965-7. doi:10.1021/ja2108905

22. Miura R, Sawada SI, Mukai SA, Sasaki Y, Akiyoshi K. Antigen Delivery to Antigen-Presenting Cells for Adaptive Immune Response by Self-Assembled Anionic Polysaccharide Nanogel Vaccines. *Biomacromolecules*. Feb 10 2020;21(2):621-629. doi:10.1021/acs.biomac.9b01351

23. Rui Y, Eppler HB, Yanes AA, Jewell CM. Tissue-Targeted Drug Delivery Strategies to Promote Antigen-Specific Immune Tolerance. *Advanced healthcare materials*. 11/23/2022 2022;doi:10.1002/adhm.202202238

24. Froimchuk E, Carey ST, Edwards C, Jewell CM. Self-Assembly as a Molecular Strategy to Improve Immunotherapy. *Acc Chem Res*. 2020/10/19 2020;53(11):2534-45. doi:10.1021/acs.accounts.0c00438

25. Bookstaver ML, Tsai SJ, Bromberg JS, Jewell CM. Improving Vaccine and Immunotherapy Design Using Biomaterials. *Trends Immunol*. Feb 2018;39(2):135-150. doi:10.1016/j.it.2017.10.002

26. Weiner LM, Dhodapkar MV, Ferrone S. Monoclonal Antibodies for Cancer Immunotherapy. *Lancet*. Mar 21 2009;373(9668):1033-40. doi:10.1016/s0140-6736(09)60251-8

27. Darvin P, Toor SM, Sasidharan Nair V, Elkord E. Immune checkpoint inhibitors: recent progress and potential biomarkers. *Exp Mol Med*. Dec 13 2018;50(12):1-11. doi:10.1038/s12276-018-0191-1

28. L S, N C, M P. Toxicities associated with checkpoint inhibitors-an overview. *Rheumatology (Oxford, England)*. 12/01/2019 2019;58(Suppl 7)doi:10.1093/rheumatology/kez418

29. P F, LA P, J C, et al. Immunotoxicity from checkpoint inhibitor therapy: clinical features and underlying mechanisms. *Immunology*. 2020 Feb 2020;159(2):167-177. doi:10.1111/imm.13141

30. Rosenblum MD, Gratz IK, Paw JS, Abbas AK. Treating Human Autoimmunity: Current Practice and Future Prospects. *Sci Transl Med*. Mar 14 2012;4(125):125sr1. doi:10.1126/scitranslmed.3003504

31. FDA approves new drug to treat multiple sclerosis. Wed, 03/29/2017 - 04:36, 2017. https://www.fda.gov/news-events/press-announcements/fda-approves-new-drug-treat-multiple-sclerosis

32. FDA U. FDA Approves First Drug That Can Delay Onset of Type 1 Diabetes | FDA. @US_FDA. Updated Thu, 11/17/2022 - 17:00. https://www.fda.gov/news-events/press-announcements/fda-approves-first-drug-can-delay-onset-type-1-diabetes

33. Eppler HB, Jewell CM. Biomaterials as Tools to Decode Immunity. *Adv Mater*. 2020 Apr 2019;32(13):1903367. doi:10.1002/adma.201903367

34. Lin AY, Almeida JP, Bear A, et al. Gold nanoparticle delivery of modified CpG stimulates macrophages and inhibits tumor growth for enhanced immunotherapy. *PLoS One*. 2013;8(5):e63550. doi:10.1371/journal.pone.0063550

35. Chen N, Wei M, Sun Y, et al. Self-assembly of poly-adenine-tailed CpG oligonucleotide-gold nanoparticle nanoconjugates with immunostimulatory activity. *Small*. Jan 29 2014;10(2):368-75. doi:10.1002/smll.201300903

36. Lynn GM, Sedlik C, Baharom F, et al. Peptide-TLR-7/8a Conjugate Vaccines Chemically Programmed for Nanoparticle Self-Assembly Enhance CD8 T-cell Immunity to Tumor Antigens. *Nat Biotechnol*. 2020 Mar 2020;38(3):320-332. doi:10.1038/s41587-019-0390-x

37. Getts DR, McCarthy DP, Miller SD. Exploiting apoptosis for therapeutic tolerance induction. *J Immunol*. Dec 1 2013;191(11):5341-6. doi:10.4049/jimmunol.1302070

38. Smith CE, Miller SD. Multi-Peptide Coupled-Cell Tolerance Ameliorates Ongoing Relapsing EAE Associated with Multiple Pathogenic Autoreactivities. *J Autoimmun*. Dec 2006;27(4):218-31. doi:10.1016/j.jaut.2006.12.002

39. Turley DM, Miller SD. Peripheral tolerance induction using ethylenecarbodiimide-fixed APCs uses both direct and indirect mechanisms of antigen presentation for prevention of experimental autoimmune encephalomyelitis. *J Immunol*. Feb 15 2007;178(4):2212-20.

40. Pishesha N, Bilate AM, Wibowo MC, et al. Engineered erythrocytes covalently linked to antigenic peptides can protect against autoimmune disease. *Proc Natl Acad Sci U S A*. Mar 21 2017;114(12):3157-3162. doi:10.1073/pnas.1701746114

41. Getts DR, Turley DM, Smith CE, et al. Tolerance induced by apoptotic antigen-coupled leukocytes is induced by PD-L1+ and IL-10-producing splenic macrophages and maintained by T regulatory cells. *J Immunol*. Sep 1 2011;187(5):2405-17. doi:10.4049/jimmunol.1004175

42. Lutterotti A, Yousef S, Sputtek A, et al. Antigen-specific tolerance by autologous myelin peptide-coupled cells: a phase 1 trial in multiple sclerosis. *Sci Transl Med*. Jun 5 2013;5(188):188ra75. doi:10.1126/scitranslmed.3006168

43. Prasad S, Kohm AP, McMahon JS, Luo X, Miller SD. Pathogenesis of NOD diabetes is initiated by reactivity to the insulin B chain 9-23 epitope and involves functional epitope spreading. *J Autoimmun*. Dec 2012;39(4):347-53. doi:10.1016/j.jaut.2012.04.005

44. Grimm AJ, Kontos S, Diaceri G, Quaglia-Thermes X, Hubbell JA. Memory of tolerance and induction of regulatory T cells by erythrocyte-targeted antigens. *Sci Rep*. 2015;5doi:10.1038/srep15907

45. Kontos S, Kourtis IC, Dane KY, Hubbell JA. Engineering antigens for in situ erythrocyte binding induces T-cell deletion. *Proc Natl Acad Sci U S A*. Jan 2 2013;110(1):E60-8. doi:10.1073/pnas.1216353110

46. Getts DR, Martin AJ, McCarthy DP, et al. Microparticles bearing encephalitogenic peptides induce T-cell tolerance and ameliorate experimental autoimmune encephalomyelitis. *Nat Biotechnol*. Dec 2012;30(12):1217-24. doi:10.1038/nbt.2434

47. Kuo R, Saito E, Miller SD, Shea LD. Peptide-Conjugated Nanoparticles Reduce Positive Co-stimulatory Expression and T Cell Activity to Induce Tolerance. *Molecular Therapy*. Jul 5 2017;25(7):1676-1685. doi:10.1016/j.ymthe.2017.03.032

48. Hunter Z, McCarthy DP, Yap WT, et al. A biodegradable nanoparticle platform for the induction of antigen-specific immune tolerance for treatment of autoimmune disease. *ACS Nano*. Mar 25 2014;8(3):2148-60. doi:10.1021/nn405033r

49. McCarthy DP, Yap JW, Harp CT, et al. An antigen-encapsulating nanoparticle platform for TH1/17 immune tolerance therapy. *Nanomedicine*. Jan 2017;13(1):191-200. doi:10.1016/j.nano.2016.09.007

50. Chen Y, Wu J, Wang J, et al. Targeted delivery of antigen to intestinal dendritic cells induces oral tolerance and prevents autoimmune diabetes in NOD mice. *Diabetologia*. Jun 2018;61(6):1384-1396. doi:10.1007/s00125-018-4593-3

51. Prasad S, Neef T, Xu D, et al. Tolerogenic Ag-PLG nanoparticles induce tregs to suppress activated diabetogenic CD4 and CD8 T cells. *J Autoimmun*. May 2018;89:112-124. doi:10.1016/j.jaut.2017.12.010

52. Pearson RM, Casey LM, Hughes KR, et al. Controlled Delivery of Single or Multiple Antigens in Tolerogenic Nanoparticles Using Peptide-Polymer Bioconjugates. *Mol Ther*. Jul 5 2017;25(7):1655-1664. doi:10.1016/j.ymthe.2017.04.015

53. Cappellano G, Woldetsadik AD, Orilieri E, et al. Subcutaneous inverse vaccination with PLGA particles loaded with a MOG peptide and IL-10 decreases the severity of experimental autoimmune encephalomyelitis. *Vaccine*. Sep 29 2014;32(43):5681-9. doi:10.1016/j.vaccine.2014.08.016

54. Yeste A, Nadeau M, Burns EJ, Weiner HL, Quintana FJ. Nanoparticle-mediated codelivery of myelin antigen and a tolerogenic small molecule suppresses experimental autoimmune

encephalomyelitis. *Proc Natl Acad Sci U S A*. Jul 10 2012;109(28):11270-5. doi:10.1073/pnas.1120611109

55. Yeste A, Takenaka MC, Mascanfroni ID, et al. Tolerogenic nanoparticles inhibit T cell-mediated autoimmunity through SOCS2. *Sci Signal*. Jun 21 2016;9(433):ra61. doi:10.1126/scisignal.aad0612

56. Chen N, Kroger CJ, Tisch RM, Bachelder EM, Ainslie KM. Prevention of Type 1 Diabetes with Acetalated Dextran Microparticles Containing Rapamycin and Pancreatic Peptide P31. *Adv Healthc Mater*. Sep 2018;7(18):e1800341. doi:10.1002/adhm.201800341

57. Peine KJ, Guerau-de-Arellano M, Lee P, et al. Treatment of experimental autoimmune encephalomyelitis by codelivery of disease associated Peptide and dexamethasone in acetalated dextran microparticles. *Mol Pharm*. Mar 3 2014;11(3):828-35. doi:10.1021/mp4005172

58. Casey LM, Pearson RM, Hughes KR, et al. Conjugation of Transforming Growth Factor Beta to Antigen-Loaded Poly(lactide- co-glycolide) Nanoparticles Enhances Efficiency of Antigen-Specific Tolerance. *Bioconjug Chem*. Mar 21 2018;29(3):813-823. doi:10.1021/acs.bioconjchem.7b00624

59. Verbeke CS, Gordo S, Schubert DA, et al. Multicomponent Injectable Hydrogels for Antigen-Specific Tolerogenic Immune Modulation. *Adv Healthc Mater*. Mar 2017;6(6)doi:10.1002/adhm.201600773

60. LaMothe RA, Kolte PN, Vo T, et al. Tolerogenic Nanoparticles Induce Antigen-Specific Regulatory T Cells and Provide Therapeutic Efficacy and Transferrable Tolerance against Experimental Autoimmune Encephalomyelitis. *Front Immunol*. 2018;9:281. doi:10.3389/fimmu.2018.00281

61. Maldonado RA, LaMothe RA, Ferrari JD, et al. Polymeric synthetic nanoparticles for the induction of antigen-specific immunological tolerance. *Proc Natl Acad Sci U S A*. Jan 13 2015;112(2):E156-65. doi:10.1073/pnas.1408686111

62. Cho JJ, Stewart JM, Drashansky TT, et al. An antigen-specific semi-therapeutic treatment with local delivery of tolerogenic factors through a dual-sized microparticle system blocks experimental autoimmune encephalomyelitis. *Biomaterials*. Oct 2017;143:79-92. doi:10.1016/j.biomaterials.2017.07.029

63. Yoon YM, Lewis JS, Carstens MR, et al. A combination hydrogel microparticle-based vaccine prevents type 1 diabetes in non-obese diabetic mice. *Sci Rep*. Aug 17 2015;5:13155. doi:10.1038/srep13155

64. Lewis JS, Roche C, Zhang Y, et al. Combinatorial delivery of immunosuppressive factors to dendritic cells using dual-sized microspheres. *J Mater Chem B Mater Biol Med*. May 7 2014;2(17):2562-2574. doi:10.1039/c3tb21460e

65. Roberts RA, Eitas TK, Byrne JD, et al. Towards programming immune tolerance through geometric manipulation of phosphatidylserine. *Biomaterials*. Dec 2015;72:1-10. doi:10.1016/j.biomaterials.2015.08.040

66. Gammon JM, Tostanoski LH, Adapa AR, Chiu YC, Jewell CM. Controlled delivery of a metabolic modulator promotes regulatory T cells and restrains autoimmunity. *J Control Release*. Jul 28 2015;210:169-78. doi:10.1016/j.jconrel.2015.05.277

67. Chittasupho C, Sestak J, Shannon L, Siahaan TJ, Vines CM, Berkland C. Hyaluronic acid graft polymers displaying peptide antigen modulate dendritic cell response in vitro. *Mol Pharm*. Jan 6 2014;11(1):367-73. doi:10.1021/mp4003909

68. Hartwell BL, Smalter Hall A, Swafford D, et al. Molecular Dynamics of Multivalent Soluble Antigen Arrays Support a Two-Signal Co-delivery Mechanism in the Treatment of Experimental Autoimmune Encephalomyelitis. *Mol Pharm*. Feb 1 2016;13(2):330-43. doi:10.1021/acs.molpharmaceut.5b00825

69. Northrup L, Sestak JO, Sullivan BP, et al. Co-delivery of autoantigen and b7 pathway modulators suppresses experimental autoimmune encephalomyelitis. *Aaps j*. Nov 2014;16(6):1204-13. doi:10.1208/s12248-014-9671-y

70. Tostanoski LH, Chiu YC, Gammon JM, et al. Reprogramming the Local Lymph Node Microenvironment Promotes Tolerance that Is Systemic and Antigen Specific. *Cell Rep*. Sep 13 2016;16(11):2940-2952. doi:10.1016/j.celrep.2016.08.033

71. Tostanoski LH, Chiu YC, Andorko JI, et al. Design of Polyelectrolyte Multilayers to Promote Immunological Tolerance. *ACS Nano*. Sep 7 2016;doi:10.1021/acsnano.6b04001

72. Hess KL, Andorko JI, Tostanoski LH, Jewell CM. Polyplexes assembled from self-peptides and regulatory nucleic acids blunt toll-like receptor signaling to combat autoimmunity. *Biomaterials*. Feb 2017;118:51-62. doi:10.1016/j.biomaterials.2016.11.052

73. Pihl M, Akerman L, Axelsson S, et al. Regulatory T cell phenotype and function 4 years after GAD-alum treatment in children with type 1 diabetes. *Clinical and experimental immunology*. 2013 Jun 2013;172(3):394-402. doi:10.1111/cei.12078

74. Wherrett DK, Bundy B, Becker DJ, et al. Antigen-based therapy with glutamic acid decarboxylase (GAD) vaccine in patients with recent-onset type 1 diabetes: a randomised double-blind trial. *Lancet*. Jul 23 2011;378(9788):319-27. doi:10.1016/s0140-6736(11)60895-7

75. Ludvigsson J, Faresjö M, Hjorth M, et al. GAD treatment and insulin secretion in recent-onset type 1 diabetes. *N Engl J Med*. 10/30/2008 2008;359(18)doi:10.1056/NEJMoa0804328

76. Riley RS, June CH, Langer R, Mitchell MJ. Delivery technologies for cancer immunotherapy. *Nat Rev Drug Discovery*. Mar 2019;18(3):175-96. doi:10.1038/s41573-018-0006-z

77. Andorko JI, Hess KL, Pineault KG, Jewell CM. Intrinsic immunogenicity of rapidly-degradable polymers evolves during degradation. *Acta Biomater*. Mar 1 2016;32:24-34. doi:10.1016/j.actbio.2015.12.026

78. Dold NM, Zeng Q, Zeng X, Jewell CM. A poly(beta-amino ester) activates macrophages independent of NF-kappaB signaling. *Acta Biomater*. Mar 1 2018;68:168-177. doi:10.1016/j.actbio.2017.12.040

79. Collier JH, Messersmith PB. Enzymatic Modification of Self-Assembled Peptide Structures With Tissue Transglutaminase. *Bioconjugate Chem*. Jul-Aug 2003 2003;14(4):748-755. doi:10.1021/bc034017t

80. Rudra JS, Tian YF, Jung JP, Collier JH. A Self-Assembling Peptide Acting as an Immune Adjuvant. *Proc Natl Acad Sci U S A*. 01/12/2010 2010;107(2):622-7. doi:10.1073/pnas.0912124107

81. Huang ZH, Shi L, Ma JW, et al. A Totally Synthetic, Self-Assembling, Adjuvant-Free MUC1 Glycopeptide Vaccine for Cancer Therapy. *J Am Chem Soc*. 05/30/2012 2012;134(21):8730-3. doi:10.1021/ja211725s

82. Rudra JS, Sun T, Bird KC, et al. Modulating Adaptive Immune Responses to Peptide Self-Assemblies. *ACS Nano*. 02/28/2012 2012;6(2):1557-64. doi:10.1021/nn204530r

83. Chen J, Pompano RR, Santiago FW, et al. The Use of Self-Adjuvanting Nanofiber Vaccines to Elicit High-Affinity B Cell Responses to Peptide Antigens Without Inflammation. *Biomaterials*. 2013 Nov 2013;34(34):8776-85. doi:10.1016/j.biomaterials.2013.07.063

84. Chesson CB, Huelsmann EJ, Lacek AT, et al. Antigenic Peptide Nanofibers Elicit Adjuvant-Free $CD8^+$ T Cell Responses. *Vaccine*. 02/26/2014 2014;32(10):1174-80. doi:10.1016/j.vaccine.2013.11.047

85. Wu Y, Norberg PK, Reap EA, et al. A Supramolecular Vaccine Platform Based on alpha-Helical Peptide Nanofibers. *ACS Biomater Sci Eng*. Dec 11 2017;3(12):3128-3132. doi:10.1021/acsbiomaterials.7b00561

86. Wu Y, Kelly SH, Sanchez-Perez L, Sampson JH, Collier JH. Comparative study of α-helical and β-sheet self-assembled peptide nanofiber vaccine platforms: influence of integrated T-cell epitopes. *Biomater Sci*. 2020/05/15 2020;8(12):3522. doi:10.1039/D0BM00521E

87. Purwada A, Tian YF, Huang W, et al. Self-Assembly Protein Nanogels for Safer Cancer Immunotherapy. *Adv Healthcare Mater*. 2016 Jun 2016;5(12):1413-9. doi:10.1002/adhm.201501062

88. Miura R, Sawada S, Mukai S, Sasaki Y, Akiyoshi K. Synergistic anti-tumor efficacy by combination therapy of a self-assembled nanogel vaccine with an immune checkpoint anti-PD-1 antibody. *RSC Adv*. 2020/02/25 2020;10(14):8074-79. doi:10.1039/C9RA10066K

89. Rad-Malekshahi M, Fransen MF, Krawczyk M, et al. Self-Assembling Peptide Epitopes as Novel Platform for Anticancer Vaccination. *Mol Pharmaceutics*. May 1 2017;14(5):1482-1493. doi:10.1021/acs.molpharmaceut.6b01003

90. Black M, Trent A, Kostenko Y, Lee JS, Olive C, Tirrell M. Self-assembled peptide amphiphile micelles containing a cytotoxic T-cell epitope promote a protective immune response in vivo. *Adv Mater*. Jul 24 2012;24(28):3845-9. doi:10.1002/adma.201200209

91. Da Silva CG, Camps MGM, Li T, Chan AB, Ossendorp F, Cruz LJ. Co-delivery of immunomodulators in biodegradable nanoparticles improves therapeutic efficacy of cancer vaccines. *Biomaterials*. Nov 2019;220:119417. doi:10.1016/j.biomaterials.2019.119417

92. Liu H, Moynihan KD, Zheng Y, et al. Structure-based programming of lymph-node targeting in molecular vaccines. *Nature*. Mar 27 2014;507(7493):519-22. doi:10.1038/nature12978

93. Zhu G, Lynn GM, Jacobson O, et al. Albumin/vaccine nanocomplexes that assemble in vivo for combination cancer immunotherapy. *Nat Commun*. Dec 5 2017;8(1):1954. doi:10.1038/s41467-017-02191-y

94. Appelbe OK, Moynihan KD, Flor A, Rymut N, Irvine DJ, Kron SJ. Radiation-enhanced delivery of systemically administered amphiphilic-CpG oligodeoxynucleotide. *J Controlled Release*. Nov 28 2017;266:248-255. doi:10.1016/j.jconrel.2017.09.043

95. Zhu G, Mei L, Vishwasrao HD, et al. Intertwining DNA-RNA nanocapsules loaded with tumor neoantigens as synergistic nanovaccines for cancer immunotherapy. *Nat Commun*. Nov 14 2017;8(1):1482. doi:10.1038/s41467-017-01386-7

96. Jin JO, Park H, Zhang W, et al. Modular delivery of CpG-incorporated lipid-DNA nanoparticles for spleen DC activation. *Biomaterials*. Jan 2017;115:81-89. doi:10.1016/j.biomaterials.2016.11.020

97. Jin JO, Kim H, Huh YH, Herrmann A, Kwak M. Soft matter DNA nanoparticles hybridized with CpG motifs and peptide nucleic acids enable immunological treatment of cancer. *J Controlled Release*. Dec 10 2019;315:76-84. doi:10.1016/j.jconrel.2019.09.013

98. Wei H, Zhao Z, Wang Y, Zou J, Lin O, Duan Y. One-Step Self-Assembly of Multifunctional DNA Nanohydrogels: An Enhanced and Harmless Strategy for Guiding Combined Antitumor Therapy. research-article. *ACS Appl Mater Interfaces*. November 21, 2019 2019;11(50):46479-89. doi:10.1021/acsami.9b15874

99. Wang Z, Shang Y, Tan Z, et al. A supramolecular protein chaperone for vaccine delivery. *Theranostics*. 2020;10(2):657-70. doi:10.7150/thno.39132

100. Li T, Pan S, Gao S, et al. Diselenide-Pemetrexed Assemblies for Combined Cancer Immuno-, Radio-, and Chemotherapies. *Angew Chem, Int Ed Engl*. Feb 10 2020;59(7):2700-04. doi:10.1002/anie.201914453

101. De Koker S, De Geest BG, Singh SK, et al. Polyelectrolyte microcapsules as antigen delivery vehicles to dendritic cells: uptake, processing, and cross-presentation of encapsulated antigens. *Angew Chem, Int Ed Engl*. 2009;48(45):8485-9. doi:10.1002/anie.200903769

102. De Geest BG, Willart MA, Hammad H, et al. Polymeric multilayer capsule-mediated vaccination induces protective immunity against cancer and viral infection. *ACS Nano*. Mar 27 2012;6(3):2136-49. doi:10.1021/nn205099c

103. De Geest BG, Willart MA, Lambrecht BN, et al. Surface-engineered polyelectrolyte multilayer capsules: synthetic vaccines mimicking microbial structure and function. *Angew Chem, Int Ed Engl*. Apr 16 2012;51(16):3862-6. doi:10.1002/anie.201200048

104. Zhang P, Chiu YC, Tostanoski LH, Jewell CM. Polyelectrolyte Multilayers Assembled Entirely from Immune Signals on Gold Nanoparticle Templates Promote Antigen-Specific T Cell Response. *ACS Nano*. Jun 23 2015;9(6):6465-77. doi:10.1021/acsnano.5b02153

105. Chiu YC, Gammon J, Andorko JI, Tostanoski LH, Jewell CM. Modular Vaccine Design Using Carrier-Free Capsules Assembled from Polyionic Immune Signals. *ACS Biomater Sci Eng*. Dec 14 2015;1(12):1200-5. doi:10.1021/acsbiomaterials.5b00375

106. Tostanoski LH, Chiu YC, Andorko JI, et al. Design of Polyelectrolyte Multilayers to Promote Immunological Tolerance. *ACS Nano*. Oct 25 2016;10(10):9334-45. doi:10.1021/acsnano.6b04001

107. Bookstaver ML, Zeng Q, Oakes RS, et al. Self-Assembly of Immune Signals to Program Innate Immunity through Rational Adjuvant Design. *Adv Sci (Weinh)*. 11/14/2022 2022;doi:10.1002/advs.202202393

108. Oakes RS, Tostanoski LH, Kapnick SM, et al. Exploiting Rational Assembly to Map Distinct Roles of Regulatory Cues during Autoimmune Therapy. *ACS Nano*. 03/23/2021 2021;15(3):4305-20. doi:10.1021/acsnano.0c07440

109. Chiu YC, Gammon JM, Andorko JI, Tostanoski LH, Jewell CM. Assembly and Immunological Processing of Polyelectrolyte Multilayers Composed of Antigens and Adjuvants. *ACS Appl Mater Interfaces*. Jul 27 2016;8(29):18722-31. doi:10.1021/acsami.6b06275

110. Andorko JI, Tsai SJ, Gammon JM, et al. Spatial delivery of immune cues to lymph nodes to define therapeutic outcomes in cancer vaccination. *Biomaterials science*. 08/09/2022 2022;10(16):4612-26. doi:10.1039/d2bm00403h

111. Chiu YC, Gammon JM, Andorko JI, Tostanoski LH, Jewell CM. Modular Vaccine Design Using Carrier-Free Capsules Assembled from Polyionic Immune Signals. *ACS Biomater Sci Eng*. Dec 14 2015;1(12):1200-1205. doi:10.1021/acsbiomaterials.5b00375

112. Bookstaver ML, Hess KL, Jewell CM. Self-Assembly of Immune Signals Improves Codelivery to Antigen Presenting Cells and Accelerates Signal Internalization, Processing Kinetics, and Immune Activation. *Small*. Sep 2018;14(38):e1802202. doi:10.1002/smll.201802202

113. Correa S, Boehnke N, Barberio AE, et al. Tuning Nanoparticle Interactions with Ovarian Cancer through Layer-by-Layer Modification of Surface Chemistry. *ACS Nano*. Feb 25 2020;14(2):2224-37. doi:10.1021/acsnano.9b09213

114. Zhang P, Andorko JI, Jewell CM. Impact of dose, route, and composition on the immunogenicity of immune polyelectrolyte multilayers delivered on gold templates. *Biotechnol Bioeng*. Feb 2017;114(2):423-431. doi:10.1002/bit.26083

115. DeMuth PC, Min Y, Huang B, et al. Polymer multilayer tattooing for enhanced DNA vaccination. *Nat Mater*. Apr 2013;12(4):367-76. doi:10.1038/nmat3550

116. He Y, Hong C, Li J, et al. Synthetic Charge-Invertible Polymer for Rapid and Complete Implantation of Layer-by-Layer Microneedle Drug Films for Enhanced Transdermal Vaccination. *ACS Nano*. Oct 23 2018;12(10):10272-80. doi:10.1021/acsnano.8b05373

117. Zeng Q, Gammon J, Tostanoski LH, Chiu YC, Jewell CM. In Vivo Expansion of Melanoma-Specific T Cells Using Microneedle Arrays Coated with Immune-Polyelectrolyte Multilayers. *ACS Biomater Sci Eng*. Feb 13 2017;3(2):195-205. doi:10.1021/acsbiomaterials.6b00414

118. Tostanoski LH, Eppler HB, Xia B, Zeng X, Jewell CM. Engineering release kinetics with polyelectrolyte multilayers to modulate TLR signaling and promote immune tolerance. *Biomater Sci*. Feb 26 2019;7(3):798-808. doi:10.1039/c8bm01572d

119. Wilson JT, Keller S, Manganiello MJ, et al. pH-Responsive nanoparticle vaccines for dual-delivery of antigens and immunostimulatory oligonucleotides. *ACS Nano*. May 28 2013;7(5):3912-25. doi:10.1021/nn305466z

120. Luo Z, Li P, Deng J, et al. Cationic polypeptide micelle-based antigen delivery system: a simple and robust adjuvant to improve vaccine efficacy. *J Controlled Release*. Sep 10 2013;170(2):259-67. doi:10.1016/j.jconrel.2013.05.027

121. Wilson JT, Postma A, Keller S, et al. Enhancement of MHC-I antigen presentation via architectural control of pH-responsive, endosomolytic polymer nanoparticles. *AAPS J*. Mar 2015;17(2):358-69. doi:10.1208/s12248-014-9697-1

122. Brubaker CE, Panagiotou V, Demurtas D, Bonner DK, Swartz MA, Hubbell JA. A Cationic Micelle Complex Improves CD8+ T Cell Responses in Vaccination Against Unmodified Protein Antigen. research-article. *ACS Biomater Sci Eng*. January 11, 2016 2016;2(2):231-40. doi:10.1021/acsbiomaterials.5b00456

123. Xu Y, Wang Y, Yang Q, et al. A versatile supramolecular nanoadjuvant that activates NF-κB for cancer immunotherapy. *Theranostics*. 2019;9(11):3388-97.

124. Tsai SJ, Amerman A, Jewell CM. Altering Antigen Charge to Control Self-Assembly and Processing of Immune Signals During Cancer Vaccination. *Frontiers in Immunology*. 01/06/2021 2021;11doi:10.3389/fimmu.2020.613830

125. Tsai SJ, Andorko JI, Zeng X, Gammon JM, Jewell CM. Polyplex interaction strength as a driver of potency during cancer immunotherapy. OriginalPaper. *Nano Res*. 2018-09-13 2018;11(10):5642-56. doi:doi:10.1007/s12274-018-2181-y

126. Froimchuk E, Oakes RS, Kapnick SM, Yanes AA, Jewell CM. Biophysical Properties of Self-Assembled Immune Signals Impact Signal Processing and the Nature of Regulatory Immune Function. *Nano Letters*. 05/12/2021 2021;21(9):3762-71. doi:10.1021/acs.nanolett.0c05118

127. Tsai SJ, Amerman A, Jewell CM. Altering Antigen Charge to Control Self-Assembly and Processing of Immune Signals During Cancer Vaccination. *Front Immunol*. 01/06/2021 2021;11doi:10.3389/fimmu.2020.613830

128. Sloane JA, Batt C, Ma Y, Harris ZM, Trapp B, Vartanian T. Hyaluronan blocks oligodendrocyte progenitor maturation and remyelination through TLR2. *Proc Natl Acad Sci U S A*. 06/22/2010 2010;107(25):11555-60. doi:10.1073/pnas.1006496107

129. Reynolds JM, Martinez GJ, Chung Y, Dong C. Toll-like receptor 4 signaling in T cells promotes autoimmune inflammation. *Proc Natl Acad Sci U S A*. 08/07/2012 2012;109(32):13064-9. doi:10.1073/pnas.1120585109

130. Celhar T, Magalhães R, Fairhurst AM. TLR7 and TLR9 in SLE: when sensing self goes wrong. *Immunol Res*. 2012 Sep 2012;53(1-3):58-77. doi:10.1007/s12026-012-8270-1

131. Prinz M, Garbe F, Schmidt H, et al. Innate immunity mediated by TLR9 modulates pathogenicity in an animal model of multiple sclerosis. *The Journal of clinical investigation*. 2006 Feb 2006;116(2):456-64. doi:10.1172/JCI26078

132. Gambuzza M, Licata N, Palella E, et al. Targeting Toll-like receptors: emerging therapeutics for multiple sclerosis management. *J Neuroimmunol*. 10/28/2011 2011;239(1-2):1-12. doi:10.1016/j.jneuroim.2011.08.010

133. Gao W, Xiong Y, Li Q, Yang H. Inhibition of Toll-Like Receptor Signaling as a Promising Therapy for Inflammatory Diseases: A Journey from Molecular to Nano Therapeutics. *Front Physiol*. 07/19/2017 2017;8:508. doi:10.3389/fphys.2017.00508

134. Hennessy EJ, Parker AE, O'Neill LA. Targeting Toll-like receptors: emerging therapeutics? *Nat Rev Drug Discov*. 2010 Apr 2010;9(4):293-307. doi:10.1038/nrd3203

135. Prinz M, Garbe F, Schmidt H, et al. Innate immunity mediated by TLR9 modulates pathogenicity in an animal model of multiple sclerosis. *J Clin Invest*. 2006 Feb 2006;116(2):456-64. doi:10.1172/JCI26078

136. Ho PP, Fontoura P, Ruiz PJ, Steinman L, Garren H. An Immunomodulatory GpG Oligonucleotide for the Treatment of Autoimmunity via the Innate and Adaptive Immune Systems. *J Immunol*. 2003-11-01 2003;171(9):4920-4926. doi:10.4049/jimmunol.171.9.4920

137. Ho PP, Fontoura P, Platten M, et al. A suppressive oligodeoxynucleotide enhances the efficacy of myelin cocktail/IL-4-tolerizing DNA vaccination and treats autoimmune disease. *J Immunol*. Nov 1 2005;175(9):6226-34. doi:10.4049/jimmunol.175.9.6226

138. Ho PP, Fontoura P, Ruiz PJ, Steinman L, Garren H. An Immunomodulatory GpG Oligonucleotide for the Treatment of Autoimmunity via the Innate and Adaptive Immune Systems. *J Immunol*. 2003-11-01 2003;171(9):4920-4926. doi:10.4049/jimmunol.171.9.4920

139. Ho PP, Fontoura P, Platten M, et al. A suppressive oligodeoxynucleotide enhances the efficacy of myelin cocktail/IL-4-tolerizing DNA vaccination and treats autoimmune disease. *J Immunol*. Nov 1 2005;175(9):6226-34. doi:10.4049/jimmunol.175.9.6226

140. Li L, Vorobyov I, Allen TW. The different interactions of lysine and arginine side chains with lipid membranes. *J Phys Chem B*. Oct 10 2013;117(40):11906-20. doi:10.1021/jp405418y

141. Delaney KT, Fredrickson GH. Theory of polyelectrolyte complexation—Complex coacervates are self-coacervates. *J Chem Phys*. 2017/06/14 2017;146(22):224902. doi:10.1063/1.4985568

142. Sing CE, Perry SL. Recent progress in the science of complex coacervation. 10.1039/D0SM00001A. *Soft Matter*. 2020;16(12):2885-2914. doi:10.1039/D0SM00001A

143. Robinson AP, Harp CT, Noronha A, Miller SD. The experimental autoimmune encephalomyelitis (EAE) model of MS: utility for understanding disease pathophysiology and treatment. *Handb Clin Neurol*. 2014 2014;122:173-89. doi:10.1016/B978-0-444-52001-2.00008-X

144. Ferreiro DU, de Prat-Gay G. A protein-DNA binding mechanism proceeds through multi-state or two-state parallel pathways. *J Mol Biol*. 08/01/2003 2003;331(1):89-99. doi:10.1016/s0022-2836(03)00720-4

145. Sokalingam S, Raghunathan G, Soundrarajan N, Lee SG. A study on the effect of surface lysine to arginine mutagenesis on protein stability and structure using green fluorescent protein. *PLoS One*. 2012 2012;7(7):e40410. doi:10.1371/journal.pone.0040410

146. Kelly SH, Wu Y, Varadhan AK, Curvino EJ, Chong AS, Collier JH. Enabling sublingual peptide immunization with molecular self-assemblies. *Biomaterials*. 2020 May 2020;241:119903. doi:10.1016/j.biomaterials.2020.119903

147. Xiang SD, Scholzen A, Minigo G, et al. Pathogen recognition and development of particulate vaccines: does size matter? *Methods*. 2006 Sep 2006;40(1):1-9. doi:10.1016/j.ymeth.2006.05.016

148. Lee K, Huang ZN, Mirkin CA, Odom TW. Endosomal Organization of CpG Constructs Correlates with Enhanced Immune Activation. *Nano Lett*. Aug 12 2020;20(8):6170-6175. doi:10.1021/acs.nanolett.0c02536

149. D'Andrea C, Pezzoli D, Malloggi C, et al. The study of polyplex formation and stability by time-resolved fluorescence spectroscopy of SYBR Green I-stained DNA. *Photochem Photobiol Sci*. 2014 Dec 2014;13(12):1680-89. doi:10.1039/c4pp00242c

150. Haladjova E, Rangelov S, Tsvetanov C. Thermoresponsive Polyoxazolines as Vectors for Transfection of Nucleic Acids. *Polymers*. 11/06/2020 2020;12(11):2609. doi:10.3390/polym12112609

151. Corse E, Gottschalk RA, Allison JP. Strength of TCR–Peptide/MHC Interactions and In Vivo T Cell Responses. *J Immunol*. 2011;186(9):5039-5045. doi:10.4049/jimmunol.1003650

152. Stadinski BD, Zhang L, Crawford F, Marrack P, Eisenbarth GS, Kappler JW. Diabetogenic T cells recognize insulin bound to IA^{g7} in an unexpected, weakly binding register. *Proc Natl Acad Sci U S A*. 2010;107(24):10978-10983. doi:10.1073/pnas.1006545107

153. Mohan JF, Petzold SJ, Unanue ER. Register shifting of an insulin peptide–MHC complex allows diabetogenic T cells to escape thymic deletion. *J Exp Med*. 2011;208(12):2375-2383. doi:10.1084/jem.20111502

154. Qi R, Wei G, Ma B, Nussinov R. Replica Exchange Molecular Dynamics: A Practical Application Protocol with Solutions to Common Problems and a Peptide Aggregation and Self-Assembly Example. *Methods Mol Biol*. 2018 2018;1777:101-119. doi:10.1007/978-1-4939-7811-3_5

155. R Z. Replica exchange molecular dynamics method for protein folding simulation. *Methods Mol Biol*. 2007 2007;350:205-23. doi:10.1385/1-59745-189-4:205

156. BR B, CL B, AD M, et al. CHARMM: the biomolecular simulation program. *J Comput Chem*. 07/30/2009 2009;30(10):1545-614. doi:10.1002/jcc.21287

157. S P, S P, R S, et al. GROMACS 4.5: a high-throughput and highly parallel open source molecular simulation toolkit. *Bioinformatics*. 04/01/2013 2013;29(7):845-54. doi:10.1093/bioinformatics/btt055

158. N M-A, EJ D, TB W, O B. MDAnalysis: a toolkit for the analysis of molecular dynamics simulations. *J Comput Chem*. 07/30/2011 2011;32(10):2319-27. doi:10.1002/jcc.21787

159. Kumar S, Nussinov R. Close-range electrostatic interactions in proteins. *Chembiochem*. 07/02/2002 2002;3(7):604-17. doi:10.1002/1439-7633(20020703)3:7<604::AID-CBIC604>3.0.CO;2-X

160. Donald JE, Kulp DW, DeGrado WF. Salt bridges: geometrically specific, designable interactions. *Proteins*. 2011 Mar 2011;79(3):898-915. doi:10.1002/prot.22927

161. Shirts MR, Chodera JD. Statistically optimal analysis of samples from multiple equilibrium states. *J Chem Phys*. 09/28/2008 2008;129(12):124105. doi:10.1063/1.2978177

162. Estimate 2D potential of mean force for alanine dipeptide parallel tempering data using MBAR.

163. Noid WG. Perspective: Coarse-grained models for biomolecular systems. *J Chem Phys*. Sep 7 2013;139(9):090901. doi:10.1063/1.4818908

164. Ingólfsson HI, Lopez CA, Uusitalo JJ, et al. The power of coarse graining in biomolecular simulations. *Wiley Interdiscip Rev: Comput Mol Sci*. 2014;4(3):225-248. doi:10.1002/wcms.1169

165. Sahoo A, Xu H, Matysiak S. Pathways of amyloid-beta absorption and aggregation in a membranous environment. 10.1039/C9CP00040B. *Phys Chem Chem Phys*. 2019;21(16):8559-8568. doi:10.1039/C9CP00040B

166. Ganesan SJ, Matysiak S. Role of Backbone Dipole Interactions in the Formation of Secondary and Supersecondary Structures of Proteins. *J Chem Theory Comput*. Jun 10 2014;10(6):2569-2576. doi:10.1021/ct401087a

167. Ganesan SJ, Xu H, Matysiak S. Effect of lipid head group interactions on membrane properties and membrane-induced cationic β-hairpin folding. 10.1039/C5CP07669B. *Phys Chem ChemPhys*. 2016;18(27):17836-17850. doi:10.1039/C5CP07669B

168. Uusitalo JJ, Ingólfsson HI, Akhshi P, Tieleman DP, Marrink SJ. Martini Coarse-Grained Force Field: Extension to DNA. *J Chem Theory Comput*. 2015/08/11 2015;11(8):3932-3945. doi:10.1021/acs.jctc.5b00286

169. Marrink SJ, de Vries AH, Mark AE. Coarse Grained Model for Semiquantitative Lipid Simulations. *J Phys Chem B*. 2004/01/01 2004;108(2):750-760. doi:10.1021/jp036508g